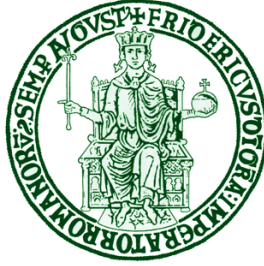


# UNIVERSITY OF NAPLES “FEDERICO II”



## PHD SCHOOL IN INDUSTRIAL ENGINEERING

DEPARTMENT OF ELECTRICAL ENGINEERING AND INFORMATION TECHNOLOGIES

### PHD COURSE IN ELECTRICAL ENGINEERING

XXVI course

**PhD Thesis of Cosimo Pisani**

## ***Real Time tracking of electromechanical oscillations in ENTSO-e Continental European Synchronous Area***

Academic supervisors

Davide Lauria

Domenico Villacci

PhD Coordinator:

Claudio Serpico

Company supervisor:

Giorgio Maria Giannuzzi, Eng. (Terna Rete Italia)

March 2014

March 2014

Department of  
Electrical Engineering and Information Technology  
University of Naples "Federico II"  
P.O. Box 80125  
Napoli  
ITALY

<http://www.dieti.unina.it/>

©Cosimo Pisani

Printed in Benevento, ITALY

## Contents

<b>Abstract</b> .....	<b>5</b>
<b>Acknowledgements</b> .....	<b>8</b>
<b>List of Abbreviations</b> .....	<b>9</b>
<b>List of Figures</b> .....	<b>12</b>
<b>List of Tables</b> .....	<b>15</b>
<b>Chapter 1</b> .....	<b>17</b>
<b>Introduction</b> .....	<b>17</b>
1.1 ELECTROMECHANICAL OSCILLATIONS IN POWER SYSTEMS .....	20
1.1 MOTIVATIONS .....	21
1.2 OBJECTIVES .....	23
1.3 CONTRIBUTIONS .....	24
1.4 THESIS OUTLINE .....	25
<b>Chapter 2</b> .....	<b>26</b>
<b>Wide Area Monitoring Systems</b> .....	<b>26</b>
2.1 WAMS: DEFINITION AND CONSTITUTIVE SUB-PROCESSES .....	27
2.1.1 DATA RESOURCES .....	28
2.2 WAMS APPLICATIONS/FUNCTIONALITIES .....	33
2.3 WAMS COMMUNICATION INFRASTRUCTURES .....	34
2.4 ITALIAN WAMS ARCHITECTURE AND FUNCTIONALITIES .....	38
2.5 WAMS MEASUREMENT DATA CLASSIFICATION .....	41
2.6 PREPROCESSING SYNCHRONIZED PHASOR MEASUREMENT DATA FOR CAPTURING POWER SYSTEMS DYNAMIC ...	42
<b>Chapter 3</b> .....	<b>44</b>
<b>Power Systems Dynamic</b> .....	<b>44</b>
<b>Estimation Techniques</b> .....	<b>44</b>
3.1 MODAL ANALYSIS.....	45
3.1.1 FUNDAMENTALS .....	45
3.1.2 POWER SYSTEM MODEL LINEARIZATION .....	48
3.1.3 STABILITY ANALYSIS AND RELATED CONCEPTS .....	51
3.2 FOURIER TRANSFORM BASED METHODS.....	55
3.3 PRONY ANALYSIS .....	58
3.4 TUFTS-KUMARESAN METHOD.....	59
3.5 NON LINEAR LEAST SQUARES METHODS .....	62
3.6 EXTENDED COMPLEX KALMAN FILTER .....	65
3.7 HILBERT TRANSFORM BASED METHODS.....	68
3.7.1 EMPIRICAL MODE DECOMPOSITION.....	69
3.7.2 HILBERT TRANSFORM .....	71
3.7.3 HILBERT HUANG TRANSFORM LIMITATIONS .....	76
3.7.4 HHT REFINEMENTS.....	77
3.7.4.1 HHT WITH STANDARD MASKING TECHNIQUE.....	78
3.7.4.2 FREQUENCY HETERODYNE TECHNIQUE .....	80
3.7.4.3 HHT WITH IMPROVED MASKING TECHNIQUE .....	82
3.7.4.4 TARGETED APPROACH TO APPLY MASKING SIGNAL-BASED EMPIRICAL MODE DECOMPOSITION .....	87
<b>Chapter 4</b> .....	<b>89</b>
<b>Advances in the use of</b> .....	<b>89</b>

<b><i>Hilbert Transform</i></b> .....	<b>89</b>
4.1 AN ADVANCED METHODOLOGY HILBERT TRANSFORM BASED FOR ESTIMATING THE POWER SYSTEMS MODAL CONTENT .....	90
4.1.1 A SIGNAL DECOMPOSITION THEOREM HILBERT TRANSFORM BASED .....	90
4.1.2 DECOMPOSITION THEOREM PROOF .....	91
4.1.3 A ROBUST NON LINEAR SPECTRAL ANALYZER.....	95
4.2 NUMERICAL IMPLEMENTATION OF THE HILBERT TRANSFORM.....	97
4.2.1 HILBERT BOCHE APPROACH.....	97
4.3 AN IMPROVED NON LINEAR LEAST SQUARES METHOD FOR ESTIMATING THE DAMPING LEVELS OF ELECTROMECHANICAL OSCILLATIONS.....	100
<b>Chapter 5</b> .....	<b>108</b>
<b><i>Experimental Findings</i></b> .....	<b>108</b>
5.1 A SYNTHETIC SIGNAL .....	108
5.1.1 INCIDENCE OF WAMS COMMUNICATION NETWORK EFFECTS.....	114
5.1.1.1 NOISE INCIDENCE.....	115
5.1.1.2 DATA PACKET DROPOUTS INCIDENCE.....	118
5.2 KUNDUR’S TWO AREA TEST SYSTEM.....	122
5.3 IEEE 9 BUS TEST SYSTEM .....	131
5.4 IEEE 68 BUS TEST SYSTEM .....	138
5.5 REAL ELECTROMECHANICAL OSCILLATIONS IN ENTSO-E INTERCONNECTED NETWORK SYSTEM GRID.....	143
5.5.1 A SUDDEN INTER-AREA OSCILLATION RECORDED IN THE CONTINENTAL EUROPE ON 19 <sup>TH</sup> FEBRUARY 2011.....	144
5.5.2 NORTH-SOUTH INTER-AREA MODE EXCITED BY A FAULT OCCURRENCE IN ITALY.....	148
5.5.3 SARDINIA LOCAL OSCILLATIONS.....	150
<b>Chapter 6</b> .....	<b>158</b>
<b>APPENDIX A – BEDROSIAN THEOREM PROOF</b> .....	<b>160</b>
<b>APPENDIX B – THEOREM PROOF ON CAUCHY PRINCIPAL VALUE INTEGRAL OF OSCILLATORY FUNCTIONS</b> .....	<b>162</b>

## Abstract

Small signal stability is a crucial aspect to accurately keep under control in modern interconnected power systems in order to ensure their security and reliability. Such an aspect could represent a serious limiting factor in the search for ever higher power systems exploitation levels. Power oscillations not well-damped may jeopardize the system integrity on large scale: several incidents caused by the establishment of large oscillations have been recorded in the past around the world. Therefore, a basic assessment that must be done before setting a certain optimal operational framework is the determination of the actual dynamic stability margins.

The fast deployment of measurement and instrumentation facilities provided by the Wide Area Measurement Systems (WAMS) technology offers a valid support in this sense. Large amount of data coming from Phasor Measurement Units (PMU) installed in the key points of power systems (e.g. primary substations) increases the Transmission System Operators (TSO) *situational awareness*. Thanks to accurate and timely information the stability margins can be precisely determined and optimized so that power systems can be operated at their actual full capacity while staying within the stability boundaries.

A deep investigation about the WAMS currently in operation or under testing around the world confirms how power oscillations tracking is one of the main functionality/application envisaged in these architectures. Real time detection of dangerous power oscillations and hence their related continuous parameters estimation, in wide area sense, is vital in the framework pointed out above. The output of this task is therefore represented by estimates of the oscillations fundamental parameters (e.g. frequency, damping factor/ratio, amplitude and phase). If potential unstable phenomena are detected (e.g. estimating a damping ratio lower than a certain threshold value) all the necessary countermeasures have to be implemented for restoring secure and stable operating conditions (e.g. generators' re-dispatch, tie line flows adjustment, load reduction, network topology change etc.).

It was moreover found that the major problems which characterize these infrastructures rely on their own technological complexity, on the data management but especially on the research of robust identification techniques for implementing all the Dynamic Security Assessment (DSA) tasks that must be run in parallel in the central control centres. In this regard, two fundamental approaches could be applied for tracking the electromechanical modes in an electrical power system. *Model-based methods* (a.k.a. *Component-based method*), which use an electric power system model linearized around a certain

March 2014

equilibrium point to identify the electromechanical modes characteristics through eigenvalue analysis (whose chief rudiments are reported in the Chapter 3). Eigenvalue analysis is not suitable for on-line tracking, especially for large scale power systems due to both high computational time and uncertainties in power system modeling. *Measurement-based methods* (a.k.a. *Mode Meters*), estimate an updated model of the electric power system from direct system measurements which come from measurement devices installed on power systems. These techniques, freeing themselves from the system modeling, they consider the power system as a black box and by making use of the signal processing expertise, estimate the modal content of the acquired signals. Being moreover less expensive than the first class of methods in large scale power systems model set up, it appears clear that they are suitable for an on-line DSA task.

However, the set of available measurement-based estimation techniques is fairly wide. Besides I note that relevant journal databases are regularly filled by novel more and more advanced algorithms. My personal feeling in this regard is that the basic methodologies are really few, while several refinements of the same algorithms, aimed at overcoming specific weaknesses, are regularly proposed. From the experience gained working hardly on the topic I can state that no best estimator exists due to the lack of an accepted definition of optimality. Furthermore, it is a difficult task to assess the performance of different estimation methods because each of them was initially designed for a specific field, has its own features and sometimes presents parameters chosen according to experience or through heuristic considerations. This means that for instance a method could show good performance in damping and frequency estimation if the modes number is known while may fail if it is not known in advance. In addition, a method could work better than another for noiseless sampled signals while could deteriorate its efficiency when the signal-to-noise ratio (SNR) decreases.

Nonetheless, there exist estimation techniques which are “generally” characterized by good performance with respect to the others. The meaning of the term “generally” should be intended as “with respect to the main situations that may occur”(different data typologies, various SNR levels, a priori knowledge of the intrinsic power system modes etc.). A wide set of estimation techniques will be analyzed in the present thesis. Afterwards, a performance comparison among the techniques will be accomplished with the objective of pointing out strengths and drawbacks of each of them. Once ascertained the points to improve, three novel estimation algorithms will be introduced. They represent a good complementary tool to the ordinary model-based methods implemented in the central control centres for real time monitoring power system oscillations. Almost all the estimation algorithms considered in the thesis were tested in real time on the Italian WAMS thanks to the support of the

March 2014

TSO, Terna. The complex infrastructure owned by Terna, thanks also to the real time information exchange with some European partners, represents a vigilant eye on the entire European Network of Transmission System Operators for electricity-Continental European Synchronous Area (ENTSO-e CESA) for the purposes of analysis. The emphasis of this research was hence to tailor high accurate and resilient estimation algorithms for real time monitoring of electromechanical oscillations, in particular of inter-area type, in such a large interconnected system. Although the doctorate course ends achieving the predetermined objectives the research on the topic will continue.

March 2014

## Acknowledgements

This thesis, although wholly written by me, would not have been possible without the cooperation and aid of some persons. First of all Veronica who accepted a not conventional lifestyle made of much sacrifice and less free time to spend, especially for tolerating my perpetual mood swings. I increasingly believe that the study has sometimes negative influence on the physical and psychological human health. I thought that Professor Antonio Feoli was joking in saying this during the Physic III exam, contrariwise he was not joking at all. I would like to thank my family for supporting me under all the viewpoints and especially for not having interfered with my plans. I sincerely thank, in equal manner, my academic supervisors Professor Davide Lauria and Professor Domenico Villacci, for their willingness and patience as well as for the constant encouragement to do my best. Of the former, I will never forget the extraordinary ability in the codes programming as well as his granitic mathematical background. Of the latter, I will never forget without any doubt his deep knowledge of all engineering aspects in power systems studies as well as the extraordinary personal and human qualities. A special thank is due to Terna and in particular to the Engineer Giorgio Maria Giannuzzi for his valuable suggestions resulting from many years of experience in field on the topic.

March 2014

## List of Abbreviations

WAMS	WIDE AREA MONITORING SYSTEM
PMU	PHASOR MEASUREMENT UNIT
DSA	DYNAMIC SECURITY ASSESSMENT
SNR	SIGNAL-TO-NOISE RATIO
ENTSO-e	EUROPEAN NETWORK OF TRANSMISSION SYSTEM OPERATORS FOR ELECTRICITY
CESA	CONTINENTAL EUROPEAN SYNCHRONOUS AREA
EPS	ELECTRIC POWER SYSTEMS
HVSD	HANKEL SINGULAR VALUE DECOMPOSITION
VARPRO	VARIABLE PROJECTION ALGORITHM
HHT	HILBERT-HUANG TRANSFORM
HT	HILBERT TRANSFORM
SCADA	SUPERVISORY CONTROL AND DATA ACQUISITION
WACS	WIDE AREA CONTROL SYSTEM
WAPS	WIDE AREA PROTECTION SYSTEM
WAMPACS	WIDE AREA MONITORING PROTECTION CONTROL SYSTEM
EMS	ENERGY MANAGEMENT SYSTEM
COMTRADE	COMMON FORMAT FOR TRANSIENT DATA EXCHANGE
MTU	MASTER TERMINAL UNIT
RTU	REMOTE TERMINAL UNIT
PLC	PROGRAMMABLE LOGIC CONTROLLERS
IED	INTELLIGENT ELECTRONIC DEVICES
GPS	GLOBAL POSITIONING SYSTEM
NCS	NETWORK CONTROL SYSTEM
CCC	CENTRAL CONTROL CENTRE
SPMS	SYNCHRONIZED PHASOR MEASUREMENT SYSTEM

March 2014

PDC	PHASOR DATA CONCENTRATOR
DFR	DIGITAL FAULT RECORDER
DPR	DIGITAL PROTECTIVE RELAY
CBM	CIRCUIT BREAKER MONITOR
SE	STATE ESTIMATION
LF	LOAD FLOW
OPF	OPTIMAL POWER FLOW
LF	LOAD FORECAST
ED	ECONOMICAL DISPATCH
OSI	OPEN SYSTEM INTERCONNECTION
CR	CONTROL ROOM
TSO	TRANSMISSION SYSTEM OPERATOR
DNC	DIRECT NUMERICAL CIRCUIT
NCC	NATIONAL CONTROL CENTER
EMS	ENERGY MANAGER SYSTEM
FIR	FINITE IMPULSE RESPONSE
IIR	INFINITE IMPULSE RESPONSE
DFT	DISCRETE FOURIER TRANSFORM
FFT	FAST FOURIER TRANSFORM
STFT	SHORT TIME FOURIER TRANSFORM
TKM	TUFTS KUMARESAN METHOD
SVD	SINGULAR VALUE DECOMPOSITION
NLS	NON LINEAR LEAST SQUARES
VARPRO	VARIABLE PROJECTION METHOD
HSVD	HANKEL SINGULAR VALUE DECOMPOSITION
EMD	EMPIRICAL MODE DECOMPOSITION
IMF	INTRINSIC MODE FUNCTION
M-EMD	HHT WITH STANDARD MASKING TECHNIQUE
R-EMD	FOURIER-BASED MASKING TECHNIQUE
A-EMD	EMD WITH ENERGY-BASED MASKING TECHNIQUE

March 2014

T-EMD	TARGETED APPROACH TO APPLY MASKING SIGNAL-BASED EMPIRICAL MODE DECOMPOSITION
FHT	FREQUENCY HETERODYNE TECHNIQUE
DHT	DISCRETE HILBERT TRANSFORM
HB	HILBERT BOCHE
CPV	CAUCHY PRINCIPAL VALUE
LPM	LAURIA PISANI METHOD
HB	HILBERT BOCHE
CPV	CAUCHY PRINCIPAL VALUE
PSS	POWER SYSTEM STABILISER
WSCC	WESTERN SYSTEM COORDINATING COUNCIL
DG	DISPERSED GENERATION
UTC	COORDINATED UNIVERSAL TIME
DG	DISPERSED GENERATION
UTC	COORDINATED UNIVERSAL TIME

## List of Figures

- Fig. 2.1 WAMS process in power systems
- Fig. 2.2 Supervisory and Control Data Acquisition architecture
- Fig. 2.3 Synchronized Phasor Measurement System structure
- Fig. 2.4 Layering in WAMS based on OSI reference model
- Fig. 2.5 Italian WAMS graphical user interface
- Fig. 2.6 Italian WAMS architecture
- Fig. 2.7 WAMS measurement data types
- Fig. 2.8 – Preprocessing unit
- Fig. 3.1 Zeros displacement of the  $B(z)$  polynomial in Tufts-Kumaresan method
- Fig. 3.2 Fourier spectra of the signals in (3.94) and (3.95)
- Fig. 3.3 Masking signal
- Fig. 3.4 Fourier spectrum of the first IMF from the M-EMD of the signal in (3.95)
- Fig. 3.5 Lower sideband signal related to the one in (3.95)
- Fig. 3.6 Fourier spectrum of the lower sideband signal related to the one in (3.95)
- Fig. 4.1 Hilbert transform of the synthetic signal in (4.36): comparison between the standard routine of Matlab® and the Boche approximation
- Fig. 4.2 Path of integration for  $I_{\omega}(f;t)$
- Fig. 4.3 Time domain decomposition of the signal in (4.48) according to the proposed decomposition theorem: standard HT routine of Matlab® vs adopted one based on Boche method
- Fig. 4.4 Data packet dropouts: a) Rate 1, b) Rate 2, c) Rate 3.
- Fig. 4.5 HT regularization action with respect to the data packet dropouts
- Fig. 5.1 Synthetic signal
- Fig. 5.2 IMF from M-EMD: Synthetic signal.

March 2014

- Fig. 5.3 First IMF Fourier spectrum in the case of M-EMD application and R-EMD application
- Fig. 5.4 FFT and  $L_p$  periodogram : synthetic signal.
- Fig. 5.5 Time domain decomposition of the un-damped synthetic signal: comparison between standard Hilbert Transform and Hilbert Boche approximation.
- Fig. 5.6 Estimation accuracy bar graph : synthetic signal.
- Fig. 5.7 Damping computation via LPM : noiseless signal.
- Fig. 5.8 Damping computation via LPM : Synthetic signal, SNR = 10 dB.
- Fig. 5.9 Change of the  $p$ -value in the Bernoulli process : effect on the synthetic signal.
- Fig. 5.10 Kundur's two area test system
- Fig. 5.11 Eigenvalues disposal: two area test system.
- Fig. 5.12 Active power between the areas: two area test system.
- Fig. 5.13 Estimation accuracy bar graph: two area test system.
- Fig. 5.14 Estimated damping coefficient vs Hankel matrix size L: Tufts Kumaresan algorithm.
- Fig. 5.15 Signal reconstruction: Hankel Singular Value Decomposition - VARIABLE PROjection.
- Fig. 5.17 Empirical Mode Decomposition output : two area test system.
- Fig. 5.18  $L_p$  Periodogram vs FFT: two area test system.
- Fig. 5.19 Damping coefficient estimation through linear regression procedure : two area test system.
- Fig. 5.20 IEEE 9 bus test system
- Fig. 5.21 Compass plot of the eigenvectors associated to the rotor angle terms: a) Mode #1 - b) Mode #2.
- Fig. 5.22 Relative angular speed between the generators 1 and 3 : IEEE 9 bus test system.
- Fig. 5.23 Estimation accuracy bar graph : IEEE 9 bus test system.
- Fig. 5.24 Fourier spectrum of the relative angular speed between the generators 1 and 3 : IEEE 9 bus test system.
- Fig. 5.25 Change of the  $p$ -value in the Bernoulli process : effect on the synthetic signal.

March 2014

- Fig. 5.26  $L_p$  periodogram of the relative angular speed between the generators 3 and 1: IEEE 9 bus test system.
- Fig. 5.27 Damping coefficient estimation through linear regression procedure : IEEE 9 bus test system.
- Fig. 5.28 IEEE 68 bus test system
- Fig. 5.29 Relative angular speed between the generators 7 and 13 : IEEE 68 bus test system.
- Fig. 5.30 Estimation accuracy bar graph : IEEE 68 bus test system.
- Fig. 5.31 FFT of the relative angular speed between the generators 7 and 13 : IEEE 68 bus test system.
- Fig. 5.32  $L_p$  periodogram of the relative angular speed between the generators 7 and 13 : IEEE 68 bus test system.
- Fig. 5.33 ENTSO-E CESA inter-area modes
- Fig. 5.34 Frequency recorded at Brindisi (Italy) on February 19<sup>th</sup> 2011
- Fig. 5.35 Voltage magnitude recorded at Palermo (Italy) on January 18<sup>th</sup> 2008
- Fig. 5.36 Waveforms recorded at Cagliari and Fiumesanto (Italy) on August 13<sup>th</sup> 2007
- Fig. 5.37 FFT vs  $L_p$  Periodogram on a 20 s time-window : voltage magnitude at Cagliari

## List of Tables

Tab. 2.1 a)	WIDE AREA MONITORING SYSTEMS GUIDED MEDIA
Tab. 2.1 b)	WIDE AREA MONITORING SYSTEMS UNGUIDED MEDIA
Tab. 3.1	HILBERT TRANSFORM PAIRS
Tab. 4.1	NODES AND WEIGHTS IN GAUSS-LAGUERRE 5 POINTS QUADRATURE RULE
Tab. 4.2	DAMPING ESTIMATION OUTCOMES: VARPRO vs IMPROVED NLS
Tab. 5.1	ESTIMATION ALGORITHMS OUTCOMES - SYNTHETIC SIGNAL
Tab. 5.2	ESTIMATION ALGORITHMS OUTCOMES WITH RESPECT TO THE NOISE - SYNTHETIC SIGNAL
Tab. 5.3	ESTIMATION ALGORITHMS OUTCOMES WITH RESPECT TO THE DATA PACKET DROPOUTS - SYNTHETIC SIGNAL
Tab. 5.4	MODAL ANALYSIS MAIN OUTCOMES - TWO AREA TEST SYSTEM
Tab. 5.5	ESTIMATION ALGORITHMS OUTCOMES - TWO AREA TEST SYSTEM
Tab. 5.6	MODAL ANALYSIS MAIN OUTCOMES - IEEE 9 BUS TEST SYSTEM
Tab. 5.7	ESTIMATION ALGORITHMS OUTCOMES - IEEE 9 BUS TEST SYSTEM
Tab. 5.8	MODAL ANALYSIS MAIN OUTCOMES - IEEE 68 BUS TEST SYSTEM
Tab. 5.9	ESTIMATION ALGORITHMS OUTCOMES - IEEE 68 BUS TEST SYSTEM
Tab. 5.10	ESTIMATION ALGORITHMS OUTCOMES - ENTSO-e CESA NORTH SOUTH MODE a)
Tab. 5.11	ESTIMATION ALGORITHMS OUTCOMES - ENTSO-e CESA NORTH SOUTH MODE b)

March 2014

Tab. 5.12	ESTIMATION ALGORITHMS OUTCOMES - SARDINIA LOCAL OSCILLATIONS, MODE 1
Tab. 5.13	ESTIMATION ALGORITHMS OUTCOMES - SARDINIA LOCAL OSCILLATIONS, MODE 2
Tab. 5.14	ESTIMATION ALGORITHMS OUTCOMES - SARDINIA LOCAL OSCILLATIONS, MODE 3
Tab. 5.15	ESTIMATION ALGORITHMS OUTCOMES - SARDINIA LOCAL OSCILLATIONS, MODE 4

# Chapter 1

## *Introduction*

In the most common structures of interconnected electrical power systems generators produce alternating current and are synchronized to operate at the same frequency network. In this structure kind, although the load demand should be conceptually shared among the machines according to their nameplate rating, the need to maintain frequency within a narrow operating range, leads the network operators to continuously adjust the generators power. Alternating current generators can lose the synchronism due to the self-regulating properties of their interconnection: if the angular speed of one generator deviates from the synchronous one, the remaining generators are loaded in such a way to allow it the synchronous speed restoring. A fundamental role in re-establishing such as condition is played by generator moment inertia that can be understood as a measure of the generator overcorrecting expedition.

Power system oscillations represent a characteristic phenomenon of electrical power systems caused by the continuous exchange of momentum among rotating masses, chiefly those of the synchronous generators. Therefore there is nothing extra-ordinary in the power oscillations arising, it deals with an inherent phenomenon of power systems, hence we should be surprised if they were absent. For this reason, to prevent power oscillations occurrence is generally recognized a futile strategy. System operators live constantly with these oscillations keeping them under constant control and mitigating their effects on system operations. These effects are basically determined by the damping levels.

Different measures of damping for an electromechanical mode can be found in literature such as *damping coefficient*, *time-domain damping*, *logarithmic decrement* etc. The most adopted one is without any doubt the damping ratio  $\xi$  expressed in percentage. Such a definition underlies the assumption of a second order linearized model for describing the power system response to a certain perturbation able to excite a sole electromechanical mode. It appears clear that this manner of measuring the electromechanical mode damping level, although

March 2014

widely employed, is quite simplified. In my opinion, significant efforts must be done in order to propose a more comprehensive index of evaluation. This is in any case behind the scope of this thesis. High damping ratios means that the power oscillation quickly decays (being stable) and does not represent an actual concern. Low damping ratios, essentially due to the lack of damping torque at the generator rotors, means large-amplitude variations in power system variables such as voltage, frequency, active and reactive power flows on the transmission lines which may result in system breakup and large-scale blackouts.

Whilst establishing a closed-form analytical relationship between power oscillations and system operating parameters is not practical, it can be argued that the damping ratio depends non-linearly on several factors such as network topology, generators' production program, load levels, tie lines power flows etc. Furthermore it can be observed that damping ratio decreases significantly with the enhancement of the overall system exploitation levels. This highlights how in modern power systems situations of serious danger for the network stability and reliability might realistically occur, taking into account that the power systems are often asked to operate close to their nameplate capacity.

Therefore, to exploit as much as possible the existing networks, ensuring at the same time adequate security levels determining the dynamic stability margins, the system operators must continuously monitor the power oscillations estimating their the fundamental parameters (e.g. frequency, damping factor/ratio, amplitude and phase). If potential unstable phenomena are detected (e.g. estimating a damping ratio lower than a certain threshold value) all the necessary countermeasures have to be implemented for restoring secure and stable operating conditions for instance generators' re-dispatch, tie line flows adjustments, load reduction, network topology change etc.

Therefore, in order to prevent these catastrophic phenomena a continuous system tracking of power oscillations, in a wide-area sense, has to be performed. Power oscillations tracking can be currently performed in real time thanks to the quick development of the WAMS. WAMS use sophisticated digital recording devices, i.e. phasor measurement units (PMU), to record and export GPS-synchronized, high sampling rate (6-60 samples/second) dynamic power system data [1]. A deep investigation about the WAMS currently in operation or under testing around the world shows how power oscillations tracking is one of the main functionality envisaged in these architectures [2], [3], [4], [5], [6], [7]. It was moreover found that the major problems which characterize these infrastructures rely on their own technological complexity, on the data management but especially the research of robust identification techniques for all the analysis that must be run in parallel in the central control centres. In this regard, two fundamental approaches could be applied for tracking the electromechanical modes in an electrical power system [8]. *Model-*

March 2014

*based methods* (a.k.a. *Component-based methods*), which use an electric power system model linearized around a certain equilibrium point to identify the electromechanical modes characteristics through eigenvalue analysis. Eigenvalue analysis is not suitable for on-line tracking, especially for large scale power system due to both high computational time and uncertainties in power system modelling. *Measurement-based methods* (a.k.a. *Mode Meters*), estimate an updated model of the electric power system from direct system measurements which come from measurement devices installed on power system [9]. These techniques, freeing themselves from the system modeling, they consider the power system as a black box and by making use of the signal processing expertise, estimate the modal content of the acquired signals. Being moreover less expensive than the first class of methods in large scale power systems model setting up, it appears clear that they are suitable for an on-line DSA task. However, the set of available measurement-based estimation techniques is fairly wide. Among the other things, different versions (refinements) of the same method can be found in literature which have been developed with the aim of overcoming the specific weaknesses of the basic version. Driven by the same objective, also some integrated multi-steps methodologies which combine basic methods have also been proposed in literature. Essentially, the basic concept is that no best estimator exists due to the lack of an accepted definition of optimality [10]. Furthermore, it is a difficult task to assess the performance of different methods because each of them was initially designed for a specific field, has its own features and sometimes presents parameters chosen according to experience or through heuristic considerations. This means that for instance a method could show good performance in damping and frequency estimation if the modes number is known while may fail if it is not known in advance. In addition, a method could work better than another for noiseless sampled signals while could deteriorate its efficiency when the signal-to-noise ratio (SNR) decreases.

The framework above has outlined numerous aspects which make the considered research problem quite complex, for this reason, the methodologies selection to tackle the problem was the result of a thorough literature review. Obviously, such a set of estimation techniques can not be considered exhaustive but represents without any doubt the review of the most popular and actually employed in real systems. Once known the state of art, the research consisted in the implementation of the mentioned techniques in Matlab® environment on a leased computing unit of the Italian WAMS that receives real-time acquired data via proprietary protocol or standard Object Linking and Embedding for Process Control. The real-time behaviour of the investigated estimation algorithms, summarized in some test reports related to different test periods, allowed to recognize strengths and drawbacks of each of them. These results were really valuable for us to identify the weak points on which act. Hence the

March 2014

work consisted in the development of some estimation algorithms, accurate and robust enough, to be employed in real time for tracking electromechanical oscillations in power systems. Thanks to the willingness and the support of the Terna's experts we had the possibility to work on a privileged application domain, exactly the ENTSO-e CESA. The experimental findings obtained in field on the widely interconnected system and the scientific awards recently obtained in the international accredited literature confirm the merit of the work done.

## 1.1 Electromechanical oscillations in power systems

As stated already, electromechanical oscillations are inherent to power networks, and are observed as soon as synchronous generators are interconnected to provide more power capacity and greater reliability. These power oscillations can be readily classified according to two different criteria: the operational setting in which they occur and the system equipment involved in. According to the former, oscillations can be divided into *spontaneous*, *transient* and *forced* [11]. Spontaneous oscillations are typically amplitude-limited and characterized by reduced variations from the initial low values. They generally occur during ambient conditions; that is in steady-state conditions. Transient oscillations appear following a perturbation of a certain entity (generation/load disconnections, line trips, etc.), then assume large amplitudes already at their onset. They can become potentially unstable under certain circumstances. Forced oscillations arise between two asynchronous islands of an electrical system, just as the previous ones assume large amplitudes at the onset and persist until islanding has been completed. According to the second criterion, oscillations can be divided into *local*, *inter-area*, *intra-plant*, *control* and *torsional* [12]. Local oscillations arise among generators installed in a certain area, with respect to the rest of the power system. They are characterized by a typical frequency range between 0.8 and 2.0 Hz. Inter-area oscillations occur on power networks when two parts of an electrical system with a large number of generators are connected by a weak tie-line. In this case, coherent generator groups swing against each other, with a typical frequency range between 0.1 and 0.8 Hz. Intra-plant oscillations appear at the same power generation site as a result of the installed machines oscillatory behaviour against the rest of the system. They show a typical frequency range between 2.0 and 3.0 Hz, depending on the entity of the installed capacity, and on the reactance values connecting the units. Control oscillations can arise from the erroneous tuning of the generators' control

March 2014

systems, controllable loads, Flexible Alternating Current Transmission System (FACTS), High Voltage Direct Current (HVDC) systems etc., or from erroneous interaction among the aforementioned control systems. These modes are to be found in the frequency range from 3.0–10 Hz. Finally, torsional oscillations, associated to the turbine generator shaft systems, are particularly identifiable when a generator is connected to the grid through a series compensated line. They fall into a typical frequency range of 10–46 Hz. The present thesis will specifically evaluate the performance of several mode meters with respect to spontaneous and ambient/ringdown (transient) oscillations, as well as with respect to local and inter-area oscillations, although the employed methodologies are general enough to face with all the other oscillation classes described in this Section.

## 1.1 Motivations

The need for providing a reliable and safe service has historically induced asset owners to adopt conservative strategies in planning and management of electric power systems (EPS) [13]. In a deregulated electricity market this worst case approach appears inadequate considering that the maximization of the profits and social welfare involve performance push for each system component [14]. Furthermore, whereas the construction of new electric lines (and in general of EPS) is often prevented by several issues (economics, environmental, social etc.) it appears evident how is crucial to determine the real exploitation margins of the existing networks in order to safely accommodate growing power flows [15]. The stress exercised on the EPS lead themselves to operate close to the stability limits, hence a proper stability evaluation must be made in order to investigate the real loadability of the system. The traditional manner to face with power systems stability issue is to identify an updatable set of critical contingencies in a certain operating condition and to perform extensive simulation studies aiming at evaluating if the operation would be secure or insecure. Indeed the simulation models employed could not exactly describe the power system behaviour due to the several factors.

A model will always be an approximated representation of a real-life system. Such an approximation is better the higher the level of detail. In order to realize more simple dynamic models to implement and simulate, in the electrical engineering practice, a certain mismatch between the dynamic behaviour of the simulated power system and the real power system is accepted. More specifically, for instance, information of the load dynamics is often unknown to the TSO or generally the grid model is not updated afterwards network assets

March 2014

reinforcement or replacement. A further source of discrepancy between the simulated and the real dynamic behaviour of the power systems is represented by missing or incorrect data. Due to these differences, adequate operational margins have to be maintained between the actual implemented power systems loadability margins and the theoretical maximum power systems loadability margins, to maintain sufficient system security.

Therefore one challenging task for TSO in grid operation and planning is to maximize system exploitation keeping the network security high. In this framework, to acquire advanced techniques for estimating power systems dynamic from real measurements is essential. This is perfectly in line with the major recommendations provided by the ENTSO-E downstream the most recent blackout on September 28<sup>th</sup> 2003 in Italy [16] and the system disturbance recorded in UCTE (Union for the Coordination of the Transmission of Electricity) power system on November 4<sup>th</sup> 2006 [17]:

Recommendation #1

Extend the real time data exchange among neighbouring TSO. Data should be consistent to run the state estimators in a reliable way on a wider topology basis.

Recommendation #2

As a support tool for dynamic analysis and monitoring of the UCTE system, accelerate the ongoing WAMS installation programs.

As can be noted, the recommendations above point out the strategic role of the wide area measurements, TSO coordination and state estimators (in wide sense) algorithms. They are the enabling technologies and practices to necessarily adopt for minimizing the disruption risk. Thanks to these tools, in the very short timescale (a few ms), a TSO is able to establish in real time if the system can be stable or not and hence implement all the necessary countermeasures. In line with this considerations the present thesis aims at providing enabling methodologies for real-time small signal stability investigations.

March 2014

Recommendation #3

UCTE has to develop standard criteria for regional and inter-regional TSO co-ordination approach aiming at regional security management, from operational planning to real time, in terms of joint training, enhancement of exchanges of data, results of security analyses and foreseen remedial actions.

Recommendation #4

UCTE has to set up an information platform allowing TSO to observe in real time the actual state of the whole UCTE system in order to quickly react during large disturbances.

## 1.2 Objectives

The primary objective of this work is hence to develop estimation algorithms able to track in real time power oscillations on interconnected electrical systems. In order to support this complex activity each potential candidate should match the following requirements:

- *high accuracy*, to precisely describe what is really happening on power system, augmenting the TSO situational awareness;
- *low computational burden*, to be easily executed in parallel with other DSA tasks in the TSO central control centres;
- *high resiliency*, with respect to the data typology in input and to the major effects of wide area communication networks, to avoid false alarm or disregarding instability phenomena;
- *sufficient flexibility*, to be integrated into a real time simulation environments of a TSO.

Obviously, the achievement of this objectives without the partnership of the Italian TSO, Terna, would not have been possible. Terna provided all the support needed to include the developed algorithms, presented in the Chapters 3 and 4, in its own real time simulator-WAMS assisted.

### 1.3 Contributions

The scientific contribution is threefold:

- Do a performances analysis of the most popular (in literature) power system oscillations estimation techniques in actual large interconnected systems through the support of WAMS;
- Analyze the effects of some wide area communication network issues on the estimation algorithms behaviour;
- Propose three novel estimation algorithms to capture the modal content of the power system oscillations satisfying the requirements listed in the previous Section.

The first one is a two-step procedure consisting of a preliminary evaluation of the electromechanical modes number by using Hankel Singular Value Decomposition (HSVD) and a subsequent application of the VARiable PROjection Algorithm (VARPRO) to estimate the featuring parameters of each of them. The principal strength of this algorithm lies in its intrinsic ability to face with potential matters in wide-area communication networks such as noise and data packet dropouts.

The second one combines a recent signal decomposition theorem for separating an assigned signal into elemental ones, each of them characterized by a single frequency component and a robust preliminary nonlinear spectral analyzer, named the  $L_p$  periodogram. It aims at answering in a more simple and pragmatic manner to the main weaknesses of the Hilbert-Huang Transform (HHT) with respect to the major refinements in the relevant literature. This procedure results very appropriate for analyzing some critical cases of electromechanical oscillations, due to the  $L_p$  periodogram robustness against heavy-tailed noise and its intrinsic ability in estimating also closely spaced frequency components.

The third one is an algorithm specifically developed for estimating the damping of electromechanical oscillations in power systems. The method is based upon a generalization of the classical nonlinear least squares approach which employs further information concerning the finite Hilbert transform (HT) of the power signals. A semi-analytic procedure is tailored with the aim to get an expression of the Cauchy principal value integral to suitably include in the objective function of the least squares minimization. The methodology is found to be very accurate in damping estimation as well as resilient against a critical effect

March 2014

of the wide area communication networks, namely dropout packets. This is partially due to the inherent regularization action of the Hilbert transform in correspondence of the data lack.

## **1.4 Thesis Outline**

The thesis remainder is the following one.

Chapter 1 presents an comprehensive introduction of the thesis including the motivations for the research project, objectives and contributions of the research. Chapter 2 gives a brief description of the WAMS paradigm emphasising in its last part the need to pre-process real measured data, properly pre-classified, before to fed it to the estimation algorithms. Chapter 3 presents the classical and the advanced literature approaches for estimating electrical power systems dynamic. Chapter 4 contains the actual chief contribute of the thesis consisting in some recent advances in the employment of the HT for addressing the outlined issue. Chapters 5 collects several experimental findings obtained on synthetic signals, near real life signals sampled by IEEE test networks (e.g. Kundur two area test system, IEEE 68 bus test system) and real measured data in the ENTSO-e CESA. Chapter 7 concludes the work with interesting remarks drawing future developments and some interesting research lines.

## Chapter 2

# *Wide Area Monitoring Systems*

Nowadays, maintain the networks security high is one of the basic requirements for the TSO. In order to do this, the acquisition of more and more system information for predicting power systems dynamic evolution, in each operating condition, and for identifying the more appropriate and effective countermeasures which guarantee secure and stable operating conditions is essential. The major impediments in doing this are represented by the TSO inability to predict, with high accuracy, the system behavior but also the technological limits of the traditional Supervisory Control and Data Acquisition (SCADA) systems. A pragmatic solution to the highlighted issues is represented by the development of the WAMS. WAMS use sophisticated digital recording devices, i.e. PMU, to record and export GPS-synchronized, high sampling rate (6-60 samples/second) dynamic power system data. A Wide Area Control System (WACS) based on WAMS is a typical area network control system (NCS), in which the communication among sensors, actuators, and controllers occurs through a shared band-limited digital communication network [18]. Wide Area Protection System (WAPS) aims at enhance the actual interoperability level in a wide area by a proper management of the protection systems [19]. WAMPACS, Wide Area Monitoring Protection and Control System, is the term coined for describing a wide area system which implements monitoring, protection and control functionalities [20]. Further problems recognized by these infrastructures concern the research for robust identification algorithms for all the analysis that must be run in parallel in the central control centers. Not less significant, indeed particularly significant at the European level, is the integration with the neighbor national WAMS. The availability of large amounts of measurements coming from the system key points, i.e. from the primary substations, and the availability of computing power at low cost offer the possibility to perform a DSA in real time. One of the main functionality envisaged in the major WAMS currently in operation or under testing is exactly the power oscillations tracking, object of this thesis. In

this Chapter a generic description of the WAMS infrastructures is provided. Once analyzed the WAMS key elements, a focus on the Italian WAMS architecture and functionalities will be done. At last a characterization of the measurement data recorded by the WAMS and hence of the needed pre-processing operations for accomplishing real time small signal stability investigations will conclude the discussion.

## 2.1 WAMS: definition and constitutive sub-processes.

Wide area monitoring is a relatively new concept firstly introduced by Bonneville Power Administration (BPA) in the late 1980s [21]. A substantial part of the experience gained in WAMS is due to the American's utilities and research institutes. Although a precise and comprehensive definition was initially introduced, it has been updated downstream the widespread of PMU and high speed-low cost communication systems. WAMS process includes three different interconnected sub-processes, exactly data acquisition, data transmitting and data processing, respectively performed by measurement systems, communication systems and Energy Management Systems (EMS) [22].

Fig. 2.1 depicts an elementary view of the WAMS process. As can be argued, WAMS acquire power system data from conventional or advanced measurement devices and transmit it through proper communication systems to the control centres where a pre-processing stage aimed at implementing all the DSA functionalities is performed. The aforementioned three WAMS sub-processes employ data resources, applications and communication infrastructure as essential methodologies. Each of them will be discussed in detail in the rest of the Chapter.

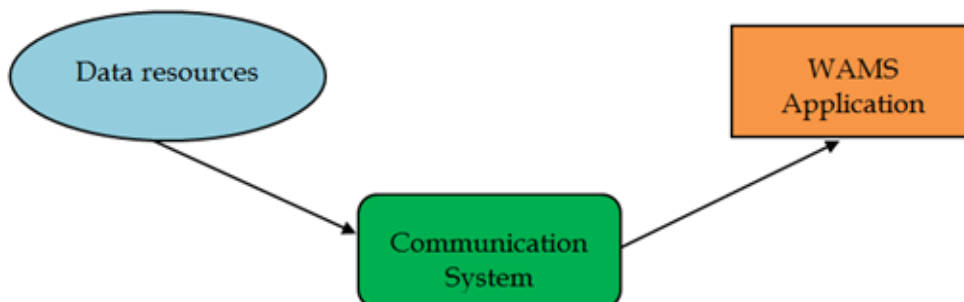


Fig. 2.1 – WAMS process in power systems.

### 2.1.1 Data resources

Data represent for WAMS the basic item to handle for executing analysis on the power systems. The presence of system data resources disseminated along the power systems, also called measuring devices, is hence ultimate. Power system data is very heterogeneous for this reasons a comprehensive classification is provided in Section 2.5. Nonetheless, at this stage, can be useful to classify it into two main group [23]: *operational* and *not operational*. The first group includes the instantaneous measurements of voltage and current (magnitudes and angles), breaker statuses, etc., recorded by the installed measurement devices. This data is continuously transmitted to the control centers through adequate communication systems for accomplishing all the analysis on the considered power system; sometimes it may be used locally for local decision making. The operational data is hence continuously conveyed to the control centers, i.e. through a continuous stream of data. This is the major difference between operational and non-operational data. Actually, the latter is typically conveyed at a specified time intervals (e.g. multiple of hours) or however at specified conditions. Furthermore, non-operational data is transmitted in different formats with respect to the operational one, e.g. numerical values, waveforms, COMTRADE (COMMon format for TRAnsient Data Exchange) etc. [23]. The non-operational data consists of records or logs of multiple events, e.g. series of faults, power fluctuations, disturbances and lightning strikes.

As well as for data, also the data resources of power systems can be classified into two groups:

- Operational data resources:
  - Supervisory Control and Data Acquisition;
  - Synchronized Phasor Measurement System.
  
- Non-operational data resources:
  - Circuit Breaker Monitor;
  - Digital Fault Recorder;
  - Digital Protective Relay.

#### *Supervisory Control and Data Acquisition*

SCADA is the generic name for a computerized system capable of collecting and processing data by applying operational controls over long distances. SCADA systems are typically used in power transmission and distribution and in the pipeline systems.

March 2014

In an electrical power system, a SCADA system provides three chief critical functions:

- Data acquisition;
- Supervisory control;
- Alarm display and control.

A SCADA system is essentially formed by both hardware and software component. SCADA hardware includes: a Master Terminal Unit (MTU) located in the control centers, one remote field site consisting of either a Remote Terminal Unit (RTU) or Programmable Logic Controllers (PLC) or Intelligent Electronic Devices (IED) and a communication system that provides communication route between remote site and the control center.

The MTU (sometimes called SCADA center, SCADA server, or master station) is located in the control center and may be considered the heart of a SCADA system. It performs many functions: (i) manages all communications, (ii) gathers data of RTU, (iii) stores obtained data and information, (iv) sends information to other systems, (v) commands system actuators that are connected to RTU and (vi) interfaces with operators.

The RTU is a stand-alone data acquisition and control unit that monitors and controls equipments at remote sites. RTU are generally microprocessor based and their functions are to control and acquire data from process equipments at the remote sites and to communicate obtained data to a master station, exactly MTU.

Traditional RTU only communicate with a MTU, while modern RTU may also communicate among together. In some cases, RTU can be configured as a relay. The may be classified in:

- Small-size RTU : include less than 10 to 20 analog and digital signals.
- Medium-size RTU: have 100 digital and 30 to 40 analog inputs.
- Large-sized RTU: with more inputs.

PLC is a small industrial computer. First it was employed for performing the logic functions carried out by electrical equipments, e.g. relays, drum switches, and mechanical timer/counters [24], but nowadays analog control is a standard part of it [25].

PLC are modular in nature, so that they can be expanded to monitor and control additional field devices at remote sites. Furthermore they can be programmed to perform local functions, even if communication with the master station is lost, because they have built-in microprocessor [26]. PLC are preferred to special-purpose RTU because they are more economical, versatile, flexible and configurable, physically compact and require less space than the RTU. The

communication systems provide communication routes between the master station and the remote sites, through private transmission media (e.g. fiber optic or leased line) or atmospheric means (wireless or satellite). There are three main physical communication architectures used in SCADA communications: point-to-point, multipoint and relay station architectures.

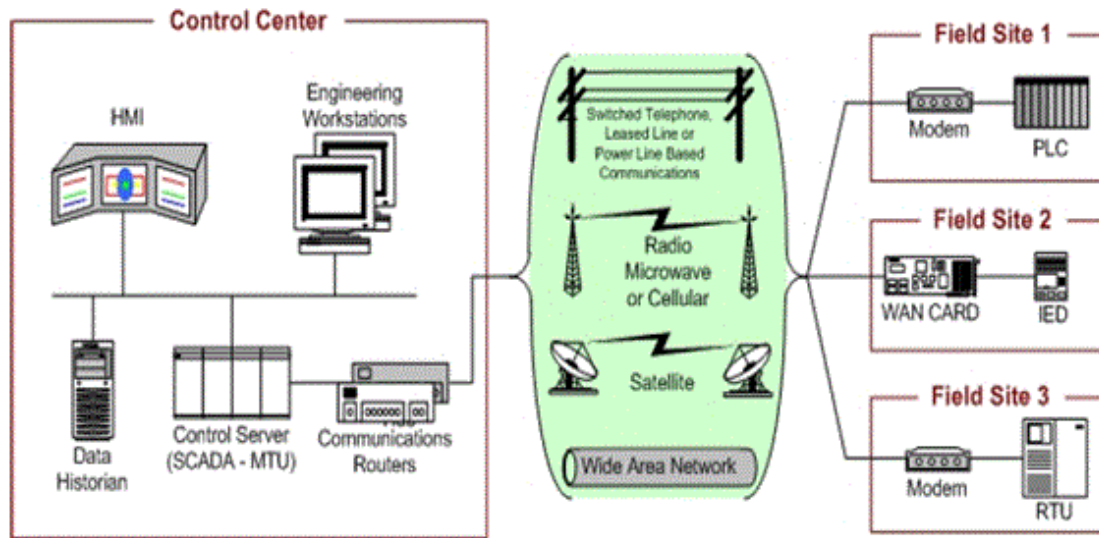


Fig. 2.2 – Supervisory and Control Data Acquisition architecture.

### *Synchronized Phasor Measurement System*

The Synchronized Phasor Measurement System (SPMS), firstly developed and introduced into the power systems in the mid-1980s, is a device able to measure currents and voltages, and calculate the angle between them. SPMS uses time received from GPS as its sampling clock, to synchronize measured angles. Moreover these systems can measure local frequency and rates of frequency changes, and may be customized to measure harmonics, negative and zero sequence quantities [27].

A SPMS consists of three main parts:

- Phasor Measurement Unit;
- Phasor Data Concentrator;
- Communication system.

March 2014

#### *Phasor Measurement Unit (PMU)*

The Phasor Measurement Unit (PMU) is a microprocessor based device, normally installed at remote sites, which measures the electrical waves (voltages and currents) on an electricity grid, at a typical rate of 48 samples per cycle (2400/2880 samples per second).

A phasor is a complex number that represents both the magnitude and phase angle of the sine waves measured on the electrical power systems. Phasor measurements that occur at the same time are called *synchrophasors*, term specifically used also for the PMU devices that allow their measurement. In typical applications PMU are synchronized from the common time source of a *Global Positioning System* (GPS). GPS provides 1 microsecond accuracy and this error translates into  $0.018^\circ$  for a 50 Hz system and  $0.021^\circ$  for a 60 Hz system. A PMU works in this way: first, the analog AC waveforms are synchronously sampled by an analogical/digital (A/D) converter for each phase, and the time from GPS satellites is used as input for a phase-lock oscillator and thereby, waveforms of the entire system are sampled with 1 microsecond accuracy. In the next step, PMU use digital signal processing techniques to calculate the voltage and current phasors. Also, line frequencies can be calculated by PMU at each site. The measured phasors are tagged by GPS time stamps and are transmitted to a PDC at the rates 30-60 samples per second. Therefore, it can be stated that PMU and RTU have almost the same tasks in the SPMS and SCADA systems. Phasor Data Concentrator (PDC) is a node in a system where phasor data from the number of PMU or PDC is correlated and fed out as a single stream to other applications. A PDC gathers data from several PMU, rejects bad data, aligns the time stamps and finally creates a coherent record of simultaneously recorded data. Also in this case it is possible to compare SPMS system with SCADA system and it can be noted that the tasks and functions of PDC in SPMS systems are almost the same as those in SCADA systems. The communication systems of SPMS may be similar to the SCADA communications in terms of technology, architecture and employed media, but in terms of streamed data they are different. Actually, the phasor data is continuous and streaming in nature while RTU data is transmitted to the master station either in specified time intervals or when master station requests it. Furthermore data of a PMU has more value than data provided by a RTU, so the indispensable requirements of the communication system are high bandwidth and low latency communications, which guarantee that all phasor data can be transmitted to PDC without any packet drops allowing a real time streaming between PMU and PDC.

March 2014

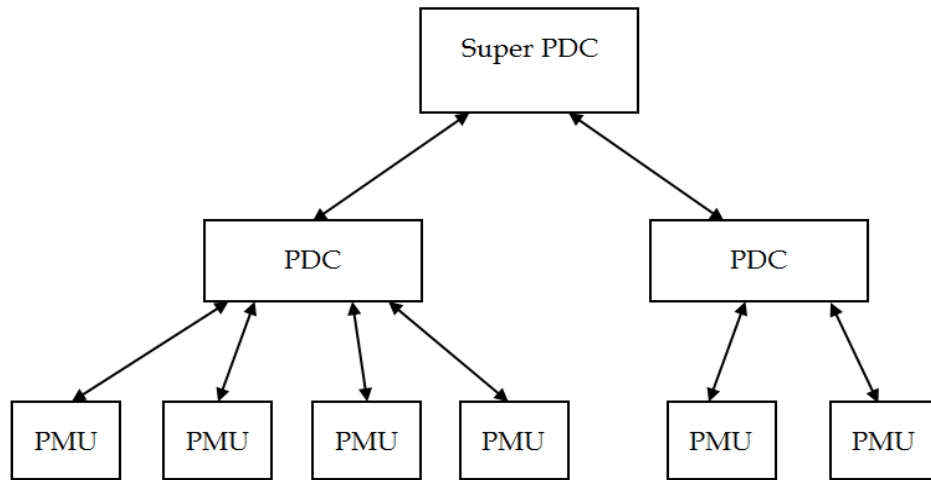


Fig. 2.3 – Synchronized Phasor Measurement System structure

#### *Digital Fault Recorder*

The Digital Fault Recorder (DFR) is typically installed in an important substation for recording highly accurate waveforms related to faults. The recorded data is a huge amount of analog and status data, respectively for [28]:

- pre-fault conditions;
- fault conditions;
- post-fault conditions.

This data may include maximum current, sequence of events, type of fault and the sequence of circuit breakers operations. DFR data can not be used in real time and in this case they are stored as samples for further offline processing. DFR has normally very high sample rate, about 64 to 356 samples per cycle.

#### *Digital Protective Relay*

In power system networks, protective relays are used to isolate the fault area and to reduce the impact of the faults from other parts of the system. At the beginning electromechanical relays were used, but from 1960s with the advent of electronic devices, electronic protection relays were introduced (nowadays partially replaced by the digital ones). A Digital Protective Relay (DPR) uses an advanced microprocessor to analyze voltages and currents and to detect faults in a power system. DPR can also measure and record analog and status data communicating with a centralized location. They collect current and voltage signals from instrument transformers and digitize them. Digital relays should

March 2014

act very fast, but this fact should defeat the accuracy of measured data. So commonly, to overcome this problem, lower sampling rates are applied to A/D converters. Firstly, DPR sample rates were 4 to 20 samples per cycle, nowadays they have been increased at 64 to 128 samples per cycle [29]. DPR data, compared to other data resources, are generally less accurate.

#### *Circuit Breaker Monitor*

The Circuit Breaker Monitor (CBM) is an electronic device that monitors circuit breakers. The CBM works in real time, capturing detailed information about each breaker, for properly acting or manually by the operator or automatically by the protection and control equipments when necessary. The CBM data is also structured in COMTRADE format.

## **2.2 WAMS applications/functionalities**

In power systems, WAMS applications are computer tools used to process the raw data measured by the data resources described in the previous Section. The purpose of these tools is to extract usable information for system operators, consumers and customers.

WAMS applications can be divided into three main groups:

- Generation;
- Transmission;
- Distribution.

Generation applications are basically devoted to monitor the generator's operating in order to know in real time the actual status and for instance supervise possible transient angle instability phenomena.

Transmission and sub-transmission applications operate at transmission, or sometimes at sub-transmission level. Historically, these tasks are performed by group of computer aided tools, the so called EMS. Some examples of conventional EMS applications are:

- State Estimation;
- Load flow ;
- Optimal power flow;
- Load forecast;
- Economical dispatch.

March 2014

Some modern WAMS applications include:

- Integrated Phasor Data Platform;
- Wide-Area Dynamic Monitoring and Analysis;
- Synchronized Disturbance Record and Replay;
- **Online Low-Frequency Oscillation Analysis;**
- Power Angle Stability Prediction and Alarming;
- PMU based State Estimation.

Combination of these modern applications with the conventional ones forms a modern EMS in the control centers.

In power systems, Distribution applications are also known as Automation applications. According to IEEE definition, Distribution automation systems have been defined as “*systems that enable a distribution company to monitor, coordinate, and operate distribution components and equipments from remote locations in real time*”. The Distribution applications have the objective to reduce costs, to improve service availability and to provide better services to the customers. Distribution applications may be classified into three main groups [30]:

- Substation automation;
- Feeder automation;
- Consumer-side automation;

## 2.3 WAMS Communication Infrastructures

The WAMS communication systems allow data delivery both from data resources to the control centers and from control centers to the system actuators. Particular attention should be paid to communication infrastructure which is as important as the electrical infrastructure. This is clear since a possible failure of communication network may cause huge problems in system operation and control, especially in the execution of WAMS applications. New communication systems are based on Open System Interconnection (OSI) layer model. This model is an effective architecture for explanation, designing, implementation, standardization and use of communications networks. The OSI reference model is composed by seven layers which are (i) physical, (ii) data link, (iii) network, (iv) transport, (v) session, (vi) presentation and (vii) application. WAMS data resources and WAMS applications normally operate at the upper layers of network models. Fig. 2.4 shows the map between OSI layers

and three major blocks of WAMS system which are data resources, applications and communication system.

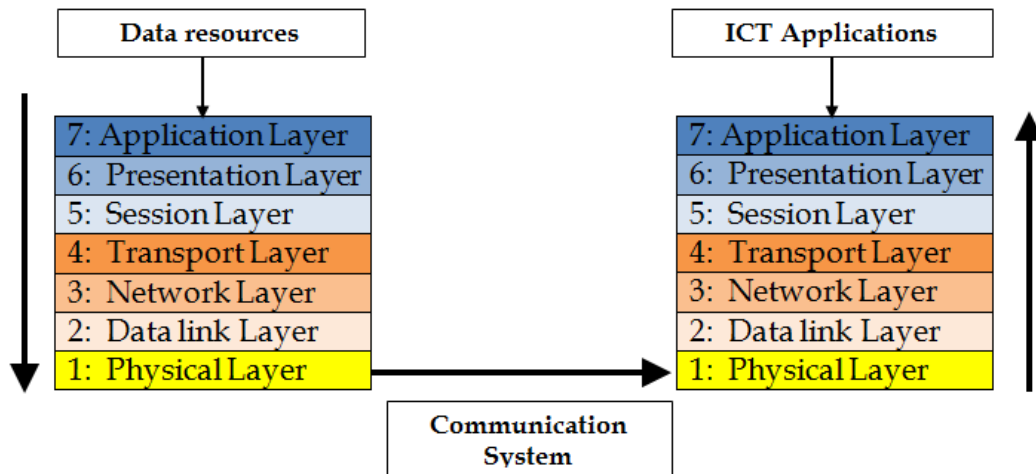


Fig. 2.4 - Layering in WAMS based on OSI reference model

The characteristics of the communication systems are seriously influenced by the characteristics of their media. Some of the chief characteristics of a transmission medium are: cost, bandwidth, propagation delay, security and reliability. Transmission media, as described below, can be classified as *guided* and *unguided* [30].

Guided transmission media guide the waves through a solid medium. Some examples are: twisted pair, coaxial cable, power transmission/distribution line and optical fiber.

Unguided transmission media provide instead a mean to transmit electromagnetic waves, but however this medium does not guide the signals. The atmosphere and outer space are some examples of unguided transmission media. They are usually referred to as wireless communication. Unlike guided media, for which the media itself has the most important role in characterizing the limitations of transmission, in the case of unguided media, the signal strength provided by wireless antenna is more important than the medium itself. Tables 2.1 lists the major guided and unguided media adopted in WAMS architectures describing their characteristics and providing a comparison among them in terms of bandwidth, latency and security.

TAB. 2.1 a) WIDE AREA MONITORING SYSTEMS GUIDED MEDIA

Media	Description	Band-width	Latency	Security
Optical fiber	OPC is employed for its flexibility to be bundled as a cable. In fiber cables the signal is a light wave either visible or infrared light. Types used in power industries are: Optical Power Ground Wire (OPGW) and All-Dielectric Self Supporting (ADSS).	High	Low	High
Power line carrier	PLC transfers critical communications directly through transmission lines, so a possible failure of the power system infrastructure (e.g. line outage) causes communication problems. According to the data rate values, PLC systems may be classified in two groups: <i>narrow band</i> and <i>broad band</i> .	Medium	Low	High
Leased Line	LL is used together with some technologies for transmitting wide area signals. These technologies are essentially the Digital Subscriber Line (DSL), able to provide digital data transmission over leased telephone circuits. According to their data rates and directionality of transmission, to distances to which those rates can be supported and to the size of the wire, several DLS versions can be identified.	Medium	Low-Medium	High

TAB. 2.1 b) WIDE AREA MONITORING SYSTEMS UNGUIDED MEDIA

Media	Description	Band-width	Latency	Security
WPAN	Wireless Personal Area Network is a network for interconnecting devices located around an individual person's workspace characterized by wireless connection. A WPAN uses some technology that allow the communication within a very short range (10 meters) One of the adopted technology in WPAN is the Bluetooth.	Low-Medium	Low-Medium	Low

March 2014

WLAN	<p>Wireless Local Area Network connects devices through a wireless distribution method. Wi-Fi is one of the most popular WLAN technologies and it provides high speed connection on short ranges.</p>	Low-Medium	Medium	Low
WMAN	<p>WiMAX, GPRS, GSM, CDMA and 3G mobile Carrier services are five <b>Wireless Metropolitan Area Network</b> technologies which are used for WMAN communication.</p> <p><b>Worldwide Interoperability for Microwave Access</b> (WiMAX) is a communication protocol which provides fix and fully mobile data networking. Its theoretical data rate is 70 Mbps with a range of up to a maximum of 50 km with a direct line of sight (LOS). Near line of sight (NLOS) conditions seriously limit their range.</p> <p><b>Global System for Mobile</b> (GSM) is a standard for mobile telephony system based on circuit-switching technology. Whith this technology connections are "always on".</p> <p><b>General Packet Radio Service</b> (GPRS) is a packet data bearer service over GSM system. It uses a packet radio principle to transfer data at high bandwidth. When a device transmits packages the bandwidth is used, GPRS has hence higher data speed than the GSM.</p> <p><b>Code Division Multi-Access</b> (CDMA) is another data networking technology for mobile communications. It allows all the users to utilize the entire frequency spectrum for all the time. CDMA can create 64 logical channels whereas 8 channels are available in GPRS.</p> <p><b>3G mobile Carrier services</b> provide new data carrier services for mobile users. For example some networks support High Speed Packet Access (HSPA) data communication with HSDPA standard to provide improved downlink speeds.</p>	Medium	Medium	Low
WWAN	<p>Wireless Wide Area Network, with satellite communications may be used in two cases: when a guided medium cannot be established between a remote site and the control center or when there is no line-of-sight between such a remote site and pre-installed communication network. One of the problem of satellites is their high latency that may create serious difficulties for some WAMS applications.</p>	Low-Medium	High	Low

---

## 2.4 Italian WAMS architecture and functionalities

The Italian WAMS project started in 2004 with the aim of achieving system benefits in terms of power system security and observability. In particular, running in real time several applications/functionalities, Italian WAMS is able to:

- improve the measure of proximity to critical conditions avoiding missing alarms;
- give a better synthetic vision of the Italian power system and its “neighbours”;
- enhance the possibility of very fast reactions.

In this way, the system is designed to support different applications and users. With reference to Control Room, Terna, the Italian TSO, is supported with real time trends and alarms related to:

- Voltage magnitude (low/high);
- Frequency (low/high);
- Angle difference (high);
- **Damping (low; from online oscillatory analysis function);**
- Voltage collapse;
- Under-frequency load shedding (from load shedding evaluation function);
- Islanding, loss of synchronism and frequency stability.

In addition, currently other functionalities of DSA are now under testing :

- Line thermal loading (under testing);
- SCADA state estimation integration with support of WAM platform (ongoing development);



Fig. 2.5 – Italian WAMS graphical user interface

Fig. 2.5 depicts a typical graphical user interface customized for the operators working in the control room. The Italian WAMS consists of a set of about 60 PMU data sources, a leased data network, based on Direct Numerical Circuit (DNC) channels and several WAMS applications/functionalities running at the National Control Center (NCC) in Rome. In NCC also data from three European partners converge this permitting to draw in real time dynamic behavioural of the entire interconnected synchronous European power system. The PMU installed on Italian network provides voltage and current phasors at the rate of 50 samples per second. This high data rate allows to monitor and control fast phenomena, such as transient stability.

Data is stored in a shared memory devoted to short-term archiving. The short-term memory has a matrix structure, whereas the rows are associated to a specific time tag (sampling time) and the columns are associated to the different measured quantities by the PMU. The shared memory is sized to allocate a maximum of 512 measures coming from 60 PMUs, for a duration of 30 minutes at a rate of 50 frames-per-second (i.e. one every 20 milliseconds). In parallel with the “fast” acquisition and the storage task a “slow” periodic saving of the data into a relational database is performed. In this way both the shared

memory are cleaned from oldest data which are then available for subsequent off line evaluations.

The relational database is structured in two levels. The first receives the data from the shared memory every 30 minutes and keeps them for the next 24 hours. The latter keeps the data collected in the last 30 days, with a sampling period of 100 milliseconds; it is updated on a daily basis.

Fig. 2.6 illustrates an integrated view of the Italian WAMS. From the central system, the real time acquired data are available to:

- Real time applications, embedded in central system;
- Distributed calculations on clients interfaces;
- External calculations on external servers (i.e. MATLAB® platform) via proprietary protocol or standard Object Linking and Embedding for Process Control (OPC);
- Visualization clients.

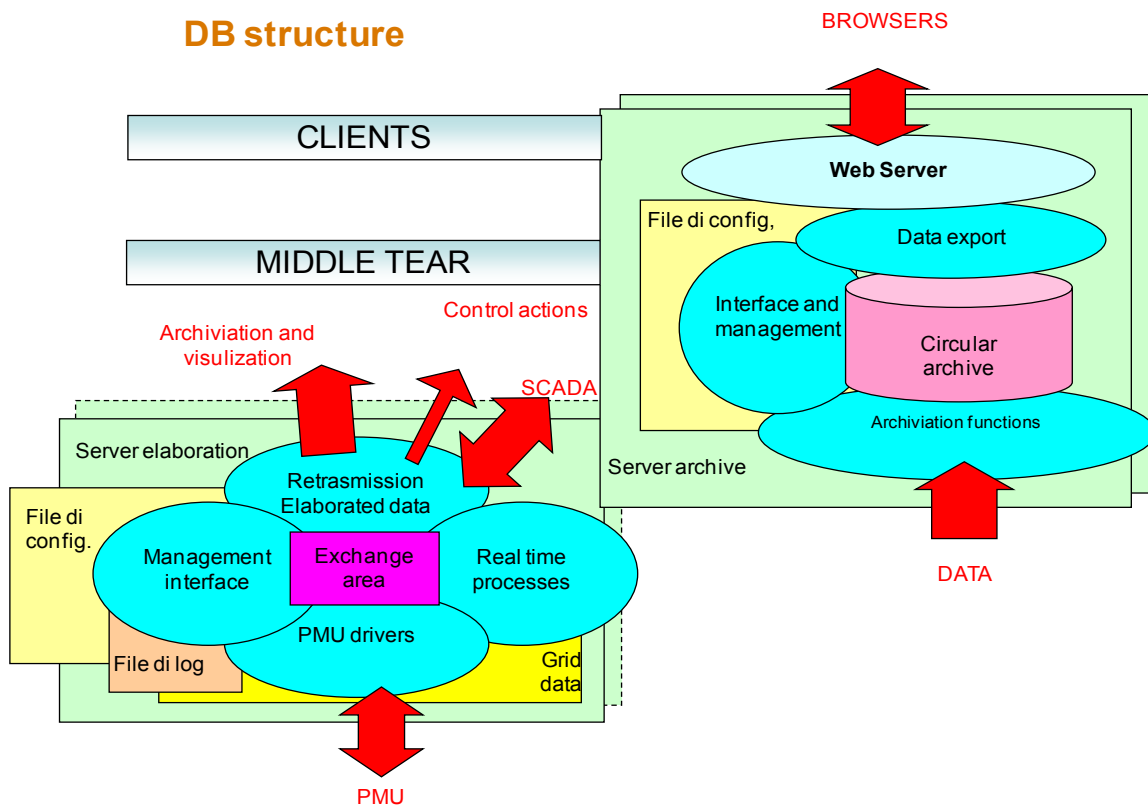


Fig. 2.6 – Italian WAMS architecture

A further feature of the Italian WAMS consists in a virtual acquisition function, a sort of “field emulator”, which feeds the acquisition and storage activities with data coming from sources such as text files. This function allows to test the

WAMS with critical situations of the power system, either recorded from the field or from simulation, thus testing the monitoring and alarm functions.

## 2.5 WAMS measurement data classification

The need for measurement data classification arises from the fact that, as already mentioned, algorithms' performance are situation-dependent that practically means data-dependent. For this reason it is essential to equip to the EMS in the control centres the most reliable estimation algorithms identifying the most indicated according to the situation on the basis of smart selection criteria. Generally, field measurement data can be classified into two categories: *typical* and *non-typical* data [31]. Typical data carries modal content information and can be described, in any case, by the identification algorithm mathematical framework. Non-typical data, such as for instance invalid data (NaN) and outliers, does not carry information about modal content and cannot be described by a generally linear model. Invalid data is often dropped data points, which may result from temporary communication and measurement device failure whereas outliers are values that significantly deviate from normal signal trend which may result for instance from a sensor failure. However, also transient data right before ringdown signals is considered non-typical, namely because it cannot be described by a linear prediction model. Typical data can be further categorized into *ambient data*, *ringdown oscillation* and *probing data*. Such a classification should not be intended as exhaustive. Ambient data is obtained when a system is working under an equilibrium condition and the major disturbance is from small amplitude random load changes [32]. Ringdown oscillation data occurs after some major disturbance, such as a line tripping, and it results in observable oscillations [33]. Probing data is obtained when low-level pseudo-random noise is intentionally injected into the system to test its performance [34]. Fig. 2.7 depicts a real measured voltage magnitude on the 220 kV Italian test system containing both ambient and ringdown data; part of the signal was intentionally polluted by non typical data, exactly invalids and an outlier. Information levels carried by the data categories just mentioned is quite different. The highest information density is carried by ringdown data which permits a fast convergence to the true oscillations parameters. Hence, a smart selection criterion that permits the switching towards those algorithms performing better on this data category at the onset of a transient phenomenon on the power system would be very useful in real time operation.

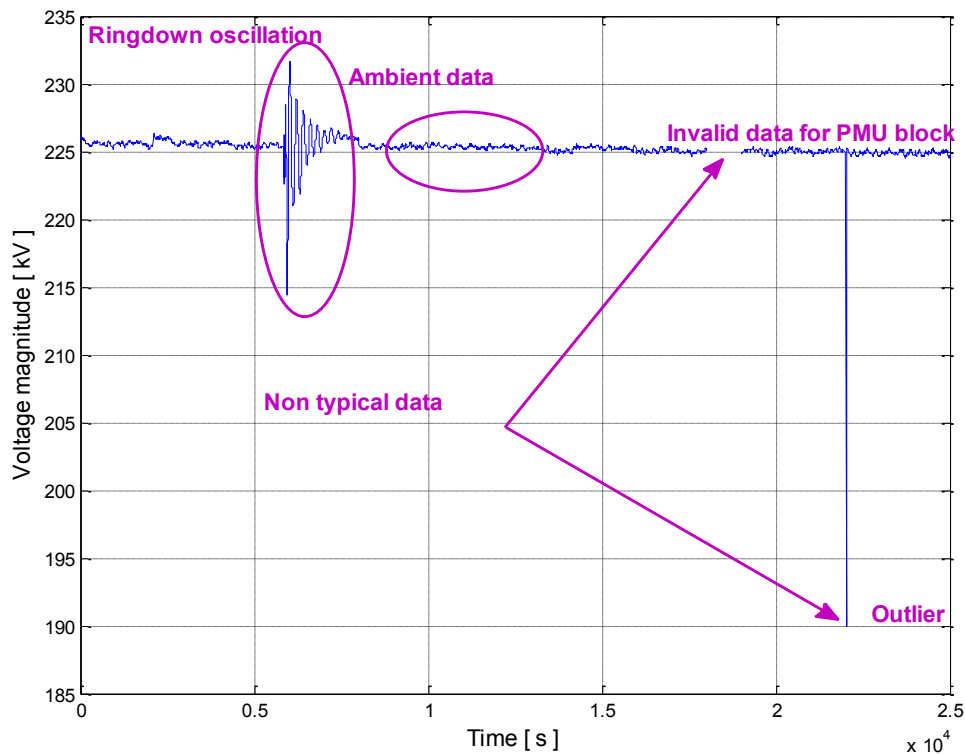


Fig. 2.7 – WAMS measurement data types

## 2.6 Preprocessing synchronized phasor measurement data for capturing power systems dynamic

The character of the synchronized phasor measurement data has been well-described in the previous Section. The direct application of an estimation algorithm of the electromechanical oscillations on the acquired signal, without a proper preprocessing action, may produce inconsistent outcomes. Generally, such an action consists in [35]:

- Removing defective data;
- Parceling data sets;
- Removing outliers;
- Interpolating missing samples;

- Removing trends;
- Filtering unwanted dynamics.

Missing data has a strong negative influence on the estimation technique performance. Obviously, the greater the magnitude of the data loss the worst is the algorithm response. If the magnitude is limited, indicatively lower than the 6 % of the data packet length, to omit the missing data and concatenate good data is best solution [36]. Besides this case, an interpolation process could be performed, as we already proposed in the reference [37] and it has been confirmed in [38]. On the contrary, if the magnitude of the data loss is not limited, concatenation will introduce artificial transients while interpolation will result in noise, therefore both the actions are to exclude. An outlier handling mechanism [37], [39], [40] should be incorporated in the preprocessing module in order to avoid artificial transients that deteriorate the estimation algorithms accuracy. Furthermore a trend removal and low pass filtering, accomplished both with Finite Impulse Response (FIR) and Infinite Impulse Response (IIR) filters is necessary to discard the modal content which does not contain important information about the power system dynamic. Fig. 2.8 depicts several functionalities of preprocessing. *Defective data removal* aims at discarding sequences of identical sample timestamps and/or values, samples with value zero and invalid measurements (e.g. NaN) caused by internal PMU failures occurrence. *Data parceling* aims at removing the missing samples to the data packets to furnish to the filters which are highly sensitive to potential gaps due to missing data. *Removal of outliers* aims at avoiding to induce artificial transients when the data is filtered. *Interpolation* aims at replacing missing samples as well as at removing data and outliers so capturing the signal trend: a linear interpolation may be simple and effective. *Removing of mean and low pass filtering* aims at suppressing the modal content which does not contain important information about the power system small signal stability.

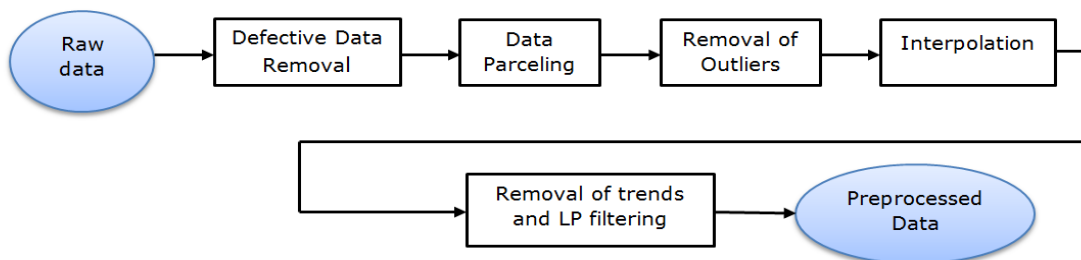


Fig. 2.8 – Preprocessing unit

## Chapter 3

# ***Power Systems Dynamic Estimation Techniques***

Power systems small-signal electromechanical dynamic properties have been traditionally investigated through modal analysis which implicitly considers a linearized model around the current steady-state operating point. On-line implementation in some actual wide area monitoring systems revealed modal analysis limits: (i) high computational times for large scale power systems not compatible for real time application (ii) difference between the actual system dynamic evolution and the one described by the adopted model due to the modeling uncertainties of some network components. For this reason, over the past two decades, several signal processing techniques have been tailored for estimating the modal content using only time-synchronized power system measurements. In this Chapter, an overview of the most popular and successful analysis techniques is presented. Unfortunately, no best estimator can be globally recognized among them due to the lack of an accepted definition of optimality, as already said. Performance comparison is made further complex from the fact that, generally, each technique has to properly be tuned because for instance it presents parameters chosen according to experience or through heuristic considerations. This action can often depend on the signal typology. Some techniques are hence appropriate for ringdown signals, others are adequate for ambient signal conditions; other ones show good performance in damping and frequency estimation if the observable modes number is known while may fail if it is not known in advance, some techniques could work better than others for noiseless sampled signals while could deteriorate their efficiency when the SNR decreases. The mentioned cases are only part of the actual encountered situations, to argue that a technique is wholly superior to the others appears hence pretentious and almost less clever. Nonetheless, either for reasons related to the specific methodological core advantages or for reasons related to the specific practicality, the attention of the power system community has recently moved towards the Hilbert transform-based techniques. The

March 2014

motivations behind this tendency is essentially due to the Hilbert transform ability to handle non-stationary and non-linear time series like the power systems oscillations as well as interesting properties not generally satisfied by other operators. It represents therefore, the starting point from which moves for developing advanced techniques aiming at solving the major drawbacks of the existing ones. The Chapter deals with the theoretical basis of several different estimation techniques postponing the numerical findings concerning computer simulations and actual experiments captured by the Italian WAMS.

### 3.1 Modal Analysis

As already mentioned, small signal stability analysis has been traditionally performed through the employment of the Modal analysis. This classical approach requires a detailed modelling of the electric power system under investigation. Such a model will be linearized around a certain equilibrium point, as described hereafter, in order to identify the electromechanical modes characteristics through the eigenvalue analysis. Before to do this, several basic concepts are introduced for favouring the topic understanding. Hence, the linearization process is then characterized. The latter introduces the state-matrix with respect to the whole stability analysis is focused.

#### 3.1.1 Fundamentals

Small signal stability is the ability of the power system to maintain the synchronism when subjected to small disturbances [41]. A disturbance is considered to be small if the power system model can be linearized around an equilibrium point. Hence, the employment of linear techniques allows the extraction of information about the power system dynamic that might be a valid aid in power system design and control.

The dynamic behaviour of an electrical power system can be described through the following set of  $n$  first order non linear differential equations:

$$\dot{x}_i = f_i(x_1, x_2, \dots, x_n, u_1, u_2, \dots, u_r; t) \quad \text{for } i = 1, 2, \dots, n \quad 3.1$$

March 2014

with  $n$  the system order and  $r$  the number of inputs. In matrix notation it can so be arranged:

$$\dot{\mathbf{x}} = \mathbf{f}(\mathbf{x}, \mathbf{u}, t) \quad 3.2$$

with

$$\mathbf{x} = \begin{bmatrix} x_1 \\ x_1 \\ \vdots \\ x_n \end{bmatrix} \quad \mathbf{u} = \begin{bmatrix} u_1 \\ u_1 \\ \vdots \\ u_r \end{bmatrix} \quad \mathbf{f} = \begin{bmatrix} f_1 \\ f_1 \\ \vdots \\ f_n \end{bmatrix}$$

where  $x$  is the state vector whose entries are the state variables  $x_i$  and  $u$  the system inputs vector affecting the system behaviour from the external. The left hand side of the Eq. (3.2) is the vector of the state variable derivative with respect to the time  $t$ . The system is said to be *autonomous* if the latter is not explicitly time-dependent, in this case Eq. (3.2) simplifies to:

$$\dot{\mathbf{x}} = \mathbf{f}(\mathbf{x}, \mathbf{u}) \quad 3.3$$

System response can be interrelated with the state variables and the system inputs in this way:

$$\mathbf{y} = \mathbf{g}(\mathbf{x}, \mathbf{u}) \quad 3.4$$

with

$$\mathbf{y} = \begin{bmatrix} y_1 \\ y_1 \\ \vdots \\ y_m \end{bmatrix} \quad \mathbf{g} = \begin{bmatrix} g_1 \\ g_1 \\ \vdots \\ g_m \end{bmatrix}$$

March 2014

which are respectively the system outputs vector,  $y$ , and the vector of non-linear functions relating the state and the input variables to the output variables,  $g$ .

State variables represent a minimal set of  $n$  linearly independent variables (not necessarily physical quantities such as voltage magnitudes and phases, rotor angles etc.) that, along with the inputs of the system, permits to describe the system dynamic behaviour. Through the employment of these variables the system *state* can be uniquely determined. The state of the system represents the minimum amount of information about the system, at any time instant  $t_0$ , that is necessary so that its future behaviour can be determined without reference to the input before  $t_0$  [42]. It can be represented in a  $n$ -dimensional Euclidean space named *state space*: whenever the system is not in equilibrium or the input is non-nil the system state change in time, tracing in this reference system a movement path called *state trajectory*.

The state trajectory points at nil speed, that is those points where all the state variables derivatives vanish, represent the system *equilibrium points* also known as singular points:

$$\mathbf{f}(\mathbf{x}_0) = 0 \tag{3.5}$$

with  $x_0$  the state vector at the equilibrium point. All the variables are constant and unvarying with time at a singular point. The system is linear if all the components of  $f$  are linear, in this case the system has only one equilibrium state (excluding the case of non-singular state matrix). On the contrary, a non linear system, such as an electrical power system, could have more than one equilibrium point.

Equilibrium points are inherently related to the system *stability* that for a non-linear system is dependent on the type and magnitude of the system inputs and on the initial state. Stability of a non linear system can be classified according to the state vector disposal in the state space [43]:

– *Small signal stability (local stability)*

The system is locally stable about an equilibrium point if, undergone to a small perturbation, it remains within a small region surrounding the equilibrium point. Furthermore, if, as  $t$  increases, the system returns to the original state, it is said to be *asymptotically stable* in the small.

March 2014

– *Finite stability*

If the state of the system is contained within a small region  $\Omega$ , the system is said to be *stable* in  $\Omega$ . The above definition of asymptotic stability can be easily extended to this case.

– *Global stability*

In the particular case in which  $\Omega$  is coincident with the entire finite space the system is said to be *globally stable*.

This thesis is essentially focused on investigations about the first mentioned class, therefore, in the following, the fundamental aspects to perform such an analysis are presented.

### 3.1.2 Power system model linearization

Small signal stability can be investigated by linearizing the non-linear system equations in (3.3) around the current equilibrium point. Let  $x_0$  be the initial state vector and  $u_0$  the input vector corresponding to the current equilibrium point; the following equation holds true:

$$\dot{\mathbf{x}}_0 = \mathbf{f}(\mathbf{x}_0, \mathbf{u}_0) = 0 \tag{3.6}$$

By perturbing the system from the above state applying a prefixed small perturbation  $\Delta$ , such that  $\mathbf{x} = \mathbf{x}_0 + \Delta\mathbf{x}$  and  $\mathbf{u} = \mathbf{u}_0 + \Delta\mathbf{u}$ , the new reached state will satisfy the (3.3), hence:

$$\dot{\mathbf{x}} = \dot{\mathbf{x}}_0 + \Delta\dot{\mathbf{x}} = \mathbf{f}[(\mathbf{x}_0 + \Delta\mathbf{x}), (\mathbf{u}_0 + \Delta\mathbf{u})] \tag{3.7}$$

The entity of the perturbations permits to expand in Taylor's series the non-linear functions in  $f(x,u)$ , by neglecting second and higher order terms. In this manner each entry of the linearized state vector derivative and of the linearized output vector derivative can be expressed as:

March 2014

$$\Delta \dot{\mathbf{x}}_i = \frac{\partial f_i}{\partial x_1} \Delta x_1 + \dots + \frac{\partial f_i}{\partial x_n} \Delta x_n + \frac{\partial f_i}{\partial u_1} \Delta u_1 + \dots + \frac{\partial f_i}{\partial u_r} \Delta u_r \quad \text{for } i = 1, 2, \dots, n \quad 3.8$$

$$\Delta y_j = \frac{\partial g_j}{\partial x_1} \Delta x_1 + \dots + \frac{\partial g_j}{\partial x_n} \Delta x_n + \frac{\partial g_j}{\partial u_1} \Delta u_1 + \dots + \frac{\partial g_j}{\partial u_r} \Delta u_r \quad \text{for } j = 1, 2, \dots, m \quad 3.9$$

State space representation can be arranged in compact manner as follows:

$$\Delta \dot{\mathbf{x}} = \mathbf{A} \Delta \mathbf{x} + \mathbf{B} \Delta \mathbf{u} \quad 3.10$$

$$\Delta \mathbf{y} = \mathbf{C} \Delta \mathbf{x} + \mathbf{D} \Delta \mathbf{u} \quad 3.11$$

where:

$\Delta \mathbf{x}$  is the  $n$ -dimensional state vector

$\Delta \mathbf{y}$  is the  $m$ -dimensional output vector

$\Delta \mathbf{u}$  is the  $r$ -dimensional input vector

The matrices  $\mathbf{A}$ ,  $\mathbf{B}$ ,  $\mathbf{C}$  and  $\mathbf{D}$  contain the partial derivatives evaluated at the equilibrium point around which the small perturbation is being analyzed:

$$\mathbf{A} = \begin{bmatrix} \frac{\partial f_1}{\partial x_1} & \dots & \frac{\partial f_1}{\partial x_n} \\ \dots & \dots & \dots \\ \frac{\partial f_n}{\partial x_1} & \dots & \frac{\partial f_n}{\partial x_n} \end{bmatrix} \quad \mathbf{B} = \begin{bmatrix} \frac{\partial f_1}{\partial u_1} & \dots & \frac{\partial f_1}{\partial u_r} \\ \dots & \dots & \dots \\ \frac{\partial f_n}{\partial u_1} & \dots & \frac{\partial f_n}{\partial u_r} \end{bmatrix}$$

$$\mathbf{C} = \begin{bmatrix} \frac{\partial g_1}{\partial x_1} & \dots & \frac{\partial g_1}{\partial x_n} \\ \dots & \dots & \dots \\ \frac{\partial g_m}{\partial x_1} & \dots & \frac{\partial g_m}{\partial x_n} \end{bmatrix} \quad \mathbf{D} = \begin{bmatrix} \frac{\partial g_1}{\partial u_1} & \dots & \frac{\partial g_1}{\partial u_r} \\ \dots & \dots & \dots \\ \frac{\partial g_m}{\partial u_1} & \dots & \frac{\partial g_m}{\partial u_r} \end{bmatrix}$$

March 2014

$\mathbf{A}$  is called state matrix or plant matrix,  $\mathbf{B}$  is the control matrix or input matrix,  $\mathbf{C}$  is the output matrix and  $\mathbf{D}$  is the feed-forward matrix defining the portion of input which appears directly in the output. Matrices size can be easily deduced above.

Eqs (3.10) and (3.11) in the Laplace domain can be so formulated:

$$s\Delta\mathbf{x}(s) - \Delta\mathbf{x}(0) = \mathbf{A}\Delta\mathbf{x}(s) + \mathbf{B}\Delta\mathbf{u}(s) \quad 3.12$$

$$\Delta\mathbf{y}(s) = \mathbf{C}\Delta\mathbf{x}(s) + \mathbf{D}\Delta\mathbf{u}(s) \quad 3.13$$

A rigorous solution of the state equations can be derived by solving for  $\Delta\mathbf{x}(s)$  and evaluating  $\Delta\mathbf{y}(s)$  in the manner that follows:

$$(\mathbf{sI} - \mathbf{A})\Delta\mathbf{x}(s) = \Delta\mathbf{x}(0) + \mathbf{B}\Delta\mathbf{u}(s) \quad 3.14$$

$$\Delta\mathbf{x}(s) = (\mathbf{sI} - \mathbf{A})^{-1}[\Delta\mathbf{x}(0) + \mathbf{B}\Delta\mathbf{u}(s)] = \frac{\text{adj}(\mathbf{sI} - \mathbf{A})}{\det(\mathbf{sI} - \mathbf{A})}[\Delta\mathbf{x}(0) + \mathbf{B}\Delta\mathbf{u}(s)] \quad 3.15$$

whence

$$\Delta\mathbf{y}(s) = \mathbf{C} \frac{\text{adj}(\mathbf{sI} - \mathbf{A})}{\det(\mathbf{sI} - \mathbf{A})} [\Delta\mathbf{x}(0) + \mathbf{B}\Delta\mathbf{u}(s)] + \mathbf{D}\Delta\mathbf{u}(s) \quad 3.16$$

As can be noted, the Laplace transform of  $\Delta\mathbf{x}$  and  $\Delta\mathbf{y}$  are formed by two components: one depending on the initial conditions, named *free component*, and one depending on the inputs, named *zero-state component*. The poles of  $\Delta\mathbf{x}(s)$  and  $\Delta\mathbf{y}(s)$  are the roots of the equation  $\det(\mathbf{sI} - \mathbf{A}) = 0$  which expanded represents the well-known *characteristic equation*. The values of the Laplace variable  $s$  that satisfy the characteristic equation are known as the *eigenvalues* of the state matrix  $\mathbf{A}$ .

### 3.1.3 Stability analysis and related concepts

The eigenvalues of the state matrix  $\mathbf{A}$  are those values of the scalar parameter  $\lambda$  for which there exist non trivial solutions (e.g. other than  $\Phi=0$ ) to the equation  $\mathbf{A}\Phi = \lambda\Phi$ . To find the eigenvalues, the latter can be re-formulated as  $(\mathbf{A} - \lambda\mathbf{I})\Phi = 0$ , hence for avoiding trivial solutions the following condition must be imposed :

$$\det(\mathbf{A} - \lambda\mathbf{I}) = 0 \tag{3.17}$$

Once expanded, Eq. (3.17) provides the so called characteristic equation whose solution  $\lambda = [\lambda_1, \lambda_2, \dots, \lambda_n]^T$  contains the eigenvalues of  $\mathbf{A}$  that can be real or complex (in the latter case conjugate pairs always occur if  $\mathbf{A}$  is real). If  $\lambda_k$  is real, a non-oscillatory mode can be identified. If  $\lambda_k$  is complex, e.g.  $\lambda_k = \sigma_k \pm i\omega_k$ , two oscillatory modes can be identified having the form:

$$z_{k1} = M_{1k} e^{(\sigma_k + i\omega_k)t} \quad \text{and} \quad z_{2k} = M_{2k} e^{(\sigma_k - i\omega_k)t} \tag{3.18}$$

where  $M_{1k}$  is the complex conjugate of  $M_{2k}$ . Hence, the output of the system is real, and the complex mode will have the form  $Ze^{\sigma t} \sin(\omega t + \varphi)$  in any output. The values of  $Z$  and  $\varphi$  depend on the magnitude and the typology of input and on which output is selected. The real part of  $\lambda_k$  indicates whether an electromechanical oscillation:

- **Decays**, if  $\sigma_k$  is negative;
- **Persist** with constant amplitude, if  $\sigma_k$  is zero;
- **Grows**,  $\sigma_k$  is positive.

Hence a negative real part indicates a damped oscillation whereas a positive real part represents an unstable oscillation of growing amplitude. Obviously, in the first case the larger its magnitude, the faster the decay. The most common manner to measure the oscillations damping levels is through the *damping ratio* which is defined as:

March 2014

$$\xi = \frac{-\sigma}{\sqrt{\sigma^2 + \omega^2}} \quad 3.19$$

Damping ratio measures the decay rate of the oscillation amplitude. Since oscillatory modes have a wide characteristic frequency range, the employment of this index rather than the time constant of decay (and hence than the simple *damping coefficient*  $\sigma$ ) is considered more appropriate for expressing the degree of damping [44].

Instead, the mode oscillation frequency can be determined from the imaginary part of  $\lambda_k$ :

$$f_k = \frac{\text{imag}(\lambda_k)}{2\pi} = \frac{\omega_k}{2\pi} \quad 3.20$$

Each eigenvalue  $\lambda_k$  has a correspondent  $n$ -column vector  $\Phi_k$  satisfying the Eq. (3.21) which is called *right eigenvector*:

$$\mathbf{A}\Phi_k = \lambda_k\Phi_k \quad \text{for } k = 1, 2, \dots, n \quad 3.21$$

and a correspondent  $n$ -row vector  $\psi_k$  satisfying the following one, named *left eigenvector*.

$$\psi_k\mathbf{A} = \lambda_k\psi_k \quad \text{for } k = 1, 2, \dots, n \quad 3.22$$

Sometimes left eigenvector is defined as the transpose of  $\psi_k$  which means that it is equal to the right eigenvector of the transpose of the state matrix  $\mathbf{A}$ .

Since for determining  $\Phi_k$  the homogeneous equation  $(\mathbf{A} - \lambda\mathbf{I})\Phi_k = 0$  has to be solved,  $k\Phi_k$  (with  $k$  any scalar multiplier) is also solution. Thus, eigenvectors are determined only to within a scalar multiplier. The left and right eigenvectors corresponding to different eigenvalues  $\lambda_i$  and  $\lambda_j$  are orthogonal, so  $\psi_j\Phi_i = 0$  while in the case of eigenvectors corresponding to the same eigenvalue  $\lambda_j$ ,  $\psi_j\Phi_j = C_j$ , with  $C_j$  a non-zero constant. A common practice is hence to normalize these vectors, so that  $\psi_j\Phi_j = 1$  (e.g.  $C_j = 1$ ).

Eigenvectors are very useful for determining the way in which a mode contributes to a specific state by exploiting the orthogonality property. Actually,

March 2014

thanks to the mentioned property any vector of length  $n$  (states number) can be expanded in terms of the right eigenvectors:

$$\Delta \mathbf{x} = \sum_{k=1}^n \mathbf{z}_k \Phi_k \quad 3.23$$

The coefficient  $\mathbf{z}_i$  can be found by pre-multiplying the Eq. (3.23) by the  $i^{\text{th}}$  left eigenvector  $\Psi_i$ . Because the left and right eigenvectors are orthogonal, only the  $i^{\text{th}}$  term of the resulting summation is nonzero, hence by scaling the eigenvectors so that  $\Psi_i \Phi_i = 1$ ,  $\mathbf{z}_i$  can be so determined:

$$\mathbf{z}_i = \Psi_i \Delta \mathbf{x} \quad 3.24$$

The coefficient  $\mathbf{z}_i$  in the state vector expansion of the Eq. (3.23) are essentially the oscillation modes. To reach a closed-form expression of these modes one can substitute the Eq. (3.23) in the state equation (3.10) and then pre-multiply by the  $i^{\text{th}}$  left eigenvector  $\Psi_i$  as before:

$$\dot{\Delta \mathbf{z}}_i = \lambda_i \mathbf{z}_i + \Psi_i \mathbf{B} \Delta \mathbf{u} \quad \text{for } i = 1, 2, \dots, n \quad 3.25$$

In this manner, the  $n$  coupled linear differential equations of the state matrix have been decoupled in the same number of linear differential equations whose solutions, that can be determined by solving separately each of them<sup>1</sup>, are exactly the modes of oscillation.

Generally, by applying any input perturbation  $\Delta \mathbf{u}$ , the  $i^{\text{th}}$  mode varies in time as follows:

$$\mathbf{z}_i(t) = \int_0^t e^{\lambda_i(t-\tau)} \Psi_i \mathbf{B} \Delta \mathbf{u}(\tau) d\tau \quad 3.26$$

---

<sup>1</sup> A special procedure must be applied in the case of equal eigenvalues since in this case the modal equations can not be completely decoupled [45]

March 2014

Hence, the state vector  $\Delta \mathbf{x}$  can be obtained by summing all the modes  $\mathbf{z}_i$  multiplied by the corresponding right eigenvector as in the Eq. 3.23. In conclusion, from a physical point of view the right eigenvector measures how each mode is distributed among the system states, it is also known as *mode shape*. On the other hand, the left eigenvector jointly with the control matrix  $\mathbf{B}$  and the input vector  $\Delta \mathbf{u}$  affects the amplitude of the mode.

### *Eigenvalue Sensitivity*

Now, differentiating the Eq. (3.21) with respect to  $a_{ij}$  (element of the  $i^{\text{th}}$  row and  $j^{\text{th}}$  column of  $\mathbf{A}$ ), pre-multiplying by  $\boldsymbol{\psi}_k$  and by keeping in mind that  $\boldsymbol{\psi}_k \boldsymbol{\Phi}_k = 1$  and  $\boldsymbol{\psi}_k (\mathbf{A} - \lambda_k \mathbf{I}) = 0$  one has:

$$\boldsymbol{\psi}_k \frac{\partial \mathbf{A}}{\partial a_{ij}} \boldsymbol{\Phi}_k = \frac{\partial \lambda_k}{\partial a_{ij}} \quad 3.27$$

where all the elements of  $\partial \mathbf{A} / \partial a_{ij}$  are zero, except that one placed at the  $i^{\text{th}}$  row and  $j^{\text{th}}$  column which is unitary. Therefore,

$$\frac{\partial \lambda_k}{\partial a_{ij}} = \boldsymbol{\psi}_{ki} \boldsymbol{\Phi}_{jk} \quad 3.28$$

Thus, the sensitivity of the eigenvalue  $\lambda_k$  to the element  $a_{ij}$  of the state matrix is equal to the product of the elements  $\boldsymbol{\psi}_{ki}$  and  $\boldsymbol{\Phi}_{jk}$ .

### *Participation factor*

Let now consider the sensitivity of  $\lambda_k$  to the  $a_{ii}$  element of the state matrix:

$$p_k = \frac{\partial \lambda_k}{\partial a_{ii}} = \boldsymbol{\psi}_{ki} \boldsymbol{\Phi}_{ki} \quad 3.29$$

In power system analysis it is termed *participation factor* of the  $i^{\text{th}}$  state in the  $k^{\text{th}}$  mode, e.g. the product of the  $i^{\text{th}}$  element in the  $k^{\text{th}}$  left (row) eigenvector and the  $i^{\text{th}}$  element in the  $k^{\text{th}}$  right (column) eigenvector. Participation factor is a nearly good indicator of the state importance to the mode from a control viewpoint, in

March 2014

particular for the optimal placement of the power system stabiliser (PSS). Actually, if for each mode, the corresponding participation factor of the generator angular velocity is:

- **Nil**, adding damping at that generator will produce any stability improvements;
- **Real positive**, adding damping at that generator will increase the damping of the mode;
- **Real negative**, adding damping at that generator will reduce the damping of the mode.

The addition of mechanical damping at the generators shafts result in the modification of the diagonal terms of the state matrix (which become negative) referred to the generators angular velocity. Anyway, some ambiguity issues can arise in the case of equal system matrix eigenvalues due to the intrinsic definition in the Eq. (3.29).

### 3.2 Fourier transform based methods

Without any doubt, the first approach historically facing the problem of estimating electromechanical oscillations parameters were those ones based on Fourier Transform. Fourier Transform methods basically analyze the signal frequency spectrum composed by its component sine waves according to the Fourier series concept. If  $x(t)$  is a periodic signal with period  $T$  and hence fundamental angular frequency  $\omega_0 = 2\pi/T$  (rad/s), its Fourier series can be expressed as [46]:

$$x(t) = \frac{a_0}{2} + \sum_{n=1}^{\infty} (a_n + a_n^*) \cos(n\omega_0 t) + i(a_n - a_n^*) \sin(n\omega_0 t) \quad 3.30$$

with  $a_n$  the coefficient of Fourier

$$a_n = \frac{2}{T} \int_{t^*}^{t^*+T} x(t) e^{-in\omega_0 t} dt \quad 3.31$$

Often rewritten as:

$$x(t) = \frac{a_0}{2} + \sum_{n=1}^{\infty} b_n \cos(n\omega_0 t) + c_n \sin(n\omega_0 t) \quad 3.32$$

$$\text{with} \quad b_n = \frac{2}{T} \int_{t^*}^{t^*+T} x(t) \cos(n\omega_0 t) dt \quad \text{and} \quad c_n = \frac{2}{T} \int_{t^*}^{t^*+T} x(t) \sin(n\omega_0 t) dt$$

keeping in mind the periodicity of  $x(t)$  and the lack of potential inter-frequency components. For our purposes, it is convenient to employ a numerical method for such an evaluation, that is the Discrete Fourier Transform (DFT):

$$F_D(x(k\Delta T)) = X(m\Delta\Omega) = \frac{1}{\sqrt{N}} \sum_{m=1}^N x(i\Delta T) e^{-im\Delta\Omega\Delta T} \quad 3.33$$

whereas  $F_D(\cdot)$  denotes the DFT,  $\Delta T$  the sampling time,  $N$  is the number of points in the sample (which must span an integer number of  $x(t)$  periods) and  $\Delta\Omega$  which is the DFT frequency domain resolution. DFT can be easily computed through an exact evaluation method, namely Fast Fourier Transform (FFT), that exploiting some symmetry properties of the complex exponential, calculates the DFT with reduced computational burden with respect to the (3.33). As the sampling interval becomes smaller and smaller, and as  $N$  goes to infinity, it is can be demonstrated that the DFT becomes the Fourier Transform (FT) [47]:

$$\mathfrak{F}\{x(t)\} = F(j\omega) = \int_{-\infty}^{\infty} x(t) e^{-i\omega t} dt \quad 3.34$$

and its inverse is

March 2014

$$\mathfrak{F}^{-1}\{F(j\omega)\} = x(t) = \frac{1}{2\pi} \int_{-\infty}^{\infty} F(j\omega)e^{j\omega t} d\omega \quad 3.35$$

Therefore, by decomposing  $x(t)$  in a sum of sine and cosine functions (harmonics) according the mathematical tools just described, the power system modes number and the associated frequency can be estimated. As far as the damping coefficient is concerned, it can be determined from the signal DFT according to the Eq. (3.36):

$$\sigma = \frac{2\pi}{BW} \quad 3.36$$

where  $BW$  is the 3dB bandwidth of the spectrum  $|X(m\Delta\Omega)|$  which exactly corresponds to the damping coefficient in the case of single component signal. Alternative definitions are proposed by Yoshida, Bertocco, Rife-Vincent and so on enclosed in reference [48].

In practice, FFT is used jointly with a sliding window along the entire duration of the signal. The latter is considered stationary in this window, hence its size must be chosen small enough to satisfy the assumption. Obviously, the lower bound to this size is represented to the necessary time for all the electromechanical modes to establish themselves. The choice of the proper window size is not trivial due to the fact that power system oscillatory signals are generally non-linear and non-stationary, stochastic in nature, containing possible nonlinear high order interactions and characterized by closely-spaced frequency components.

FFT would hence require harmonic components to track non-stationary real time-synchronized signals dissipating energy over a wide frequency range making little physical sense. For this reason some researchers have proposed Short-time Fourier Transform (STFT) as potential candidate to replace it [49], [50]. STFT uses a time window for analyzing the signals into a two-dimensional domain, time-frequency, in order to search for a compromise between time-domain resolution and frequency-domain resolution. The main problem relies in the fact that once a particular size for the time window is chosen, such a window width has to be kept constant for all frequencies. Rigorously speaking, STFT calculates a succession of spectra localized about a time  $t$  by firstly multiplying the signal by a window  $w(\tau)$  centred about  $t = \tau$ . The longer the window  $w(\tau)$ , the better the frequency resolution but at the expense of a reduced time-domain resolution and vice versa. Furthermore the optimal

rectangular window length is a function of the instantaneous signal frequency which is in turn unknown a priori, hence the STFT is limited in its usefulness [51]. Although sometimes the approximation of linear and stationary signal is not so far from the reality, no sufficient information can be obtained with the FT-based methods. For this reason, during the past, new estimation techniques are proposed replacing the basic idea to analyze the spectrum of the power system oscillatory signals with the one to analyze the instantaneous frequency and amplitude. This concepts will be introduced in this Chapter.

### 3.3 Prony Analysis

Among linear analysis techniques, Prony analysis, developed by Hauer, Demeure, and Scharf [52], allows to estimate power systems small-signal dynamic properties implementing a curve-fitting decomposition procedure able to separate a simulated or real measured signal into  $n$  exponential damped sinusoids:

$$x(t) = \sum_{k=1}^n A_k e^{\sigma_k t} \sin(\omega_k t + \varphi) \quad \text{for } k = 1, 2, \dots, n \quad 3.37$$

When this assumption is made, the technique is also recognized as a ringdown analyzer, this can be easily deduced from the concepts furnished in the Section 2.5. Since it basically deals with an eigenvalue-based technique, Prony analysis furnishes the real and imaginary parts of the mode, corresponding respectively to the damping coefficient  $\sigma$  and to the modal damped frequency  $\omega$ . Mode amplitude  $A$  and phase shift  $\varphi$  can also be readily determined so permitting to reconstruct the original signal in the time domain from the feasible components identified. The fundamental assumption of such a technique is the signal stationary, that being not always met, implies sometimes a not meaningful decomposition. Factors such as window length and sampling rate can affect the accuracy with which a non-stationary signal is approximated by a sum of stationary modes [47]. The mathematical framework of this technique is not reported since the next subsection presents an its improved version that through some expedients enhances the inherent consistency of the method with respect to the noisy.

Ongoing research into the study of power systems electromechanical dynamic revealed the practical inapplicability of the Prony analysis in presence of high noise levels and possible non-stationary real time-synchronized measurements. This has motivated the progressive abandonment in the use of this technique for estimating the modal behaviour of actual power systems favouring the development of new estimation techniques most of which are described in this Chapter.

### 3.4 Tufts-Kumaresan method

Despite the Prony analysis concerns presented in the previous Section, some actual WAMS projects around the world implement tasks of electromechanical oscillations tracking through the use of this technique. Some practical experiences come, for instance, from two regional electrical power systems in China [53], [54]. However, as already mentioned, some problems arise for increasing signals noise levels. A valid help in this sense is represented by an interesting refinement developed by D.W. Tufts and R. Kumaresan, consisting in a Prony extension to signals embedded in noise.

More specifically, Tufts and Kumaresan in [55], [56] introduced a method, in the sequel TKM, for spectral estimation in presence of white Gaussian noise which is a quite satisfactory assumption for the cases of interest. The TKM mathematical framework preserves the assumption to model a certain observed data sequence  $x(n)$  with a sum of  $M$  exponential damped sinusoids corrupted by complex white Gaussian noise:

$$x(n) = \sum_{k=1}^n a_k e^{s_k n} + w(n) \quad \text{for } n = 0, 1, \dots, N-1 \quad 3.38$$

whereas,  $s_k = \sigma_k + i\omega_k$ , with  $\sigma_k$  the damping factor of  $k^{\text{th}}$  exponential damped sinusoid,  $\omega_k$  the angular frequency of  $k^{\text{th}}$  exponential damped sinusoid lying in the interval  $(0, 2\pi)$  and  $a_k$  the complex amplitude. TKM manages complex and conjugate data samples of the signal in backward direction through the following linear prediction equation:

$$\begin{bmatrix} y(1) & y(2) & \dots & y(L) \\ y(2) & y(3) & \dots & y(L+1) \\ \vdots & \vdots & \ddots & \vdots \\ y(N-L) & y(N-L-M) & \dots & y(N-1) \end{bmatrix} \begin{bmatrix} b(1) \\ b(2) \\ \vdots \\ b(L) \end{bmatrix} = \begin{bmatrix} y(0) \\ y(1) \\ \vdots \\ y(N-L-1) \end{bmatrix} \quad (3.39)$$

or in equivalent compact manner:

$$\mathbf{A}\mathbf{b} = -\mathbf{h} \quad (3.40)$$

In Eq. (3.40)  $\mathbf{A}$  is the linear prediction matrix,  $\mathbf{b}$  is the vector of the backward prediction coefficients. From the equations system (3.40), the following homogeneous system can be rewritten:

$$\mathbf{A}_H \mathbf{b}_H = 0 \quad (3.41)$$

Where  $\mathbf{A}_H$  is the partition  $(\mathbf{h} | \mathbf{A})$  and  $\mathbf{b}$  is the vector  $[1 \ b_1 \ b_2 \ \dots \ b_L]^T$ . If the signal is noiseless and  $L$  is chosen equal to  $M$ , the zeros of the polynomial

$$B(z) = 1 + b_1 z^{-1} + \dots + b_L z^{-L} \quad (3.42)$$

fall outside the unit circle because the linear prediction equation is written in reversed time direction. But if  $L > M$  this choice permits to increase the estimation accuracy of the zeros location. Actually, in this case the Eq. (3.42) has also  $L-M$  extraneous zeros and the system (3.41) is over-determined; by choosing the solution which minimizes the norm  $\|\mathbf{b}\|^2 = \|b_1\|^2 + \|b_2\|^2 + \dots + \|b_L\|^2$ , the extraneous  $L-M$  zeros fall inside the unit circle [57].

This is pointed out in Fig. 3.1 for the following bi-modal signal ( $M=2$ )

$$x(n) = e^{(-0.1+i3.3)n} + e^{(-0.2+i2.6)n} \quad (3.43)$$

with  $n = 0,1,2,\dots,99$ . As can be noted the  $M$  actual signal components fall outside the unitary circle with respect to the  $L-M$  extraneous components ( $L=20$  in the specific case and hence  $L-M=18$ ).

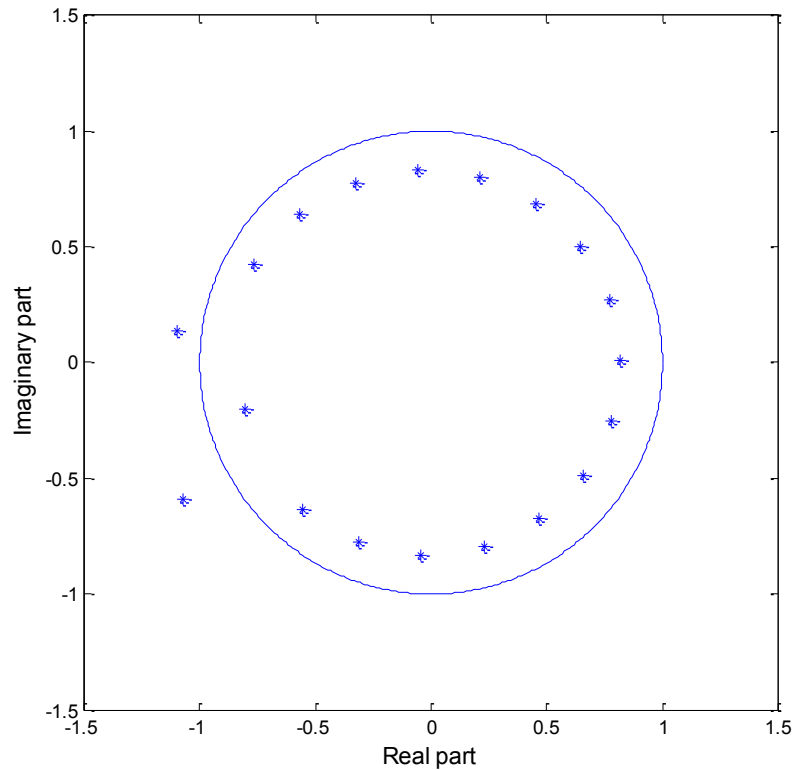


Fig. 3.1 – Zeros' displacement of the  $B(z)$  polynomial in Tufts-Kumaresan method

In this way it is facilitated the distinction among the actual zeros and the extraneous zeros of  $B(z)$  associated to the noise. When the signal is corrupted by high noise, several perturbations are introduced in the vector of the backward prediction coefficients and the adoption of the Singular Value Decomposition (SVD) is necessary. The basic idea is that the linear prediction matrix  $\mathbf{A}$  has  $L$  non-zero singular values with the principal singular values  $s_1, s_2, \dots, s_M$  greater than the  $s_{M+1}, s_{M+2}, \dots, s_L$  which are associated to the noise. Hence, depending on the adequate  $M$  value chosen for describing the characteristic power system modes, the SVD of the linear prediction matrix can be written as:

$$\mathbf{A}_M = \mathbf{U} \mathbf{S}_M \mathbf{V}^T \quad 3.44$$

where  $\mathbf{S}_M$  is a diagonal matrix which has the first  $M$  elements equal to  $s_1, s_2, \dots, s_M$  and the other  $L-M$  elements are imposed to be equal to zero.

After this SVD truncate, the system in Eq. (3.40) becomes:

$$\mathbf{A}_M \mathbf{b} = -\mathbf{h} \quad 3.45$$

The values of vector  $\mathbf{b}$  are found as:

$$\mathbf{b} = -\mathbf{A}_M^+ \mathbf{h} \quad 3.46$$

where  $\mathbf{A}_M^+$  is the pseudoinverse matrix of  $\mathbf{A}_M$ . Therefore, from the roots of the polynomial in the Eq. 3.42 the values of the frequencies and of the damping factors of all the power system modes can be easily derived by using the following relationships:

$$\alpha_k = \text{real}(\log(e^{s_k})) \quad 3.47$$

$$f_k = \frac{\text{imag}(\log(e^{s_k}))}{2\pi} \quad 3.48$$

### 3.5 Non linear least squares methods

The non linear least squares (NLS) method considered in this thesis for estimating the parameters of electromechanical oscillations is the VARiable PROjection (VARPRO) method. VARPRO application requires the knowledge of the system order, and hence of the electromechanical modes number, that can be achieved for instance through Hankel Singular Value Decomposition (HSVD). Given  $m$  observations  $(t_i, x_i)$ , let us define  $\mathbf{x} = [x_1, x_2, \dots, x_m]^T$  the observation data vector. This can represent almost any variable representative of the power system operating, adequately processed if necessary such as generators angular speed, voltage magnitude, active power flow etc. The fundamental HSVD steps are summarized in the following, leaving its full discussion to the relevant literature (i.e. in [58], [59]) in order to do not complicate the discussion:

March 2014

1. Construct the Hankel data matrix,  $\mathbf{H}$ , having dimension  $L \times M$ .  $L$  must be chosen greater than  $M$ , and in turn,  $M$  greater than  $K$ , with  $K$  the modes number;

$$\mathbf{H} = \begin{bmatrix} y_1 & y_2 & \cdots & y_M \\ y_2 & y_3 & \cdots & y_{M+1} \\ \vdots & \vdots & \cdots & \vdots \\ y_L & y_{L+1} & \cdots & y_{L+M+1} \end{bmatrix} \quad 3.49$$

2. Calculate the Hankel matrix SVD:

$$\mathbf{H}_{L \times M} = \mathbf{U}_{L \times L} \mathbf{S}_{L \times M} \mathbf{V}_{M \times M}^+ \quad 3.50$$

3. Eliminate the singular values that correspond to the noise and compute an updated Hankel matrix having rank equal to  $K$ :

$$\mathbf{H}_K = \mathbf{U}_{L \times K} \mathbf{S}_K \mathbf{V}_{M \times K}^+ \quad 3.51$$

where  $\mathbf{U}$  is an unitary matrix,  $\mathbf{V}^+$  is the hermitian conjugate of the unitary matrix  $\mathbf{V}$  and  $\mathbf{S}$  is a rectangular diagonal matrix with real and positive singular values  $\sigma_1 \geq \sigma_2 \geq \dots \geq \sigma_n$ .

4. Compute the eigenvalues of the  $\mathbf{Z}$  matrix in least squares sense:

$$\mathbf{Z} = \left( \mathbf{A}_{L \times K}^T \mathbf{A}_{L \times K} \right)^{-1} \mathbf{A}_{L \times K}^T \mathbf{B}_{L \times K} \quad 3.52$$

where  $\mathbf{A}$  and  $\mathbf{B}$  are obtained from  $\mathbf{U}$  by eliminating the first and the last row. In this way, the modes number simply corresponds to the estimated eigenvalues number.

The knowledge of the system model order allows us to develop a proper framework to process in the next proposed non-linear least square algorithm, exactly called the Variable Projection Method [60]. In order to clarify the VARPRO's working, let us consider that the number of oscillation modes detected by the HSVD is  $k$ , each represented by a damped sinusoid. Hence the following representation can be adopted:

March 2014

$$x(t) = \sum_{i=1}^k A_i e^{\sigma_i t} \sin(2\pi f_i t + \varphi_i) \quad 3.53$$

where  $\sigma_i$  and  $f_i$  are respectively the damping factor and the frequency of each mode to determine since they are unknown. Eq. (3.53) can be rewritten as:

$$\begin{aligned} x(t) &= \sum_{i=1}^k \left[ A_i e^{\sigma_i t} \sin(2\pi f_i t) \cos \varphi_i + A_i e^{\sigma_i t} \cos(2\pi f_i t) \sin \varphi_i \right] \\ &= \sum_{i=1}^k \left[ C_{1i} e^{\sigma_i t} \sin(2\pi f_i t) + C_{2i} e^{\sigma_i t} \cos(2\pi f_i t) \right] \end{aligned} \quad 3.54$$

VARPRO peculiarity is to perform the fit only with respect to the non-linear parameters of the model above, exactly  $\sigma_i$  and  $f_i$ , computing the remaining linear parameters, exactly  $C_{1i}$  and  $C_{2i}$ , through linear least squares, with no need for initial estimates. The objective function structure,  $L$ , is the one in the Eq. (3.55), whereas  $\alpha$  is the vector of linear parameters  $[C_{11}, C_{21}, C_{12}, C_{22}, \dots, C_{1k}, C_{2k}]^T$ ,  $\beta$  is the vector of non-linear parameters  $[\sigma_1, f_1, \sigma_2, f_2, \dots, \sigma_k, f_k]^T$  and at last  $\Theta$  is the fitting function that, at the instant  $t_k$ , depends only on the non-linear parameters  $\Theta = \Theta(\beta; t)$ .

$$L(\alpha, \beta) = \sum_{j=1}^h \left[ x(t_j) - \Theta(\beta, t_j) \alpha \right]^2 = [x - \Theta(\beta) \alpha]^T [x - \Theta(\beta) \alpha] = \|[x - \Theta(\beta) \alpha]\|^2 \quad 3.55$$

with  $h$  the number of available samples.

The minimization can be reformulated as:

$$L(\hat{\alpha}, \hat{\beta}) = \min_{\beta} \left\{ \min_{\alpha} \|x - \Theta(\beta) \alpha\|^2 \right\} \quad 3.56$$

As can be noted, if  $\beta$  is fixed, the internal minimization is a linear least squares problem, therefore the minimum of the linear parameters vector is:

$$\alpha(\beta) = \Theta^+(\beta) x \quad 3.57$$

where  $\Theta^+$  is the pseudo-inverse matrix of  $\Theta = \Theta(\beta)$ . Eq. 3.56 can be reformulated as:

$$\mathbf{L}(\hat{\boldsymbol{\alpha}}, \hat{\boldsymbol{\beta}}) = \min_{\boldsymbol{\beta}} \left\{ \min_{\boldsymbol{\alpha}} \left\| \mathbf{x} - \boldsymbol{\Theta}(\boldsymbol{\beta}) \boldsymbol{\Theta}^+(\boldsymbol{\beta}) \mathbf{x} \right\|^2 \right\} \quad 3.58$$

which depends only on the parameters in  $\boldsymbol{\beta}$  that can be easily calculated through an iteration procedure, allowing consequently to determine  $\boldsymbol{\alpha}$  and to reconstruct the original signal. Summarizing, VARPRO method, through the described procedure, furnishes angular frequency  $f_i$  and damping coefficient  $\sigma_i$  collected in  $\boldsymbol{\beta}$  for each elemental component. Hence, by solving a linear least squares problem, amplitude and phase of the single component, implicitly collected in the  $\boldsymbol{\alpha}$  elements, can be computed according to the following relationships:

$$A_i = \sqrt{C_{1i}^2 + C_{2i}^2} \quad 3.59$$

$$\varphi_i = \text{tg}^{-1} \left( \frac{C_{2i}}{C_{1i}} \right) \quad 3.60$$

### 3.6 Extended Complex Kalman Filter

As already said an electromechanical oscillation can be often modelled with a sum of  $M$  exponential damped sinusoids corrupted by complex white Gaussian noise  $w(n)$ . An equivalent expression to the one in (3.38) is the following:

$$\mathbf{x}(n) = \sum_{k=1}^M \mathbf{a}_k e^{\lambda_k n T_s} + w(n) = \sum_{k=1}^M \mathbf{a}_k e^{(-\sigma_k + j\omega_k) n T_s} \quad \text{for } n = 0, 1, \dots, N-1 \quad 3.61$$

where now  $T_s$  is the sampling interval,  $\mathbf{a}_k$  the complex amplitude of the  $k^{\text{th}}$  mode and at last  $\lambda_k = -\sigma_k + j\omega_k$  is the signal eigenvalue referred to the  $k^{\text{th}}$  power system oscillatory mode, with  $\sigma_k$  the damping factor and  $\omega_k$  the angular frequency.

The Extended Complex Kalman Filter (ECKF) implementation requires to organize the observed signal  $\mathbf{x}(n)$  in a state space representation. The method is called extended complex Kalman filter because it applies the standard Kalman

filter to a nonlinear system with additive white noise by continually updating a linearization around the previous state estimate [61]. The state transition and the observation models of the ECKF are hence [62]:

$$\mathbf{z}_{n+1} = \mathbf{f}(\mathbf{z}_n) \quad 3.62$$

$$\mathbf{x}_n = \mathbf{H}\mathbf{z}_n + \mathbf{w}_n \quad 3.63$$

The  $k^{\text{th}}$  eigenvalue at the  $n^{\text{th}}$  instant is represented by two states denoted as  $z_n(k)$  and  $z_n(k+1)$  expressed as:

$$z_n(k) = e^{(-\sigma_k + i2\pi f_k)T_s} \quad 3.64$$

$$z_n(k+1) = a_k e^{(-\sigma_k + i2\pi f_k)nT_s} \quad 3.65$$

Hence, the acquired signal is characterize through  $2M$  number of states (with  $M$  the number of exponential damped sinusoids). In this way the state transition and the observation models become:

$$\begin{bmatrix} z(1) \\ z(2) \\ z(3) \\ z(4) \\ \vdots \\ z(2M-1) \\ z(2M) \end{bmatrix} = \begin{bmatrix} z(1) \\ z(1)z(2) \\ z(3) \\ z(3)z(4) \\ \vdots \\ z(2M-1) \\ z(2M-1)z(2M) \end{bmatrix} \quad 3.66$$

$$z(n) = z_n(2) + z_n(4) + \dots + z_n(2M) + w_n \quad 3.67$$

with the measurement/observation matrix defined as:

$$\mathbf{H}_{1 \times 2M} = [0 \ 1 \ 0 \ 1 \ \dots \ 0 \ 1] \quad 3.68$$

The ECKF operations are hence summarized in the following:

$$\hat{\mathbf{z}}_{n|n} = \hat{\mathbf{z}}_{n|n-1} + \mathbf{K}_n (\mathbf{x}_n - \mathbf{H} \hat{\mathbf{z}}_{n|n-1}) \quad 3.69$$

$$\hat{\mathbf{z}}_{n+1|n} = \mathbf{f}(\hat{\mathbf{z}}_{n|n}) \quad 3.70$$

$$\mathbf{K}_n = \hat{\mathbf{P}}_{n|n-1} \mathbf{H}^T \left[ \mathbf{H} \hat{\mathbf{P}}_{n|n-1} \mathbf{H}^T + \mathbf{R}_n \right]^{-1} \quad 3.71$$

$$\hat{\mathbf{P}}_{n|n} = \hat{\mathbf{P}}_{n|n-1} - \mathbf{K}_n \mathbf{H} \hat{\mathbf{P}}_{n|n-1} \quad 3.72$$

$$\hat{\mathbf{P}}_{n+1|n} = \mathbf{F}_n \hat{\mathbf{P}}_{n|n} \mathbf{F}_n^T + \mathbf{Q}_n \quad 3.73$$

$$\mathbf{F}_n = \left. \frac{\partial \mathbf{f}(\mathbf{z}_n)}{\partial \mathbf{z}_n} \right|_{\mathbf{z}_n = \hat{\mathbf{z}}_{n|n}} \quad 3.74$$

where  $R_n$ ,  $Q_n$ ,  $K$  and  $P$  are respectively the measurement noise correlation factor, the process noise correlation factor, the filter gain and the covariance matrix. Careful tuning of the measurement and process noise correlation factor, must be done in order to avoid biased estimations and to make the estimation procedure less sensible against the noise. The damping factor and the oscillatory frequency of the  $k^{\text{th}}$  mode can be computed from the estimated state vector  $z_n$  as follows:

$$\sigma_k = \frac{-\ln(z_n(2k-1))}{T_s} \quad 3.75$$

$$f_k = \frac{\tan^{-1} \frac{\text{Im}\{z_n(2k-1)\}}{\text{Re}\{z_n(2k-1)\}}}{2\pi T_s} \quad 3.76$$

This estimation algorithm is able to track ringdown oscillations poorly damped, this means for instance that a fast transient event, like a capacitor switching can not be effectively monitored. Nonetheless, it enhances the performance of the standard linear Kalman filter adopted for the purpose. Estimation algorithm

performance are dependent from the initial conditions of the states, for this reason in reference [63] the employment of the HSVD is proposed for improving the convergence speed and the estimation accuracy. In this thesis we employ HSVD to detect the system order (which is the number of intrinsic modes captured in the signal) which highly affects the consistence of the obtained results by the VARPRO application. Due to the filter transient behaviour in the computing of the parameters in (3.75) and (3.76) at the initial and final part of the observation window, these values are provided as average value over a convenient one where the filter output is stable around the actual electromechanical oscillation parameter to estimate (respectively damping coefficient or frequency).

### 3.7 Hilbert transform based methods

Recently, both for reasons related to the specific methodological core advantages and for reasons related to the specific practicality, the attention of the power system community has recently moved towards the employment Hilbert transform-based methods. The motivations behind this tendency is essentially due to the HT ability to handle non-stationary and non-linear time series like the power systems oscillations and due to some remarkable properties not satisfied from other operators that will be discussed later. Being moreover specifically designed for working on non-stationary and non-linear time series, it exactly matches the characteristics of the electromechanical oscillations which are the inherent non-stationarity and the development on different time scales. HT offers the possibility to direct examine the instantaneous signal properties such as frequency, damping coefficient, amplitude and phase. For this reasons Hilbert-Huang transform has been extensively applied in various engineering fields such as mechanics, biomedical, geophysics as a direct tool for understanding the behaviour of complex systems. Apart from the electromechanical modes identification, HHT application fields in electrical power systems studies are essentially the power quality analysis [64] and faults diagnostic [65]. Basically, HHT is an empirically based data analysis method consisting of two parts. The first part is the Empirical Mode Decomposition (EMD) which attempts to decompose the original signal in elemental signals called *intrinsic mode functions* (IMF), through an iterative procedure named *sifting algorithm*. The second part is the ordinary HT application on each IMF with the aim of determining *instantaneous frequencies* and the *instantaneous amplitudes*. The manner of determining the instantaneous amplitude and frequency values is generally called *analytical*

*signal* method. Instantaneous damping factor or damping ratio estimates can be also easily achieved through simple mathematical derivations.

### 3.7.1 Empirical Mode Decomposition

Empirical mode decomposition developed by Norden Huang [66] is a signal decomposition algorithm based on a successive removal of elemental signals called intrinsic mode functions derived through an iterative procedure termed sifting algorithm [67], [68], [69]. It is more like an empirical method than a theoretical tool. The lack of an analytical formulation prevents any theoretical analysis: this justifies the empirical denotation of the method. In order to be an IMF a certain basis function must verify the following conditions:

- The number of extrema and the number of zero-crossings differ by, at most, one along the entire signal duration;
- The mean value of the envelope defined by the local maxima and the envelope defined by the local minima is nil at any point.

In practice, a signal with any significant DC component can not be an IMF. Sifting algorithm, through three main steps, aims at subtracting away the large-scale features of the signal repeatedly until only the fine-scale features remain. Therefore the signal to decompose  $x(t)$  can be seen as sum of elemental functions  $c(t)$  having finite-scale trait, namely IMF, and a residue  $r(t)$ ,  $x(t)=c(t)+r(t)$ . The first important difference with respect the previously analyzed method is that, in this case, no assumption on IMF model is made.

In the following the sifting algorithm steps are listed:

1. Set  $r_0(t)=x(t)$  at the stage  $k = 1$ ;
2. Extract the  $k^{\text{th}}$  IMF through the following procedure
  - 2.1 Set  $m=1$  and  $h_{m-1}(t)=r_{k-1}(t)$ ;
  - 2.2 Identify the successive local minima and the local maxima for  $h_{m-1}(t)$ . The time spacing between successive maxima is defined to be the time-scale of these successive maxima;
  - 2.3 Interpolate the local minima and the local maxima with a cubic spline to form an upper envelop  $e_{\max, m-1}(t)$  and a lower one  $e_{\min, m-1}(t)$  for the entire data span;

March 2014

#### 2.4 Calculate the instantaneous mean of the envelopes

$$i_{m-1}(t) = 0.5(e_{\max, m-1}(t) + e_{\min, m-1}(t))$$

and refresh the estimate  $h_m(t) = h_{m-1}(t) - i_{m-1}(t)$  such that  $e_{\min, m-1}(t) \leq h_m(t) \leq e_{\max, m-1}(t)$ . Set  $m = m + 1$ ;

2.5 Repeat the steps 2.2-2.4 until  $h_m(t)$  satisfies a set of predetermined stopping criteria (follows the pointed out conditions to recognize an IMF). Then set  $c_k(t) = h_m(t)$ ;

3. Get an improved residue  $r_k(t) = r_{k-1}(t) - c_k(t)$ . Set  $k = k + 1$  and repeat the whole step 2 until the number of extrema in  $r_k(t)$  is less than two.

In this manner, low-amplitude riding waves and asymmetries with respect to the local mean are eliminated in the time series making the wave profile more balanced. The IMF 'sifted' from this algorithm are orthogonal in nature and appear in decreasing order of frequency. At the end of the decomposition procedure only the first  $n$  IMF identified contain informative content, the remaining ones together with the residue  $r_n(t)$  contain less relevant non sinusoidal informative content. Unlike linear transform techniques such as Prony analysis or Fourier techniques, EMD separates components exhibiting 'fast' (in some sense) variations from components varying more slowly without making any assumptions about the components model. Actually, while linear transform techniques adopt for each component an exponentially modulated sinusoid to carry out a fitting process for determining fundamental constant parameters such as frequency, damping coefficient, amplitude and phase shift, IMF do not approximate any specific model. The chief EMD difference with respect to the linear transform techniques relies in the concept of instantaneous frequency which overcomes the assumption of constant frequency for each component. Fourier analysis furnishes the frequency component from its time period, which is the time taken to complete one stationary time period. As already said, since electromechanical oscillations are generally non-stationary waveform characterized by incomplete time periods, the frequency definition is hence not trivial.

### 3.7.2 Hilbert transform

The Hilbert Transform of a real signal  $x(t)$  is defined as:

$$H[x(t)] = x_H(t) = \frac{1}{\pi} \text{P.V.} \int_{-\infty}^{\infty} \frac{x(\tau)}{t - \tau} d\tau = \frac{1}{\pi} \text{P.V.} \int_{-\infty}^{\infty} \frac{x(t - \tau)}{\tau} d\tau \quad 3.77$$

where the integral is considered as a Cauchy principal value because of the possible singularity at  $\tau=t$  or  $\tau=0$ . Alternative definition reverse the sign. As can be noted from the Eq. (3.77), the HT represents the convolution between the transformer  $1/\pi t$  and the function  $x(t)$ ,  $H[x(t)] = (1/\pi t) * x(t)$ . A basic property of this operator is to shift the phase of the negative frequency components by  $\pi/2$  radians and the phase of the positive frequency components by  $-\pi/2$  radians. For this reason HT is often interpreted as a  $\pi/2$  phase shift operator. The signal  $x(t)$  and its Hilbert transform  $x_H(t)$  can be arranged in a canonical representation called *analytical signal*  $g(t)$ :

$$g(t) = x(t) + jx_H(t) = A(t)e^{i\vartheta(t)} \quad 3.78$$

where

$A(t) = \sqrt{x^2(t) + x_H^2(t)}$  is the analytical signal amplitude;

$\vartheta(t) = \tan^{-1}(x_H(t)/x(t))$  is the analytical signal phase.

The instantaneous angular frequency of  $g(t)$  can be calculated as:

$$\omega(t) = \frac{d\vartheta_u(t)}{dt} \quad 3.79$$

where  $\vartheta_u(t)$  is the continuous unwrapped phase,  $\vartheta_u(t) = \vartheta(t) + \Lambda(t)$ , with  $\Lambda(t)$  an integer multiple of  $\pi$ -valued function designed to ensure a continuous phase function. Hence the instantaneous frequency is evaluated as:

March 2014

$$f(t) = \frac{\omega(t)}{2\pi} = \frac{x(t)\dot{x}_H(t) - x_H(t)\dot{x}(t)}{2\pi[x^2(t) + x_H^2(t)]} \quad 3.80$$

As far as the instantaneous damping coefficient is concerned, it can be derived through simple mathematical derivations from the instantaneous frequency and magnitude. Rewriting the expression (3.78) according to the following one:

$$g(t) = A(t)e^{j\theta(t)} = \Sigma(t)e^{-\alpha(t)+i\theta(t)} \quad 3.81$$

with  $\alpha(t)$  the time-dependent decay function modelled as:

$$\alpha(t) = \int_0^t \sigma(\tau) d\tau \quad 3.82$$

Dividing the derivative of  $g(t)$  by the same  $g(t)$  one obtains:

$$\frac{\dot{g}(t)}{g(t)} = \left[ \left( -\sigma(t) + \frac{\dot{\Sigma}(t)}{\Sigma(t)} \right) + i\omega(t) \right] \quad 3.83$$

where

$$\operatorname{Re} \left( \frac{\dot{g}(t)}{g(t)} \right) = \frac{\dot{A}(t)}{A(t)} \quad 3.84$$

The instantaneous damping can hence be calculated:

$$\sigma(t) = -\frac{d\alpha(t)}{dt} = -\left[ \frac{\dot{A}(t)}{A(t)} - \frac{\dot{\Sigma}(t)}{\Sigma(t)} \right] \quad 3.85$$

March 2014

simplified in the case of purely exponential signal into the following relationship:

$$\sigma(t) = -\frac{d\alpha(t)}{dt} = -\frac{\dot{A}(t)}{A(t)} \quad 3.86$$

since  $\Sigma(t)$  is constant and its derivative nil.

### *HT Properties*

The great interest in HT relies on the fact that this operator satisfies three important properties [70] not satisfied from the major part of the other operators: amplitude continuity and differentiability, phase independence of scaling and homogeneity and at last the harmonic correspondence. A brief focus on Bedrosian theorem in Hilbert Transform is also reported since it represents a central point of the signal decomposition theorem presented in the Chapter 4 as valid alternative to the EMD.

#### *P.1 Amplitude Continuity and Differentiability*

By applying a small perturbation  $\delta x(t)$  to the original signal  $x(t)$ , the following relationship maintains:

$$H[x(t) + \delta x(t)] \rightarrow H[x(t)] \quad \text{if } \|\delta x(t)\| \rightarrow 0 \quad 3.87$$

#### *P.2 Phase Independence of Scaling and Homogeneity*

If the signal  $x(t)$  is replaced by  $k \cdot x(t)$ , with  $k$  a real positive constant, by using the transform linearity one can demonstrate that:

$$\frac{H[kx(t)]}{kx(t)} = \frac{H[x(t)]}{x(t)} \quad 3.88$$

$$\text{e.g. } H[kx(t)] = kH[x(t)] \quad 3.89$$

March 2014

### *P.3 Harmonic Correspondence*

By assuming constant and positive the amplitude and frequency of a single sinusoid, for each  $A$ ,  $f$  and  $\varphi$  one must has:

$$H[A \cos(\omega t + \varphi)] = A \sin(\omega t + \varphi) \quad 3.90$$

### *Bedrosian Theorem*

As already mentioned, Bedrosian E. establishes a fundamental result for the Hilbert transform of the functions product [71]. In particular, he was the first to take care of the validity of the following relationship under the Hilbert Transform:

$$H[f(t)g(t)] = f(t)H[g(t)] \quad 3.91$$

where  $f(t)$  and  $g(t)$  are generally real-valued functions of the variable  $t$  in  $L^2(\mathbb{R})$ , and  $H[.]$  the Hilbert Transform operator. This spectral condition is generally somewhat restrictive to be useful in modal identification since exponential function has no bounded spectrum. Obviously, such a condition is satisfied with a good approximation for highly damped sinusoids. Appendix A contains all the mathematical derivations to reach the powerful outcome in the Eq. (3.91).

Although less employed in power engineer literature, a more general expression of the Hilbert transform product of two complex functions,  $f(t)$  and  $g(t)$ , has been developed in [72]:

$$H[f(t)g(t)] = f(t)H[g(t)] + g(t)H[f(t)] + H[H[f(t)]H[g(t)]] \quad 3.92$$

this is essentially due to the fact that the Hilbert transform product remains.

From the convolution properties, one can simply derive that the inverse Hilbert transform of a signal  $x_H(t)$  is given by:

$$x(t) = H^{-1}[x_H(t)] = \frac{-1}{\pi t} * x(t) \quad 3.93$$

and therefore the double application of the HT returns the original signal with opposite sign. Tab. 3.1 lists the most used Hilbert transform pairs whereas those

March 2014

ones of the trigonometric and exponential functions are of interest for our purpose [73].

*TAB. 3.1 – HILBERT TRANSFORM PAIRS*

<b>Signal</b>	<b>Hilbert transform</b>
$\sin t$	$-\cos t$
$\cos t$	$\sin t$
$e^{it}$	$-ie^{it}$
$e^{-it}$	$ie^{-it}$
$\frac{1}{t^2 + 1}$	$\frac{t}{t^2 + 1}$
$\frac{\sin t}{t}$	$\frac{1 - \cos t}{t}$
<i>Rectangular function</i> $\Pi(t)$	$\frac{1}{\pi} \log \left  \frac{t + \frac{1}{2}}{t - \frac{1}{2}} \right $
<i>Dirac delta function</i> $\delta(t)$	$\frac{1}{\pi t}$
<i>Characteristic function</i> $X[a,b](t)$	$\frac{1}{\pi} \log \left  \frac{t - a}{t - b} \right $

As can be noted, Hilbert transform of a cosine function is a sine function and similarly, the Hilbert transform of a sine function is a negative cosine function, as direct result of the Eq. (3.93).

### 3.7.3 Hilbert Huang transform limitations

Power system oscillatory behaviour is described through non-stationary and possibly non linear signals characterized by frequency components in the interval 0-2 Hz that can lie furthermore within the same *octave*. An octave is basically the frequency range between one frequency and its double or half frequency. With respect to these, unfortunately HHT presents some limitations, due both to the EMD behaviour and to the discrete implementation of the HT, that could lead to a wrongful understanding of the electrical power systems dynamic. First of all, the sifting algorithm does not guarantee that each IMF has mono-component character especially if (i) the highest two frequencies in the original signal fall in an octave, (ii) the original signal consists of a weak high-frequency component along with a dominating lower frequency component. This implies that first IMF is not a mono-frequency signal, but instead it exhibits a modes mixing, making little sense to expect useful physical interpretation through the application of the Hilbert analysis. The error on the first IMF is transmitted to the next IMF. Secondly, this decomposition process could generate spurious information not related to the actual signal modal content often due to the end effects associated with the decomposition. Thirdly, leakage errors caused by the transformation from the time domain to the frequency domain and vice versa, in HT numerical computation, could play a not-negligible role in the success of the entire procedure. Indeed, the first two issues are major concerns with respect to the last one. Actually, the HHT refinements presented in the following are all developed for addressing exactly the described critical.

To show the mode mixing issue in the EMD let consider the following signals:

$$x_1 = 1.8\sin(1.5\pi t) + \sin(0.5\pi t) \quad 3.94$$

$$x_2 = 1.8\sin(1.5\pi t) + \sin(\pi t) \quad 3.95$$

As can be noted the signals differ from the fact that the second one in (3.95) has two frequency component in the same octave with respect to the first one in (3.94). By applying the EMD and analyzing the Fourier spectrum of the first IMF in both the cases one can appreciate the issue outlined above, that is the first IMF for the second signal is not mono-component.

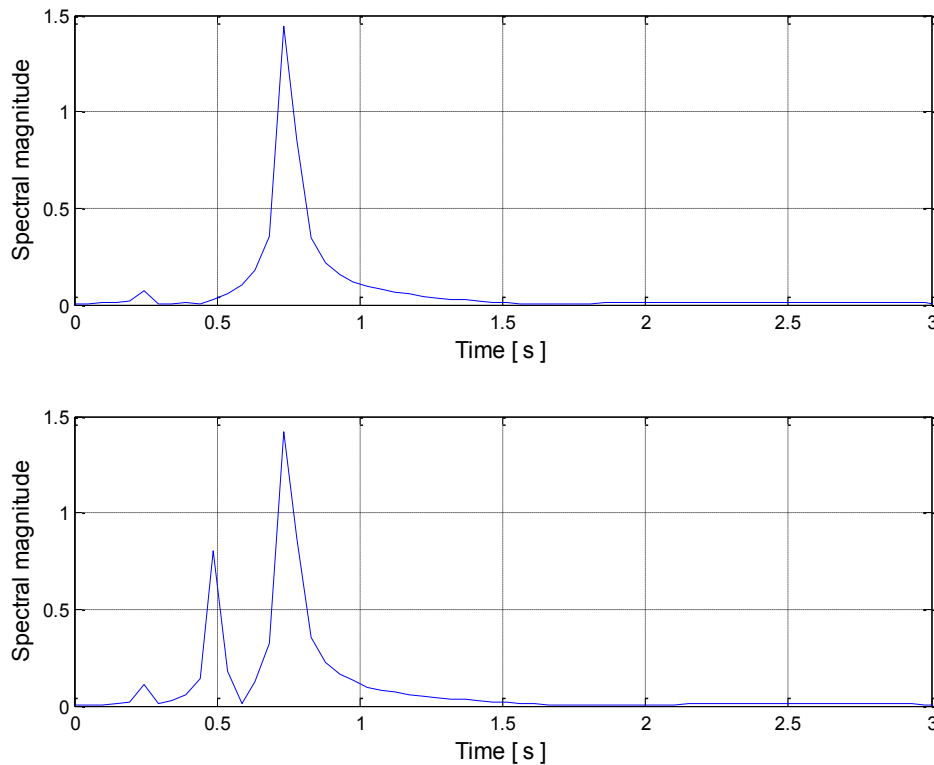


Fig. 3.2 – Fourier spectra of the signals in (3.94) and (3.95)

### 3.7.4 HHT refinements

Several HHT refinements, here reported, have been proposed for solving the modes mixing issue in the IMF furnished by the EMD. Apart from the Frequency Heterodyne Technique (FHT), which is here reported only for sake of completeness since somewhat hard to employ in practice, the main philosophy behind the others is to alter the modal content of the investigated signal with a *masking signal*. The masking signals achievement procedure and their direct employment criterion vary among the different proposals of refinement. The first one considered, exactly *HHT with standard masking technique* (M-EMD), although effective for power quality applications is demonstrated to be ineffective in the case of closely spaced frequency components. *Fourier-Based Masking Technique* (R-EMD), *EMD with Energy-Based Masking Technique* (A-EMD) and *Targeted approach to apply masking signal-based empirical mode decomposition* (T-EMD) have been specifically developed for extending the masking technique to electromechanical oscillations applications.

### 3.7.4.1 HHT with standard masking technique

To enhance EMD resolution in HHT the use of masking signals has been firstly proposed in [66]. The rationale behind the refinement is to alter the original signal with the addition and the subtraction of a mask-signal to get two new signals. Classical EMD is performed on these two new signals to obtain the first IMF only, hence the average of the two IMF is then computed to yield the correct IMF of the original signal. Obviously, the masking signal must be properly constructed: to be effective its frequency must be chosen higher than the highest frequency component present in the original signal and that falls in its same octave. A systematic procedure to implement mask-EMD (M-EMD) can be so codified:

- 1) Perform FFT to estimate the stationary equivalents of the possibly time-varying frequency components  $f_1, f_2, \dots, f_n$  with  $f_1 < f_2 < \dots < f_n$ ;
- 2) Construct  $n-1$  masking signals of the type  $\text{mask}_k = M_k \sin(2\pi(f_{k-1} + f_k)t)$  for  $k = 2, 3, \dots, n$ .  $M_k$  is empirically suggested to be 5.5 times the magnitude of  $f_k$ , however case by case investigations have to be preferred.
- 3) Calculate two new signals  $x(t) + \text{mask}_n$  and  $x(t) - \text{mask}_n$  and apply on each of them the steps of the standard EMD described in the subsection 3.7.1 to get only the first IMF from each of them,  $c_i^+(t) = \text{IMF}^+$  and  $c_i^-(t) = \text{IMF}^-$ . The correct IMF will be  $c_1(t) = \text{IMF} = 0.5(\text{IMF}^+ + \text{IMF}^-)$ .
- 4) Obtain the residue  $r_1(t) = x(t) - c_1(t)$ ;
- 5) Perform steps 3 and 4, replacing  $x(t)$  with the residue obtained in step 4, iteratively until  $n-1$  IMF containing frequency components  $f_2, f_3, \dots, f_n$  have been extracted. The final residue  $r_n(t)$  will contain the remaining component  $f_1$ .

Now, by applying the present refinement to the signal in (3.95) one can demonstrate the validity of the masking philosophy. In this case the unique masking signal to construct is depicted in Fig. 3.3. Superimposing the latter to the original signal and performing the steps above, the Fourier spectrum of the first IMF becomes the one illustrated in Fig. 3.4.

March 2014

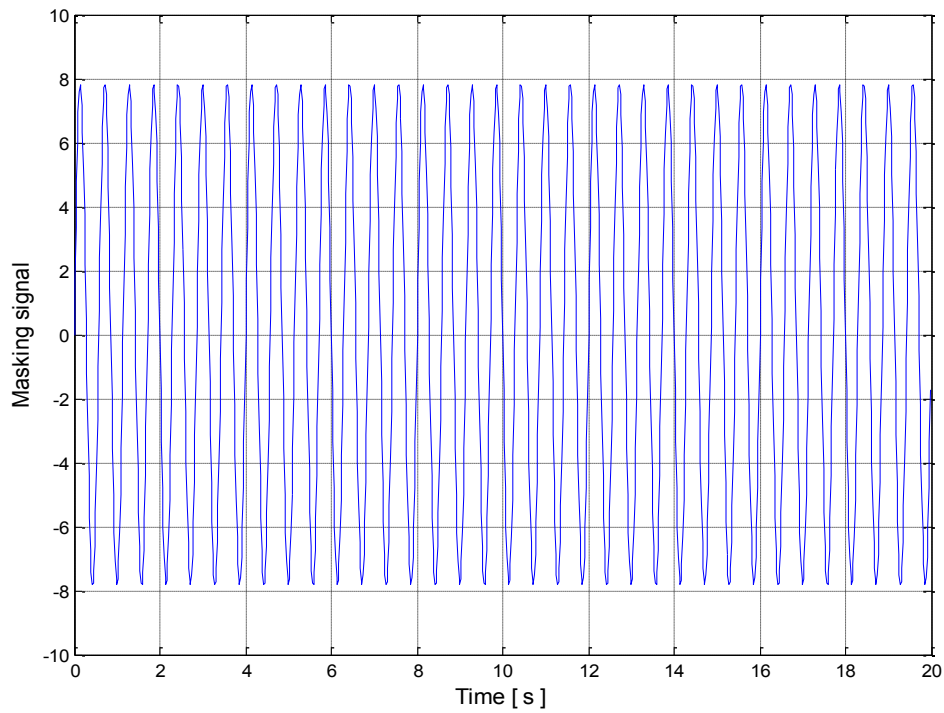


Fig. 3.3 – Masking signal

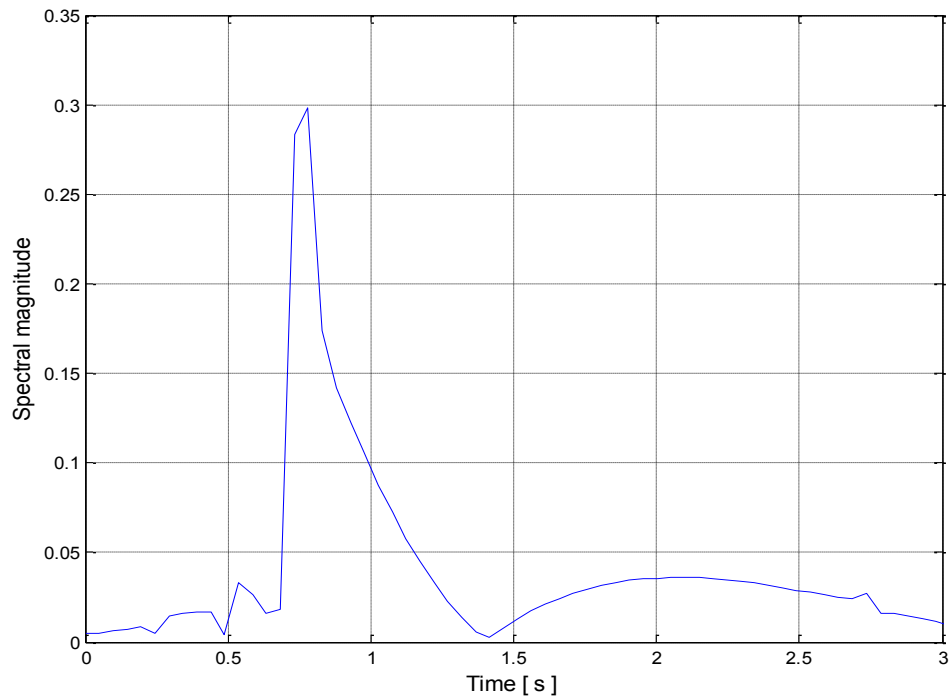


Fig. 3.4 – Fourier spectrum of the first IMF from the M-EMD of the signal in (3.95)

### 3.7.4.2 Frequency Heterodyne Technique

This technique is well-known in the telecommunication scientific community as *heterodyne detection* [75]. Practically, Frequency Heterodyne Technique (FHT) alters the spectral distance between two adjacent frequency components through an injection of a pure tone of frequency greater than the highest frequency present in the original distorted signal. The objective, as usual, is to overcome the modes mixing issue in the elemental components from the decomposition procedure. Obviously, the aforementioned expedient implies to know in advance the spectral content of the original signal. The major benefit ensured by FHT is to reduce loss of amplitude information while extracting the highest frequency component.

The basic idea in FHT is to shift the frequency content of an original distorted signal  $x(t)$  around a new carrier frequency  $f_c$ , multiplying it by the analytic representation of the carrier signal. The signal thus obtained  $x_{\text{DSB}}(t)$  is referred to as *double sideband modulated* (DSB) with suppressed carrier as it contains two frequency shifted copies of the original signal on either side of the carrier frequency:

$$x_{\text{DSB}}(t) = x(t)e^{i2\pi f_c t} \quad 3.96$$

A *single sideband modulated* (SSB) signal can be obtained by removing one of the sidebands using an appropriate filter or a Hilbert transformer. In the latter case, the lower sideband signal  $x_{\text{SSB}}(t)$  can be readily derived by employing the analytic form of  $x(t)$  in the manner that follows:

$$x_{\text{SSB}}(t) = \text{Re}\left\{ [x(t) + ix_H(t)]e^{-i2\pi f_c t} \right\} \quad 3.97$$

From an operational point of view, let suppose that the original signal contains two frequencies  $f_1$  and  $f_2$  falling in the same octave (with  $f_1 < f_2$ ), the heterodyne frequency  $f_c$  is chosen in the range  $f_2 < f_c < 2f_2 - f_1$ . The SSB frequencies obtained by applying the aforementioned heterodyning are  $f_c - f_1$  and  $f_c - f_2$ , positioned in different octaves if  $f_c$  is properly selected. Hence, the subsequent application of the standard EMD furnishes IMF of frequencies  $f_c - f_1$  and  $f_c - f_2$  that can be heterodyned back to their original frequencies. They should realistically be

mono-component and slightly reduced in amplitude.

An analysis on the error distribution in the EMD with masking and frequency heterodyning points out that while in the first case the error is distributed along the observation window, in the second one it is concentrated at the window's edges and near switching instants only. Indeed, selecting an adequate heterodyne frequency is a complex task which would require the detailed knowledge of the spectral content of the distorted signal. Unfortunately, this can be achieved only by performing a FFT-spectral analysis, that as already mentioned, could be approximated and possibly inaccurate.

Let now imagine to adopt this refinement instead than M-EMD for solving the mode mixing issue in the IMF for the signal in (3.95). A proper choice of the heterodyne frequency is  $f_c = 0.85$  Hz. The lower sideband signal  $x_{SSB}(t)$  is plotted in the Fig. 3.5 that follows:

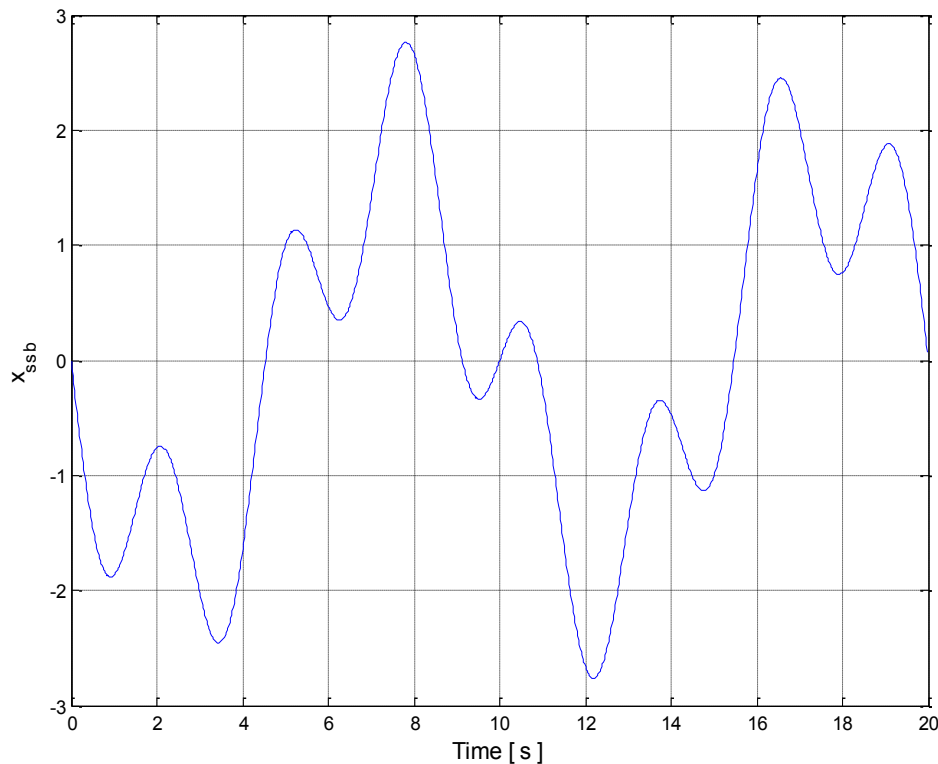


Fig. 3.5 – Lower sideband signal related to the one in (3.95)

The SSB frequencies are now in different octaves, as demonstrated in Fig. 3.6 so permitting to the EMD to correctly extract IMF of frequencies about  $f_c - f_1 = 0.10$  Hz and  $f_c - f_2 = 0.35$  that can be heterodyned back to their original frequencies exactly  $f_1 = 0.75$  Hz and  $f_2 = 0.50$  Hz.

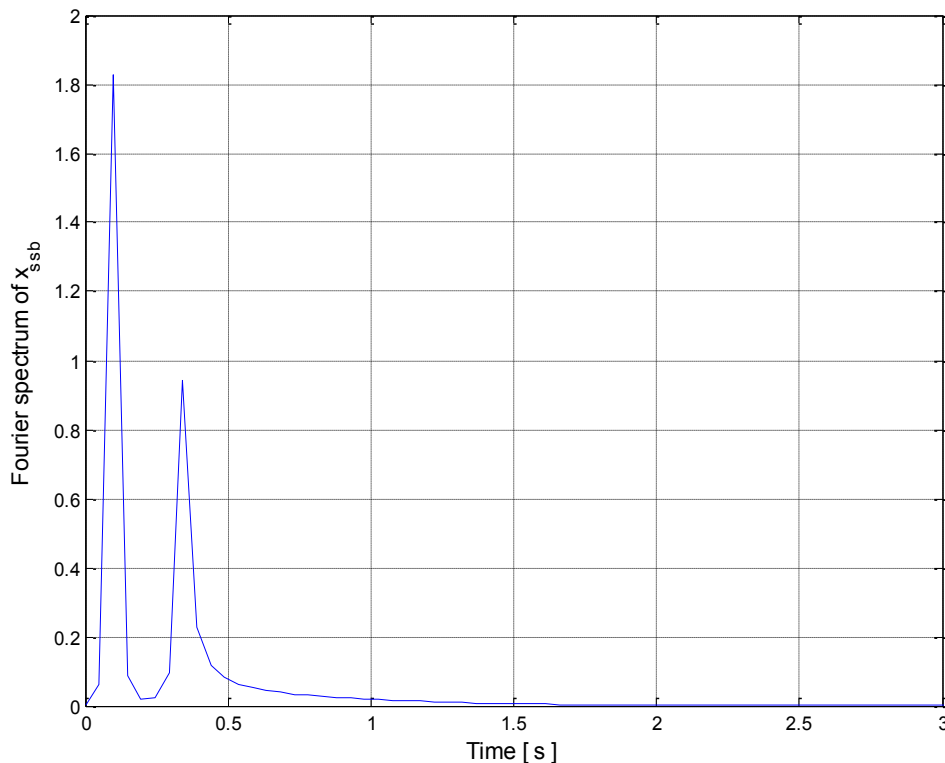


Fig. 3.6 – Fourier spectrum of the lower sideband signal related to the one in (3.95)

### 3.7.4.3 HHT with improved masking technique

Laila et al. in reference [76] developed two improved masking technique versions for EMD. Each of them, jointly employed with a local Hilbert transformer, seems to offer a better frequency and temporal resolution compared to the previous ones described so far. Without any doubt, the signals set with respect to the present HHT refinement correctly work is enlarged, nonetheless it can not be stated that these refinements solve completely the resolution issue in the EMD. This will be clearly pointed out in the Chapter 5 containing a collection of experimental findings. However, two improved masking technique algorithms, namely EMD with Fourier-Based Masking Technique, R-EMD, and EMD with Energy-Based Masking Technique, A-EMD, are here presented.

*Algorithm 1: R-EMD.*

EMD with Fourier-Based Masking Technique consists of the following steps:

1. Perform FFT to estimate the stationary equivalents of the possibly time-varying frequency components  $f_1, f_2, \dots, f_n$  with  $f_1 > f_2 > \dots > f_n$ ;
2. Construct  $n-1$  masking signals of the type  $\text{mask}_k = M_k \sin(2\pi(f_k + f_{k+1})t)$  for  $k = 1, 2, \dots, n-1$ .  $M_k$  is empirically suggested to be 5.5 times the magnitude of  $f_k$ , however case by case investigations have to be preferred.
3. Depending on the numerical values assumed by the two highest frequencies  $f_1$  and  $f_2$  and by the related magnitudes  $M_1$  and  $M_2$  distinguish two different cases:

If any of these conditions is valid:

- a)  $f_1 \leq 1$  and  $M_1 < R_{21}M_2$
  - b)  $f_1 > 1$  and  $f_1 < R_1f_2$
  - c)  $f_1 > 1$  and  $R_1f_2 < f_1 < R_2f_2$  and  $M_1 < R_{22}M_2$
  - d)  $f_1 > 1$  and  $f_1 \geq R_2f_2$  and  $M_1 < R_{23}M_2$
- with  $R_{21} = 1.1, R_1 = 1.5, R_2 = R_{22} = 2, R_{23} = 0.5$

then consider the Case a) otherwise the Case b)

Case a)

3.a Employ only the first masking signal for the entire decomposition process

$$\text{mask}_1(t) = M_1 \sin(2\pi(f_1 + f_2)t)$$

4.a Construct two new signals  $x(t) + \text{mask}_1(t)$  and  $x(t) - \text{mask}_1(t)$ , then apply on each of them the standard EMD to get all the IMF,  $c_i^+(t) = \text{IMF}_i^+$  and  $c_i^-(t) = \text{IMF}_i^-$  for  $i=1, 2, \dots, n$  and

Case b)

3.b Employ all the constructed masking signals.

4.b Construct two new signals  $x(t) + \text{mask}_1(t)$  and  $x(t) - \text{mask}_1(t)$ , then apply on each of them the standard EMD selecting only the first IMF from each one,  $c_1^+(t)$  and  $c_1^-(t)$ . Thus, the first IMF of  $x(t)$  is

$$c_1(t) = \frac{c_1^+(t) + c_1^-(t)}{2}$$

March 2014

also the residue  $r_n^+(t)$  and  $r_n^-(t)$ . Hence:

$$c_i(t) = \frac{c_i^+(t) + c_i^-(t)}{2}$$

$$r_n(t) = \frac{r_n^+(t) + r_n^-(t)}{2}$$

5.b Get the residue,  $r_1(t) = x(t) - c_1(t)$

6.b Use the next masking signal by performing iteratively the steps 4.b and 5.b while replacing  $x(t)$  with the residue obtained at each iteration, until  $n-1$ .

7.b) Calculate the last residue  $r_n(t) = x(t) - c_n(t)$

8.b If the residue is above the threshold value of error tolerance, then repeat on it the step 2 of the sifting algorithm in Section 3.7.1 for getting the next IMF and the new residue.

The reconstructed signal will be:

$$\hat{x}(t) \cong \sum_{i=1}^n c_i(t) + r_n(t)$$

As can be argued, this algorithm extends the HHT refinement with standard masking technique (Case b)), specifically developed for power quality applications and hence for “high frequency signals”, by adding an alternative procedure (Case a)) in the case of “low-frequency signals”. In this manner the entire algorithm can handle the decomposition for a large set of signals both with high-and low-frequency components. As far as the numerical values of the parameters  $R_1$ ,  $R_2$ ,  $R_{21}$ ,  $R_{22}$ , and  $R_{23}$ , they are experimentally derived for matching the inter-area oscillations characteristics. The need for a tuning is not to exclude. This further increases the empirical connotation of the present HHT refinement.

The application of this improvement to the signal in (3.95) makes more selective the first IMF extraction with respect to the M-EMD. This is illustrated in Fig. 3.7 which depicts the Fourier spectrum of the IMF approximating the signal component at frequency  $f_1 = 0.75$  Hz.

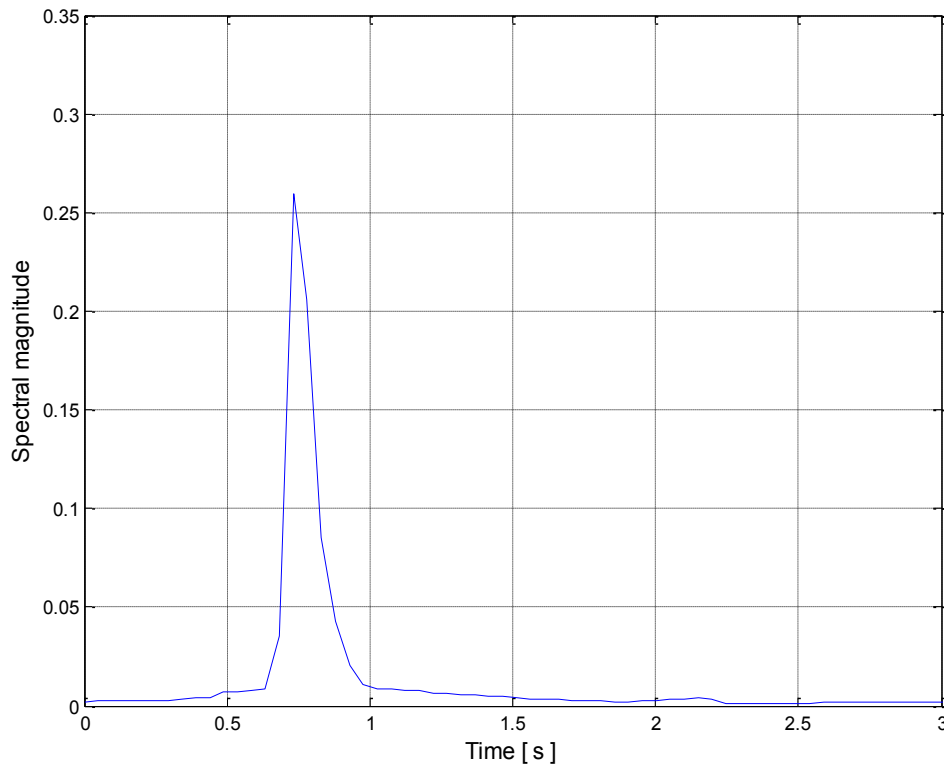


Fig. 3.7 – Fourier spectrum of the first IMF from R-EMD of the signal in (3.95)

Sometimes the ordinary M-EMD could fail in extracting mono-components, R-EMD can represent in that cases an option to investigate to solve the problem. At the best of our investigation anyway, its success is not globally guaranteed hence we recommend a critical employment for real time applications.

Algorithm 2: *A-EMD*.

The chief criticism of the R-EMD algorithm is due to the increase of the total number of empirical assumptions for the heuristic choice of the mask parameters, frequency and amplitude, besides based upon the preliminary employment of the FFT which assumes to be stationary the signal in the time-window analyzed. This philosophy could hence lead to a wrong understanding of the power systems behaviour caused by a lack of resolution. For this reason, the same authors who developed the R-EMD algorithm have proposed an alternative one based upon the delineated Case a) and the notion of energy weighted mean of the highest frequency. It is termed EMD with Energy-Based

March 2014

Masking Technique, briefly A-EMD; its fundamental steps are listed in the sequel:

- 1) Execute the standard EMD on the original distorted signal  $x(t)$ .
- 2) Use only the first IMF,  $c_1(t)$ , which is expected to contain the highest frequency component of the signal,  $f_{max}$ , but could also contain mode mixing. Determine the signal instantaneous frequency  $f_1(t)$  and the instantaneous magnitude  $A_1(t)$  by implementing the HT.
- 3) Calculate the energy weighted mean of  $f_1(t)$  with the available samples number  $L$ :

$$\bar{f} = \frac{\sum_{k=1}^L A_1(k) f_1^2(k)}{\sum_{k=1}^L A_1(k) f_1(k)}$$

- 4) Observe Case a) from R-EMD, then replace step 3.a with the following one, completing all the steps:

$$\text{mask}_1(t) = M_1 \sin(2\pi(m\bar{f})t)$$

where  $M_1 = \max_{i=1,\dots,L} \{A_1(k)\}$  and  $m > 1$ . Generally, if the maximum frequency component in the analyzed signal is lower than 1 Hz, it is usual set  $m=2$  as upper bound for ensuring an effective masking, so avoiding that the product  $m\bar{f}$  would be much higher than  $f_{max}$ .

Like in the previous algorithm, the authors generalizes the results of other colleagues, specifically Deering and Kaiser in [74], who suggested the following masking signal form:

$$\text{mask}_1(t) = a_0 \sin\left(\frac{2\pi\bar{f}t}{f_s}\right)$$

As can be noted the sampling frequency  $f_s$  is replaced by the parameter  $m$ , whereas furthermore an analytic criterion for the  $a_0$  choice is also introduced. The application of A-EMD on the signal in (3.95) produces similar results to the

R-EMD, although the choice of the parameter  $m$  in the masking construction is not a trivial task.

#### **3.7.4.4 Targeted approach to apply masking signal-based empirical mode decomposition**

A further HHT refinement aimed at addressing the mode mixing issue associated with closely spaced modes frequency modes in power system signals while applying EMD is due to Prince et al in [77]. The algorithm's steps are listed later since before applying them a pre-processing stage consisting in a detrending through a raw application of the EMD, is performed. The basic idea of the T-EMD is to target some modes to track through the FFT spectrum of the processed signal, to aggregate individually IMF in which the targeted modes are identified, to obtain in this way a concentrated signal on which apply the M-EMD. T-EMD steps are hence here summarized:

1. FFT spectral analysis is firstly performed and the modes to be extracted for a particular application are then identified; these modes will be denoted hereafter as *targeted modes*.
2. If the magnitude of the targeted frequency  $f_k$  is comparable in magnitude with the nearby frequencies in the analyzed signal (let's say at least half the strength of the dominant frequency), then go directly to step 4.
3. Perform the standard EMD identifying the IMF in which the targeted mode,  $f_k$ , is dominant via FFT or HT. Aggregate the identified IMF to get a concentrated signal. Replace the original signal with the concentrated one and go to step 2.
4. Form an appropriate masking signal and carry out M-EMD.
5. M-EMD provides in output the targeted frequency component  $f_k$ , verifying successively that it has a complete mono-component trait. FFT or Hilbert spectrum can be used for the purpose. Algorithm accuracy can be enhanced through a further concentrating of the processed signal using step 3 repeatedly.

A crucial aspect of this HHT refinement is the adequate choice of the observation window which is inherently depending on the need to ensure both the correct identification of the electromechanical oscillation frequencies and a

March 2014

proper numbers of extrema points corresponding to the targeted modes in the sifting process. The authors suggest a minimum of two or three cycles for obtaining good frequency resolution from FFT analysis without giving information about the effect of the time window on the sifting process. At any rate, as in all the HHT refinements using FFT for estimating the electromechanical oscillation frequencies, wrongful interpreting of the power systems dynamic could be achieved as previously discussed. Evidently, this threatens the consistency of the algorithm in the presence of strongly nonlinear and non-stationary signals. With this Section the present Chapter, devoting to analyze the relevant literature addressing the electromechanical oscillations parameter estimation, ends. The next one, will present the basic thesis contributes to the literature, not forgetting anyway that the HSVD-VARPRO previously described, has been tailored by me and my supervisor Professor Lauria D.

## Chapter 4

# *Advances in the use of Hilbert Transform*

The estimation algorithms here presented represent, without any doubt, the chief thesis contribute. The first one, as the previous described in the Chapter 3, faces the issue to detect and estimate electromechanical oscillations in power systems. It has been tailored for answering in a more simple and pragmatic manner to the main weaknesses of the HHT and the related refinements so far presented. This algorithm combines a recent signal decomposition theorem HT-based for separating an assigned signal into elemental ones, each of them characterized by a single frequency component with a robust preliminary nonlinear spectral analyzer. The second one is an improved non linear least squares method for estimating the damping levels of electromechanical oscillations. A semi-analytic procedure is tailored with the aim to get an expression of the Cauchy principal value integral to suitably include in the objective function of the least squares minimization. The algorithm, conversely to the first one, will be directly tested in this Chapter, to demonstrate its accuracy in damping estimation as well as its resiliency against a critical effect of the wide area communication networks, namely dropout packets. This is partially due to the inherent regularization action of the Hilbert transform in correspondence of the data lack.

## 4.1 An advanced methodology Hilbert Transform based for estimating the power systems modal content

The estimation algorithm here presented has been specifically designed for answering in a more simple and pragmatic manner to the main weaknesses of the HHT and the related refinements so far presented [78]. This algorithm combines a recent signal decomposition theorem HT-based for separating an assigned signal into elemental ones, each of them characterized by a single frequency component with a robust preliminary nonlinear spectral analyzer, named  $L_p$  *periodogram*. This procedure results very appropriate for analyzing some critical cases of electromechanical oscillations, due to the  $L_p$  periodogram robustness against heavy-tailed noise and its intrinsic ability in estimating also closely spaced frequency components. The proposed approach bases its own foundations on very simple rudiments of the signal processing theory, showing also some appealing features worth of mention such as the inherent simplicity, the reliability and consistency of the performance and at last very low computational burden. The core of the mentioned theorem is the exact division of a general signal into two time functions whose spectra are non-vanishing over two mutually exclusive frequency ranges separated by a bisecting frequency. This theorem ensures, through several steps of bisecting, the separation of the original signal, having also multiple closely spaced frequency components, into elemental signals, each dominated by a single frequency component. As it will be experimentally demonstrated in Chapter 5, the following signal decomposition theorem, proposed in [79] for identification of mechanical systems and structural dynamics, represents a viable alternative to the standard EMD and related improvements, for separating electromechanical oscillations close in frequency in non-linear and non-stationary power signals. In this manner the empirical connotation of EMD, specifically of the sifting algorithm, is hence outdated through a more rigorous analytical approach.

### 4.1.1 A signal decomposition theorem Hilbert transform based

Let  $x(t)$  be a generic real signal of the real variable  $t$  characterized by  $m$  significant frequency components  $f_1, f_2, \dots, f_m$  in  $L^2(-\infty, +\infty)$ . It can be decomposed in  $m$  elemental signals  $x_i^{(d)}(t)$  whose Fourier spectra are equal to  $\hat{F}(\omega)$  over  $m$

March 2014

mutually exclusive angular frequency  $|\omega| < \omega_{b1}$  and  $\omega_{b1} < |\omega| < \omega_{b2}$  and  $\omega_{b(m-1)} < |\omega|$ :

$$x(t) = \sum_{i=1}^m x_i^d(t) \quad 4.1$$

where  $\hat{F}(\omega)$  is the Fourier transform of  $x(t)$  and in particular  $\omega_{bi} \in [\omega_i, \omega_{i+1}]$ , for  $i = 1, 2, \dots, m-1$  are the bisecting frequencies. In this manner each signal having a narrow bandwidth can be determined by the following relations:

$$x_i^d(t) = s_i(t) - s_{i-1}(t), \dots, x_m^d(t) = x(t) - s_{m-1}(t) \quad 4.2$$

$$s_i(t) = \sin(\omega_{bi}t)H[x(t)\cos(\omega_{bi}t)] - \cos(\omega_{bi}t)H[x(t)\sin(\omega_{bi}t)] \quad \text{for } i = 1, 2, \dots, m-1 \quad 4.3$$

where  $s_0(t)=0$  and  $H[.]$  represents the Hilbert transform operator of the function in the square brackets. Since the theorem represents the core of the proposed algorithm for the electromechanical oscillations detection and estimation, I believe that it is appropriate to immediately demonstrate the powerful result in the Eq. (4.2).

### 4.1.2 Decomposition theorem proof

A certain time series  $x(t)$  can be expressed through the summation of two signals,  $s_1(t)$  and  $\bar{s}_1(t)$ , whose Fourier transforms,  $\hat{s}_1(t)$  and  $\hat{\bar{s}}_1(t)$ , respectively vanish for  $|\omega| > \omega_b$  and  $|\omega| < \omega_b$ :

$$\hat{s}_1(t) = \begin{cases} 0, & |\omega| > \omega_b \\ \hat{F}(\omega), & |\omega| < \omega_b \\ \frac{\hat{F}(\omega)}{2}, & |\omega| = \omega_b \end{cases} \quad 4.4$$

March 2014

$$\hat{\bar{s}}_1(t) = \begin{cases} \hat{F}(\omega), & |\omega| > \omega_b \\ 0, & |\omega| < \omega_b \\ \frac{\hat{F}(\omega)}{2}, & |\omega| = \omega_b \end{cases} \quad 4.5$$

As it can be noted, both the Fourier transforms are the same and equal to  $\frac{\hat{F}(\omega)}{2}$  at the boundary  $|\omega| = \omega_b$  of the two mutually exclusive frequency ranges, with  $\omega_b$  an arbitrary positive value referred to as the *bisecting frequency*. This remarkable property is very useful since together with the Parseval's theorem in Fourier transform permits to establish that  $s_1(t)$  and  $\bar{s}_1(t)$  are real functions in  $L^2(-\infty, +\infty)$ :

$$\int_{-\infty}^{+\infty} |s_1(t)|^2 dt = \int_{-\infty}^{+\infty} |\hat{s}_1(\omega)|^2 d\omega \leq \int_{-\infty}^{+\infty} |\hat{F}(\omega)|^2 d\omega / 2\pi = \int_{-\infty}^{+\infty} |x(t)|^2 dt < \infty \quad 4.6$$

$$\int_{-\infty}^{+\infty} |\bar{s}_1(t)|^2 dt = \int_{-\infty}^{+\infty} |\hat{\bar{s}}_1(\omega)|^2 d\omega \leq \int_{-\infty}^{+\infty} |\hat{F}(\omega)|^2 d\omega / 2\pi = \int_{-\infty}^{+\infty} |x(t)|^2 dt < \infty \quad 4.7$$

In order to demonstrate the validity of the signal decomposition theorem in the Eq. (4.2), let consider the functions  $s_a(t) = \cos(\omega_b t)$  and  $s_b(t) = \sin(\omega_b t)$ , whose Fourier transform are non-vanishing over the same mutually exclusive frequency ranges with  $s_1(t)$  and  $\bar{s}_1(t)$  (consider in fact that they vanish at all the frequencies except for  $|\omega| = \omega_b$ ). The HT of the products  $s_a(t)x(t)$  and  $s_b(t)x(t)$  becomes:

$$H[s_a(t)x(t)] = H[s_a(t)s_1(t)] + H[s_a(t)\bar{s}_1(t)] \quad 4.8$$

$$H[s_b(t)x(t)] = H[s_b(t)s_1(t)] + H[s_b(t)\bar{s}_1(t)] \quad 4.9$$

The above relations can be handled by using the *Bedrosian identity* in Hilbert transform which establishes that the Hilbert transform of the product of a low-pass,  $f_{LP}(t)$ , and a high-pass(t) signal,  $f_{HP}(t)$ , with non-overlapping spectra is

March 2014

given by the product of the low-pass signal and the Hilbert transform of the high-pass signal (see the Appendix A for detail):

$$H[f_{LP}(t)f_{HP}(t)] = f_{LP}(t)H[f_{HP}(t)] \quad 4.10$$

Hence:

$$H[s_a(t)x(t)] = s_1(t)H[s_a(t)] + s_a(t)H[\bar{s}_1(t)] \quad 4.11$$

$$H[s_b(t)x(t)] = s_1(t)H[s_b(t)] + s_b(t)H[\bar{s}_1(t)] \quad 4.12$$

Eqs (4.11) and (4.12) represent an equations system in two unknowns, respectively  $s_1(t)$  and  $H[\bar{s}_1(t)]$  computable from the relations that follow:

$$s_1(t) = \frac{s_b(t)H[s_a(t)x(t)] - s_a(t)H[s_b(t)x(t)]}{s_b(t)H[s_a(t)] - s_a(t)H[s_b(t)]} \quad 4.13$$

$$H[\bar{s}_1(t)] = \frac{H[s_a(t)]H[s_b(t)x(t)] - H[s_b(t)]H[s_a(t)x(t)]}{s_b(t)H[s_a(t)] - s_a(t)H[s_b(t)]} \quad 4.14$$

Since  $H[s_a(t)] = \sin(\omega_b t)$  and  $H[s_b(t)] = -\cos(\omega_b t)$  and  $s_b(t)H[s_a(t)] - s_a(t)H[s_b(t)] = 1$  the previous Eqs can be rewritten as:

$$s_1(t) = \sin(\omega_b t)H[x(t)\cos(\omega_b t)] - \cos(\omega_b t)H[x(t)\sin(\omega_b t)] \quad 4.15$$

$$H[\bar{s}_1(t)] = \sin(\omega_b t)H[x(t)\sin(\omega_b t)] + \cos(\omega_b t)H[x(t)\cos(\omega_b t)] \quad 4.16$$

while the  $\bar{s}_1(t)$  component and the HT of the  $s_1(t)$  can be directly derived from the relationship  $x(t) = s_1(t) + \bar{s}_1(t)$ , that is:

March 2014

$$\bar{s}_1(t) = x(t) - s_1(t) \quad 4.17$$

$$H[s_1(t)] = H[x(t)] - H[\bar{s}_1(t)] \quad 4.18$$

Basically, Eq. (4.13) is the straightforward application of the Eq. (4.3) with bisecting frequencies  $\omega_{bi}$  with  $i = 1, 2, \dots, m-1$ . By generalizing, the decomposition procedure in two signal components can be applied in two different manner for the  $m-1$  bisecting frequencies identified  $\omega_{b1}, \omega_{b2}, \dots, \omega_{b(m-1)}$  through a repetition of the bisecting process.

The first manner can be defined as *original signal decomposition procedure* with respect to the second one that will indicate as *modified signal decomposition procedure*.

The original version faces with the signal decomposition according to the following relations:

$$x(t) = s_1(t) + \bar{s}_1(t) = s_2(t) + \bar{s}_2(t) = \dots = s_{m-1}(t) + \bar{s}_{m-1}(t) \quad 4.19$$

$$x_1^{(d)}(t) = s_1(t); \quad x_i^d(t) = s_i(t) - s_{i-1}(t) \quad \text{for } i = 2, 3, \dots, m-1 \quad 4.20$$

in which  $s_i(t)$  and  $\bar{s}_{m-1}(t)$  have to be determined by the Eqs (4.15) and (4.17), selecting respectively the proper bisecting frequency value  $\omega_{bi}$  and  $\omega_{b(m-1)}$ .

Conversely, the modified version performs a bisection of the previously decomposed signals in sequence:

$$x(t) = s_1(t) + \bar{s}_1(t); \quad \bar{s}_1(t) = s_2(t) + \bar{s}_2(t); \quad \bar{s}_{m-2}(t) = s_{m-1}(t) + \bar{s}_{m-1}(t) \quad 4.21$$

with the elemental signals of the Eq. (4.2):

$$x_1^d(t) = s_1(t) \quad \text{for } i = 1, 2, 3, \dots, m-1; \quad x_m^d(t) = \bar{s}_{m-1}(t) \quad 4.22$$

Since the modified signal decomposition procedure can be less accurate than the original signal decomposition procedure, due to potentially accumulated

numerical errors in HT, the original one is adopted in the thesis for the electromechanical modes identification.

### 4.1.3 A robust non linear spectral analyzer

The actual applicability of the theorem in power system modes identification could be threatened by the inability to identify the actual frequency components of the acquired signals by looking at the Fourier spectrum. For this reasons a non linear spectral analyzer is employed for determining the bisecting frequencies, the  $L_p$  periodogram, which can be interpreted as a direct extension of the Laplace periodogram,  $p=1$ , and of the ordinary periodogram,  $p=2$ :

$$P(\omega) = \frac{1}{n} \left| \sum_{t=1}^n x(t) e^{-it\omega} \right|^p \quad p \in \{1,2\} \quad 4.23$$

where  $n$  is the number of the samples of  $x(t)$ . The paper [80] shows how to design a harmonic regressor by employing  $p \in [1,2]$  in order to make the periodogram robust and efficient enough. In particular, by denoting with  $\|\cdot\|$  the Euclidean norm, it is demonstrated that the following periodogram definition is well posed:

$$P(\omega) = \frac{n}{4} \|\beta_n(\omega)\|^2 \quad 4.24$$

with

$$\beta_n(\omega) = \arg \min_{\beta \in \mathbb{R}^2} \sum_{t=1}^n |x(t) - c_t^T(\omega)\beta|^p \quad 4.25$$

$\beta_n(\omega)$  is the least square regression coefficient corresponding to the trigonometric regressor  $c_t(\omega) = [\cos(\omega t), \sin(\omega t)]^T$ .

Several signals, of different kind (synthetic, acquired by IEEE test networks, real PMU data), were considered in order to establish if the  $p$ -value choice would be

affected by signal typology. At the best of our simulations, we can confirm, as stated by Ta-Hsin Li, that the optimal  $p$ -value falls within the interval [1,2]; it is not possible to derive further practical considerations about the  $p$ -value choice with respect to the type of data analyzed. The  $p$ -value of 1.5 can be reasonably conceived as a trade-off between the robustness of the Laplace periodogram ( $p=1$ ) against extreme heavy-tailed noise and the efficiency of the ordinary periodogram ( $p=2$ ). Besides, the value of 1.5 resulted the mean value of the optimal  $p$ -values over all the performed simulations.

From an operational point of view, the identification of the bisecting frequencies  $\omega_{bi} \in [\omega_i, \omega_{i+1}]$ , for  $i=1,2,\dots,m-1$  can be performed by determining the  $m$  peaks of the signal  $L_p$  periodogram (with  $1 < p < 2$ ). Each elemental signal obtained by the Eq. (4.2) has the feature of being mono-frequency. By making use of the HT fundamentals reported in the Section 3.7.2, instantaneous amplitude and phase angle values of the  $i^{\text{th}}$  component  $x_i^d(t)$  can be determined. The analytical signal notation for the  $i^{\text{th}}$  component is:

$$A_{mi}(t)e^{i\vartheta_{mi}(t)} = x_i^d(t) + iH[x_i^d(t)] \quad 4.26$$

Once derived the instantaneous frequency  $f_i$  in Eq. (4.27) and the damping factor  $\sigma_i$  in Eq. (4.28), by employing the linear least square procedure described in [81], their mean values can be respectively estimated from the slope of the phase angle  $\theta_{mi}(t)$  versus time plot and from the slope of the decaying amplitude  $\ln(A_{mi}(t))$  versus time plot:

$$f_i = \frac{1}{2\pi} \frac{d\vartheta_{mi}(t)}{dt}; \quad 4.27$$

$$\sigma_i = -\frac{d[\ln(A_{mi}(t))]}{dt} \quad 4.28$$

Hence, roughly speaking, the average frequency for the  $i^{\text{th}}$  component can be obtained as the slope of the straight line from the least-square fitting of the phase angle  $\theta_{mi}(t)$  versus the time, whereas the average damping coefficient for the  $i^{\text{th}}$  component can be obtained as slope of the straight line from the least-square fitting of the decaying amplitude  $\ln(A_{mi}(t))$  versus time plot. These straight lines are referred to as the average straight lines for phase angle and decaying amplitude.

## 4.2 Numerical implementation of the Hilbert transform

The theory presented in Section 3.7.2 refers to the HT computation in continuous time. Obviously, continuous time power systems dynamic behaviour can only be approximated through sampled power system measurements. Discrete Hilbert Transform (DHT) algorithm of Matlab® package is based on the fundamental result that the Fourier spectra of the original and analytic signals are identical at positive frequencies, whereas at negative frequencies, the FT of the analytic signal is zero [82]. More specifically, *hilbert* command of Matlab® calculates the discrete-time analytic signal through the discrete approximation of the FT. Therefore the HT of the original time-discrete signal is extracted as the imaginary part of the discrete-time analytic signal. The advantage in computing HT via the DFT is to avoid performing a convolution operation, exploiting the speed and the simplicity of the standard FFT routine. Disadvantages are essentially due to the aliasing inherent in the application of the DFT to a signal which is improbably real-band-limited and to the Gibb's phenomena at the ends of the observation window. The first issue can only be mitigated and not completely solved by increasing the sampling frequency the second one has been addressed in this thesis through the Hilbert Boche approach, tailoring a flexible routine in Matlab® environment.

### 4.2.1 Hilbert Boche approach

Let consider the class of square integrable and  $\pi$ -band-limited functions (in  $\pi$  for sake of standardization), indicating it as  $\mathbf{W}_\pi$  and let  $g \in \mathbf{W}_\pi$ . Given an enumerable set of discrete instants  $\{t_i\}$  and denoting with  $\{x_i\}$  the corresponding values for which  $g$  exists, that is  $g(t_i)=x_i$ , a similar approximating expression adopted in the Shannon sampling series [83] is here considered:

$$g_n(t) = \sum_{k=1}^n b_{k,n} \frac{\sin(\pi(t-t_k))}{\pi(t-t_k)} \quad 4.29$$

$$g_n(t_i) = \sum_{k=1}^n b_{k,n} \frac{\sin(\pi(t_i-t_k))}{\pi(t_i-t_k)} \quad 4.30$$

where the coefficients  $b_{k,n}$  can be computed through the resolution of the following system of  $n$  linear equations:

$$\mathbf{g} = \mathbf{A}\mathbf{b} \quad 4.31$$

with

$$\mathbf{g} = \begin{bmatrix} g_n(t_1) \\ \vdots \\ g_n(t_n) \end{bmatrix} \quad \mathbf{A} = \begin{bmatrix} a_{11} & \cdots & a_{1n} \\ \vdots & a_{lk} & \vdots \\ a_{n1} & \cdots & a_{nn} \end{bmatrix} \quad \mathbf{b} = \begin{bmatrix} b_{1n} \\ \vdots \\ b_{nn} \end{bmatrix}$$

The elements of the matrix  $\mathbf{A}$  are of the type  $a_{ik} = \frac{\sin(\pi(t-t_k))}{\pi(t-t_k)}$ , hence for  $t_i \neq t_k$

and for  $i \neq k$   $\mathbf{A}$  is regular and positive definite as well as symmetric. The procedure proposed by Boche and Protzmann in [84] consists in beginning with a first point  $t_i$ , in each iteration step an additional point is added, giving the dimension  $n$  in the  $n^{\text{th}}$  step in Eq. 4.31. The choice of  $t_i$  follows the criterion that follows.

For  $g \in \mathbf{W}_\pi$  the sequence of  $\{g_n\}$ , with  $g_n \in \mathbf{W}_\pi$  converges with  $g$  in  $L^2(-\infty, +\infty)$  resulting:

$$\lim_{n \rightarrow \infty} \int_{-\infty}^{\infty} |g_n(t) - g(t)|^2 dt = 0 \quad 4.32$$

Because of the particular properties of the class  $\mathbf{W}_\pi$  the sequence  $\{g_n\}$  converges not only in  $L^2(-\infty, +\infty)$  but pointwise and even, too:

$$\lim_{n \rightarrow \infty} \int_{-\infty}^{\infty} \sup_{t \in \mathbb{R}} |g_n(t) - g(t)| dt = 0 \quad 4.33$$

Whereby, the instant  $t_i$  for the next step can be selected by identifying the maximum of the values difference  $|g_n(t_i) - g(t_i)|$ . The knowledge of this maximum may be used for terminating the iteration.

The conjugate series of the one in Eq. (4.29), so the related Hilbert transform, is given by:

$$H\{g_n(t)\} = \sum_{k=1}^n b_{k,n} \frac{1 - \cos(\pi(t - t_k))}{\pi(t - t_k)} \quad 4.34$$

for every  $g \in \mathbf{W}_\pi$  converges against the Hilbert transform of the function  $g$  with a pointwise or  $L^2(-\infty, +\infty)$  approximation error not greater than that of the series in Eq. (4.29) itself. In this manner, a powerful approximation function is provided without particular complications. Therefore the analytical form of a generic signal  $x(t)$  can always be determined as follows:

$$x(t) + iX_H(t) = \sum_{k=1}^n b_{k,n} \frac{\sin(\pi(t - t_k))}{\pi(t - t_k)} + i \sum_{k=1}^n b_{k,n} \frac{1 - \cos(\pi(t - t_k))}{\pi(t - t_k)} \quad 4.35$$

with  $b_{k,n}$  that are the same in any sum.

The adoption of such a procedure allows to reduce rather significantly the Gibb's effects in Hilbert transform. This can result very useful when the analytical expression of the investigated signal HT is known, in a perspective to fit the mentioned expression to the numerical values provided by the Hilber-Boche (HB) approximation. Let consider for instance the signal in the Eq. 4.36:

$$x(t) = e^{-0.1t} \sin(2\pi 0.25t) \quad 4.36$$

Although this signal is synthetic, its characteristic parameters are chosen to replicate an actual electromechanical oscillation. Actually the value of damping coefficient  $\sigma = -0.1 \text{ s}^{-1}$  and the frequency  $f = 0.25 \text{ Hz}$  match quite exactly those of the ENTSO-e CESA North-South inter-area oscillation. As can be appreciated by the Fig. 4.1, the end effects at the observation window extremities are importantly suppressed through the employment of the HB approach.

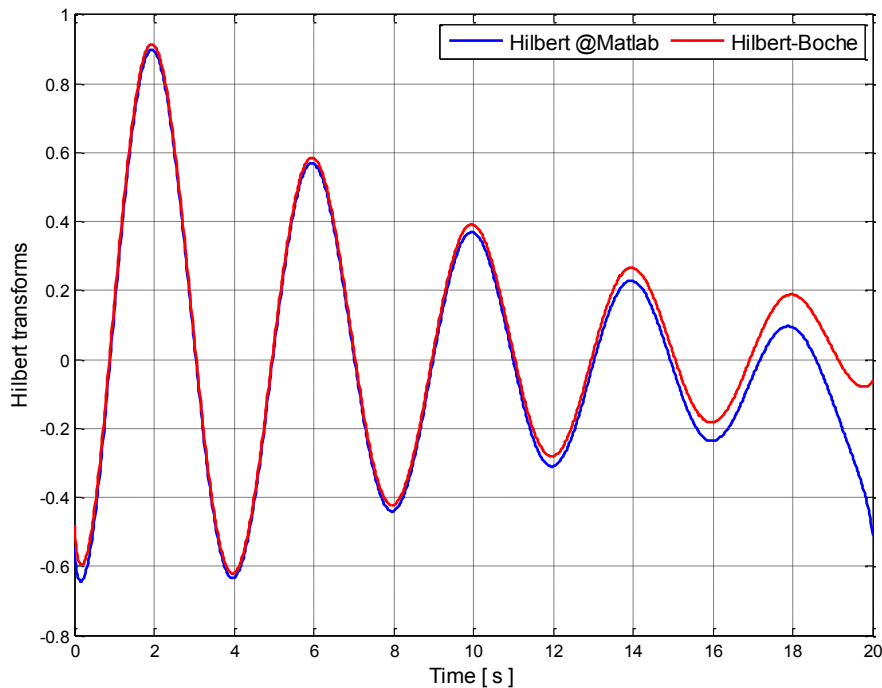


Fig. 4.1 – Hilbert transform of the synthetic signal in (4.36): comparison between the standard routine of Matlab® and the Boche approximation.

### 4.3 An improved non linear least squares method for estimating the damping levels of electromechanical oscillations

In this Section a new estimation algorithm is proposed for estimating the damping of electromechanical oscillations in power systems. The method is based upon a generalization of the classical nonlinear least squares approach which employs further information concerning the finite Hilbert transform of the power signals. A semi-analytic procedure is tailored with the aim to get an expression of the Cauchy principal value integral to suitably include in the objective function of the least squares minimization. The methodology is found to be very accurate in damping estimation as well as resilient against a critical effect of the wide area communication networks, namely dropout packets. This is partially due to the inherent regularization action of the Hilbert transform in correspondence of the data lack.

The proposed procedure for estimating the characteristic parameters of electromechanical oscillations is organized into two steps. The first one consists

March 2014

in decomposing the original power systems signals into elemental components according to the theorem presented in the Section 4.1.1. This separator block, as already said, ensures the mono-component trait of each decomposed elemental component. The basic assumption in the non linear least squares procedures that will be presented in the sequel is to adopt an exponential damped sinusoid model, hereafter *standard fitting model*, for each elemental component furnished by the previous separator block:

$$x_i^d(t) \cong A_i e^{\sigma_i t} \sin(\omega_i t + \varphi_i) \quad 4.37$$

with  $A_i$  the instantaneous component amplitude,  $\sigma_i$  the component damping coefficient in ( $s^{-1}$ ),  $\omega_i$  the component angular frequency in (rad/s) and at last  $\varphi_i$  the component phase in (rad).

The second one consists in applying, on each of the previous elemental signals, a non linear least squares optimization considering an objective function that includes information related to the component Cauchy principal value integral. The latter relationship is derived through the semi-analytic procedure that follows. The main difference with respect to the classical NLS procedure presented in the Section 3.5, the VARPRO, relies in the development of a specific objective function able to offer better accuracy and consistency to the whole estimation procedure. The new objective function includes information about the Cauchy principal value integral of the elemental component  $x_i^{(d)}(t)$ . In detail, the novel objective function,  $\mathbf{LH}_i$ , has so been designed:

$$\mathbf{LH}_i(\boldsymbol{\alpha}_i, \boldsymbol{\beta}_i) = \sum_{j=1}^h \left\{ H[x_i^d(t_j)] - \text{CPVI}[x_i^d(t_j)] \right\}^2 \quad 4.38$$

where:

- $H[.]$  is a local Hilbert transform operator specifically implemented according to the Boche approach, in order to reduce the Gibb's effect, then enhancing the estimation procedure accuracy;
- CPVI is the Cauchy principal value integral of the standard fitting model containing the problem unknowns.

CPVI expression, defined in the Eq. (4.38), can be numerically computed through the tailored semi-analytic procedure. Rigorously speaking, CPVI is defined as:

$$\begin{aligned}
 \text{CPVI} &= \frac{1}{\pi} \text{P.V.} \int_{t_a}^{t_b} \frac{C_{1i} e^{\sigma_i \tau} \sin(2\pi f_1 \tau) + C_{2i} e^{\sigma_i \tau} \cos(2\pi f_1 \tau)}{t - \tau} d\tau \\
 &= \frac{1}{\pi} \text{P.V.} \int_{t_a}^{t_b} \frac{C_{1i} e^{\sigma_i (t-\tau)} \sin(2\pi f_1 (t-\tau)) + C_{2i} e^{\sigma_i (t-\tau)} \cos(2\pi f_1 (t-\tau))}{\tau} d\tau
 \end{aligned} \tag{4.39}$$

It can be determined, as demonstrated later, by evaluating the Cauchy principal value integral of the following oscillatory function:

$$I_\omega(f; t) = \text{P.V.} \int_{t_a}^{t_b} e^{i\omega\tau} \frac{e^{\sigma\tau}}{t - \tau} d\tau \tag{4.40}$$

where the function  $f(\tau) = e^{\sigma\tau}$  is surely analytic in a sufficiently large region of the complex plane containing  $[t_a, t_b]$ . Such an integral, although shows difficulties in the solution related to the Cauchy type singularity and to the intrinsic oscillatory nature, exists since  $f$  satisfies Holder's condition [85].

By denoting the complex plane regions  $\Omega$  and  $\Omega'$  in the following manner:

$$\Omega = \{z \in \mathbb{C} \mid t_a \leq \Re(z) \leq t_b, 0 \leq \Im(z) \leq \eta\} \tag{4.41}$$

$$\Omega' = \{|z - t| \leq r, 0 \leq \arg(z) \leq \pi\} \tag{4.42}$$

where  $\eta$  is a large number and  $r$  is small enough such that  $\Omega' \subseteq \Omega$ .

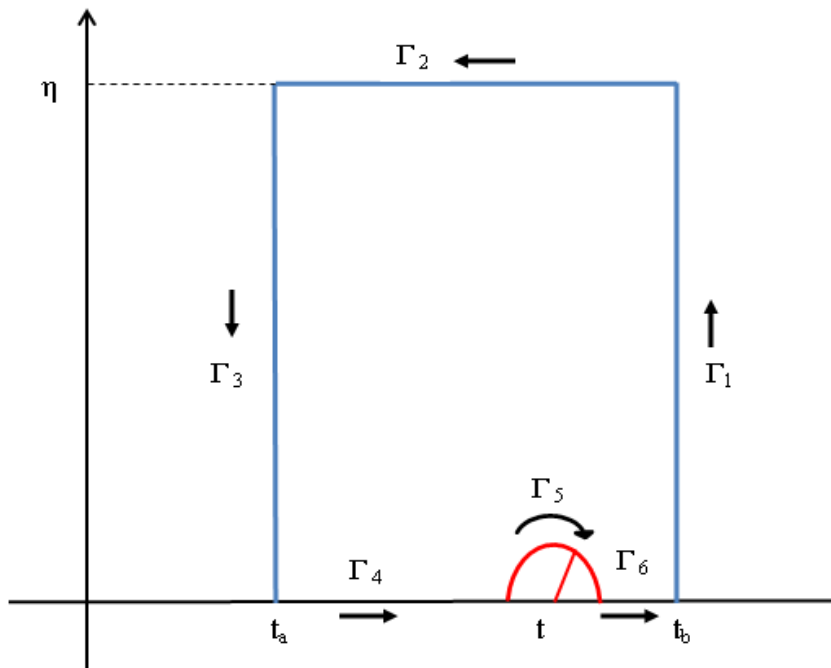


Fig. 4.2 – Path of integration for  $I_\omega(f; t)$

According to the theorem in [86], the integral in the Eq. (4.40) can be evaluated as:

$$I_{\omega}(f; t) = -ie^{i\omega t} \pi e^{\sigma t} - \frac{ie^{-i\omega t_a}}{\omega} \int_0^{+\infty} e^{(-x)} \frac{e^{\sigma\left(t_a + \frac{ix}{\omega}\right)}}{t_a - t + \frac{ix}{\omega}} dx + \frac{ie^{-i\omega t_b}}{\omega} \int_0^{+\infty} e^{(-x)} \frac{e^{\sigma\left(t_b + \frac{ix}{\omega}\right)}}{t_b - t + \frac{ix}{\omega}} dx \quad 4.43$$

The theorem proof is reported in the Appendix B. Indeed, the two integrals in the equation above can be evaluated by employing the Gauss-Laguerre quadrature rule. More specifically, by respectively denoting with  $x_k$  and  $w_k$ , the nodes and the weights of the  $n$ -point Gauss-Laguerre quadrature rule, C.P.V. integral in Eq. (4.43) can be approximated by the following relationship.

$$I_{\omega}(f; t) \approx -ie^{i\omega t} \pi e^{\sigma t} - \frac{ie^{-i\omega t_a}}{\omega} \sum_{k=1}^n w_k \frac{e^{\left(t_a + \frac{ix_k}{\omega}\right)}}{t_a - t + \frac{ix_k}{\omega}} + \frac{ie^{-i\omega t_b}}{\omega} \sum_{k=1}^n w_k \frac{e^{\left(t_b + \frac{ix_k}{\omega}\right)}}{t_b - t + \frac{ix_k}{\omega}} \quad 4.44$$

In the numerical simulations, a 5-point Gauss-Laguerre quadrature rule has been used whose associated  $x_k$  and  $w_k$  values are listed in Table 1 [87].

TAB. 4.1 - NODES AND WEIGHTS FOR GAUSS - LAGUERRE  
5 POINTS QUADRATURE RULE

<b>Gauss-Laguerre quadrature rule with 5 points</b>	
$x_k$ nodes	$w_k$ weights
$x_1=0.26356$	$w_1=0.521756$
$x_2=1.4134$	$w_2=0.398667$
$x_3=3.59643$	$w_3=0.0759424$
$x_4=7.08581$	$w_4=0.00361176$
$x_5=12.6408$	$w_5=0.00002337$

The analytical expression (4.44) allows to evaluate in a simple way the Cauchy principal value integral in (4.39), since:

$$\text{P.V.} \int_{t_a}^{t_b} \cos(\omega\tau) \frac{e^{\sigma\tau}}{t-\tau} d\tau = \Re \left[ \text{P.V.} \int_{t_a}^{t_b} e^{i\omega\tau} \frac{e^{\sigma\tau}}{\tau-t} d\tau \right] \approx \Re(I_\omega(f; t)) \quad 4.45$$

$$\text{P.V.} \int_{t_a}^{t_b} \sin(\omega\tau) \frac{e^{\sigma\tau}}{t-\tau} d\tau = \Im \left[ \text{P.V.} \int_{t_a}^{t_b} e^{i\omega\tau} \frac{e^{\sigma\tau}}{\tau-t} d\tau \right] \approx \Im(I_\omega(f; t)) \quad 4.46$$

As consequence of that:

$$\mathbf{LH}_i(\boldsymbol{\alpha}_i, \boldsymbol{\beta}_i) = \sum_{j=1}^h \left\{ \mathbf{H}[y_i^d(t_j)] - \text{CPVI}[y_i^d(t_j)] \right\}^2 = \sum_{j=1}^h \left\{ \mathbf{H}[y_i^d(t_j)] - \frac{1}{\pi} [C_{1i} \Im\{I_\omega(f; t_j)\} + C_{2i} \Re\{I_\omega(f; t_j)\}] \right\}^2 \quad 4.47$$

It is easy to argue that also in this case the problem structure is suitable to be addressed through VARPRO algorithm, by decoupling the estimates of  $\boldsymbol{\alpha}_i$  and  $\boldsymbol{\beta}_i$ . To demonstrate the effectiveness of the present algorithms the following synthetic bi-modal signal is here considered

$$y(t) = 8e^{-0.1t} \sin(1.6\pi t) + 20e^{-0.3t} \sin(\pi t) \quad 4.48$$

Such a test signal is particularly critical for M-EMD due to its inability to effectively separate the signal components. Conversely, the proposed preliminary separation theorem allows to reproduce without difficulties both the closely-spaced frequency components having mono-component trait. For sake of brevity, the  $L_p$  periodogram output, depicting the signal spectrum is not reported since, in this case, a simple FFT is sufficient to identify the spectrum peaks and hence the bisecting frequency  $\omega_b$  required by the decomposition procedure. In particular, Fig. 4.3 depicts the single components and the decomposed elemental ones according to the decomposition procedure both with respect to standard Hilbert routine of Matlab® and to the one based on Boche method.

March 2014

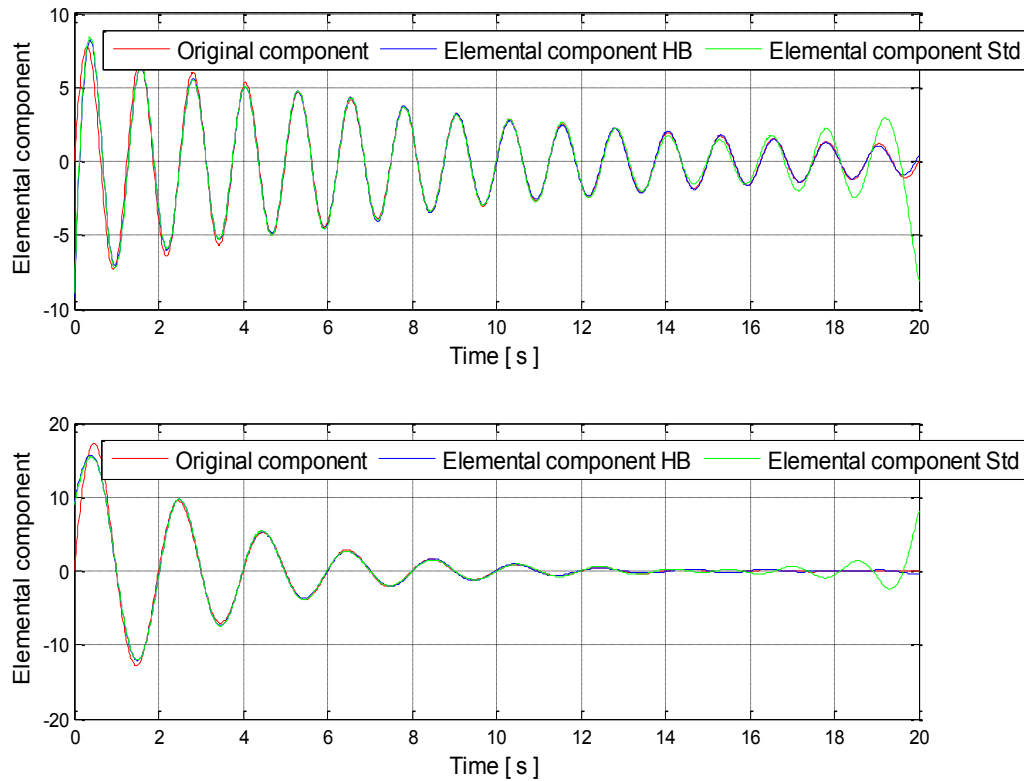


Fig. 4.3 – Time domain decomposition of the signal in (4.48) according to the proposed decomposition theorem: standard HT routine of Matlab® vs adopted one based on Boche method.

As it can be appreciated, the HT calculated with the Boche method permits to significantly reduce the Gibb's phenomena at the signal ends ensuring higher performance in the estimation process with respect to an ordinary use of the *hilbert* command of Matlab®. Each elemental component is fed to the standard VARPRO and to the improved NLS algorithm, assessing the damping estimation accuracy with respect to different rate of data packets loss, appreciable in Figures 4.4a, 4.4b and 4.4c. A deep discussion about the data packet dropouts issue and its modelling will be performed in the next Chapter, for now suppose to have the three following situations.

March 2014

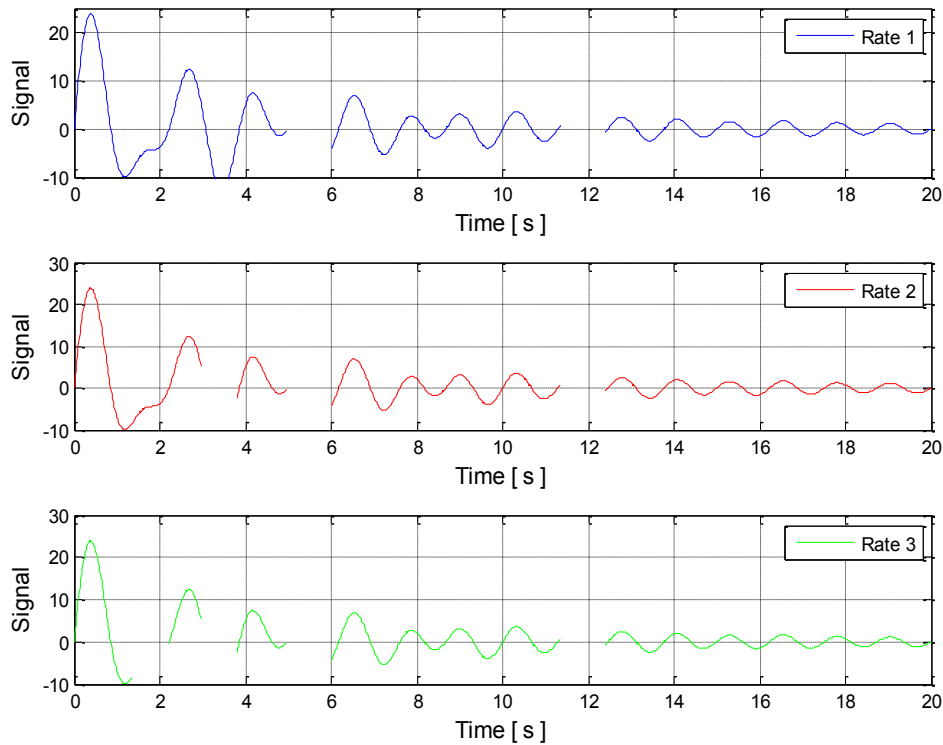


Fig. 4.4 – Data packet dropouts: a) Rate 1, b) Rate 2, c) Rate 3.

As can be noted by the achieved numerical results in Table 4.2, the improved NLS algorithm generally offers better performance with respect to the standard one. If a data packet dropout occurs, whatever would be its entity, the improved NLS approach ensures a much more consistent behaviour. The case of signal correctly transmitted is a singular one in the sense that, as demonstrated in our recently submitted paper being evaluation [88], in the situation of real measured signals the proposed NLS is ever better than the standard one (also in the case of signal correctly transmitted). The experimental findings are here not reported for sake of brevity since the example above is only devoted to validate the tailored algorithm. More specifically, the higher the loss rate, the more resilient is the improved NLS approach performing. Therefore the adoption of an objective function which minimizes the residual between the local HT performed through Hilbert-Boche method and the CPV integral expression obtained from the developed semi-analytic procedure seems more appropriate.

TAB. 4.2 – DAMPING ESTIMATION OUTCOMES: VARPRO vs IMPROVED NLS.

	Signal correctly transmitted		Data packet dropouts rate 1		Data packet dropouts rate 2		Data packet dropouts rate 2	
	$x_1^d(t)$	$x_2^d(t)$	$x_1^d(t)$	$x_2^d(t)$	$x_1^d(t)$	$x_2^d(t)$	$x_1^d(t)$	$x_2^d(t)$
Classical	0.0974	0.2914	0.1131	0.4451	0.1213	0.4459	0.1270	0.4450
Improved	0.0967	0.2745	0.1111	0.3498	0.1192	0.3488	0.1248	0.3484

Furthermore the preliminary components separation, performed according to the presented decomposition theorem HT-based, represents a great advantage with respect to the same phenomenon due to the intrinsic regularization action of the HT, as it can be noted in Fig. 4.5.

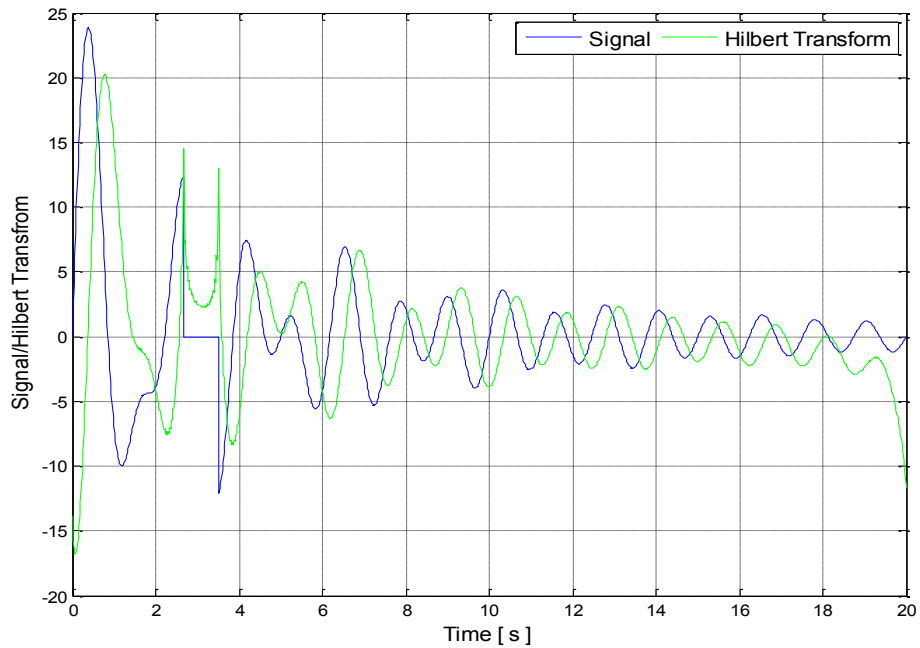


Fig. 4.5 – HT regularization action with respect to the data packet dropouts

## Chapter 5

### *Experimental Findings*

In this Chapter a wide collection of experimental findings obtained from the in-field employment of the estimation algorithms included in the Chapter 3 and Chapter 4 is reported. The case studies refer to synthetic signals, near real life signals acquired by simulation on IEEE test networks and at last actual measured signals in ENTSO-e CESA by the Italian WAMS. A performance comparison among the different estimation techniques, in essentially tracking frequency and damping of the actual or simulated electromechanical oscillations, is performed. In this sense, keeping in mind the lack of a rigorous definition of optimality, the algorithms accuracy is assessed by measuring how far the provided estimates are from the ones of the modal analysis, in the case of IEEE test benches, or from the average value recorded in literature about real systems (when known), in the case of real measurements from interconnected European system. An adequate discussion about the achieved numerical findings is provided aimed at furnishing a reasonable interpretation. The effects of some wide area communication networks, such as noise and data packet dropouts, is also evaluated to measure the inherent robustness of each considered algorithms.

#### 5.1 A synthetic signal

The signal under investigation is of particular interest due to the fact that the standard HHT and the M-EMD fail in extracting mono-component elemental signals as already said in the Section 4.3. Let consider hence a damped version of the signal employed in [76] :

$$x(t) = 8e^{-0.1t} \sin(1.6\pi t) + 20e^{-0.3t} \sin(\pi t) \quad 5.1$$

March 2014

The signal, depicted in Fig. 5.1 related to an observation window of 20 s, is fed to all the estimation algorithms after a simple mean removal. There is no need for any particular digital filtering operation.

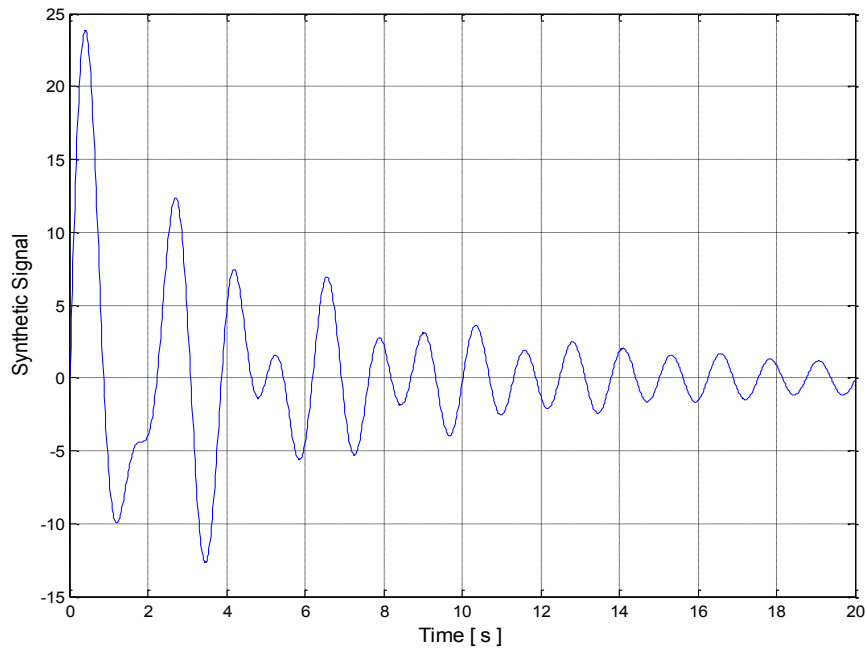


*Fig. 5.1 – Synthetic signal*

Before to analyze the outcomes provided by the estimation algorithms, we believe necessary to test the decomposition capability of the HHT refinements presented in the Chapter 3, specifically HHT with standard masking technique, M-EMD, and EMD with Fourier-Based Masking Technique, R-EMD, with respect to the HT-based one described in the Chapter 4. Actually, in this simple case, the standard EMD is not able to furnish the real frequency and damping coefficient for each component: the first two IMF are characterized by a frequency  $f_1 = 0.6636$  Hz and  $f_2 = 0.2592$  Hz and a damping coefficient  $\sigma_1 = -0.1305$  s<sup>-1</sup> and  $\sigma_2 = -0.1259$  s<sup>-1</sup>. The IMF extracted by the M-EMD instead are plotted in Fig. 5.2. Due to the mode mixing in the first IMF, as confirmed in Fig. 5.3, although the estimate is improved with respect to the ordinary EMD in terms of frequency ( $f_1 = 0.8298$  Hz  $f_2 = 0.4171$  Hz) the modes damping values are fairly underestimated ( $\sigma_1 = -0.0340$  s<sup>-1</sup> and  $\sigma_2 = -0.0519$  s<sup>-1</sup>).

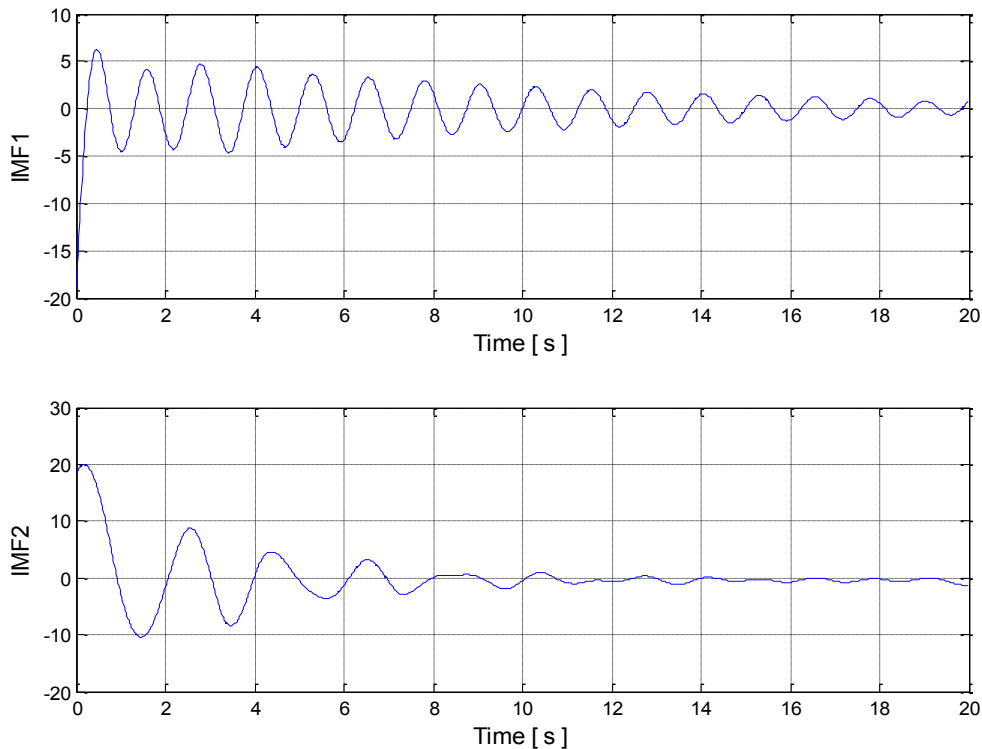


Fig. 5.2 – IMF from M-EMD: synthetic signal.

The M-EMD inability to separate components with closely spaced frequency components is so pointed out. The drawbacks above can be overcome through the adoption of the R-EMD. In fact, in this manner also the damping coefficient estimations are enhanced ( $\sigma_1 = -0.0791 \text{ s}^{-1}$  and  $\sigma_2 = -0.1776 \text{ s}^{-1}$ ) and the mode mixing issue is mitigated. Without any doubt the potentiality of the R-EMD is partially conditioned by the damping effect, since an undamped version of the signal in (5.1) would show a much more effective action, as confirmed in reference [76]. The decomposition procedure, and hence the subsequent oscillations parameters estimation, can be enhanced by adopting the estimation algorithm described in the Chapter 4, hereafter Lauria-Pisani method (LPM). The estimation algorithm application requires the preliminary determination of the bisecting frequency (or angular velocity) via  $L_p$  periodogram. The latter, for  $p = 1.5$ , is illustrated in Fig. 5.4 together with the ordinary Fourier spectrum of the signal in (5.1).

March 2014

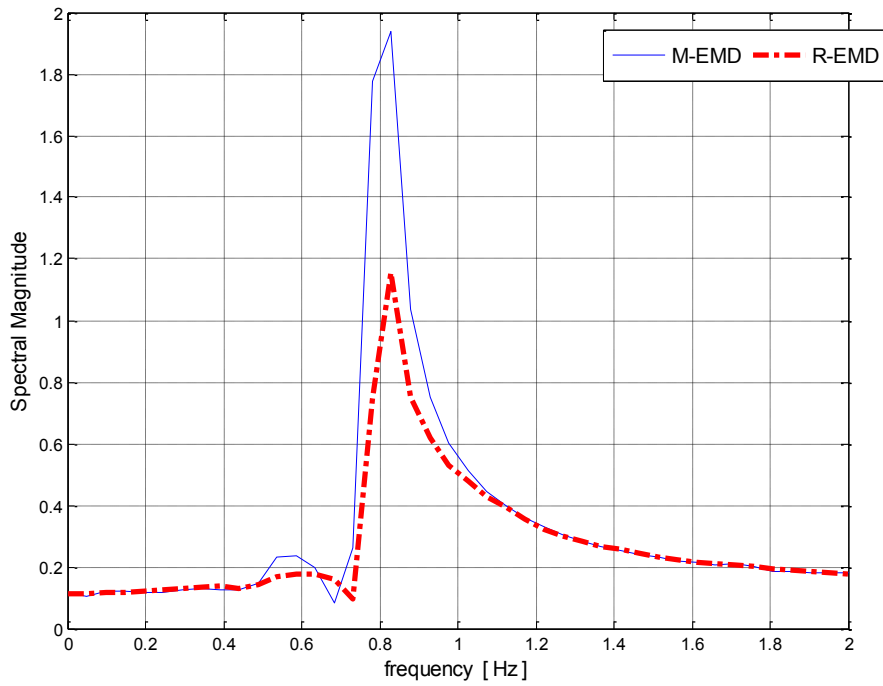


Fig. 5.3 – First IMF Fourier spectrum in the case of M-EMD and R-EMD application.

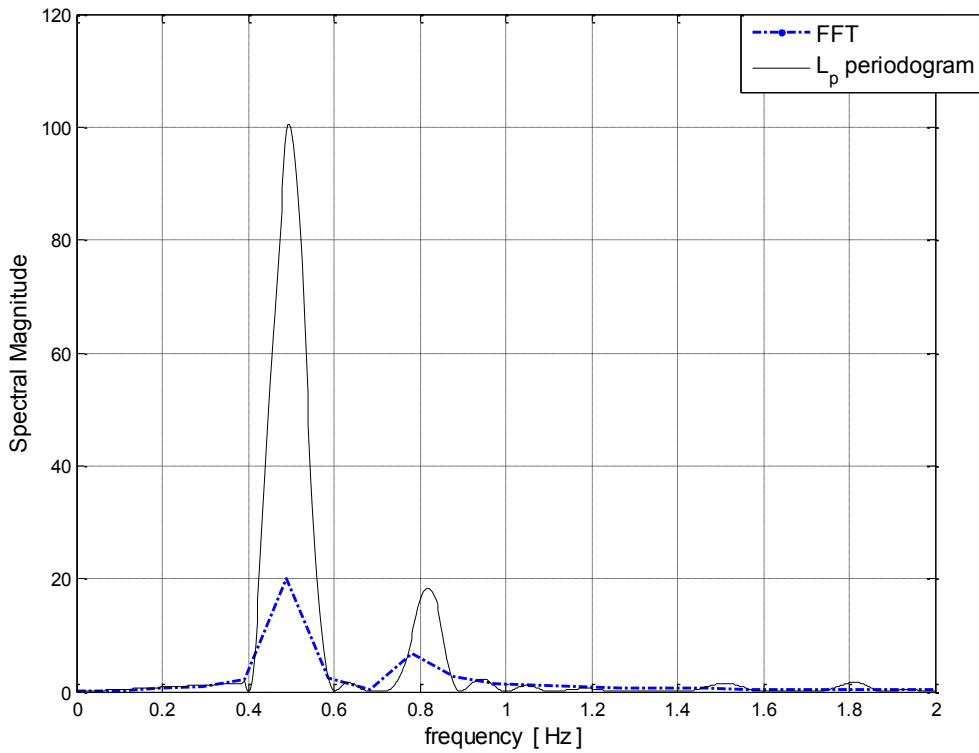


Fig. 5.4 – FFT and  $L_p$  periodogram : synthetic signal.

The bisecting frequency determined by averaging the peaks of the  $L_p$  periodogram is  $f_b = 0.6509$  Hz ( $\omega_b = 4.0897$  rad/s). Once computed the bisecting frequency the two components can be extracted according to the decomposition theorem presented in the Chapter 4. The result of this operation is shown in Fig. 5.5.

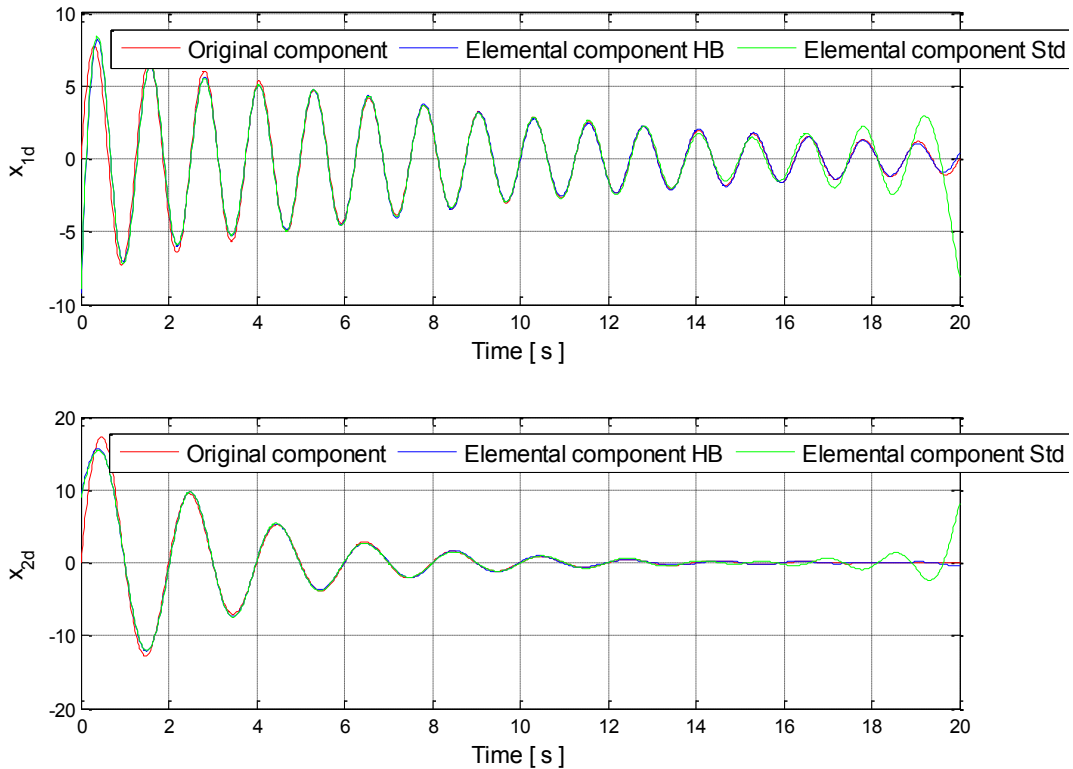


Fig. 5.5 – Time domain decomposition of the un-damped synthetic signal: comparison between standard Hilbert Transform and Hilbert Boche approximation.

As shown in Fig. 5.5 the approximation is really satisfactory and furthermore the employment of the Hilbert-Boche method for computing the HT significantly reduces the Gibb's effect. At this point the performance comparison of all the estimation algorithms can be accomplished. The numerical outcomes obtained are listed in Tab. 5.1. First of all, in this case study a superiority of the SVD based covariance-based methods, which are Tufts-Kumaresan method, TKM, and Hankel Singular Value Decomposition – VARIable PROjection method, VARPRO, with respect to the ones HT-Based, exactly R-EMD and LPM is pointed out. Furthermore the estimations of the Extended Complex Kalman Filter (HSVD assisted) are not reported for reasons that will be clarified in the short. It can be stated that while HT-based estimation algorithms suffer from the closeness of the frequency components of

the signal in (5.1) the other ones do not. This is essentially due to the philosophy behind the techniques: in this case the attempt to extract details about the single component involves a loss of accuracy in its parameters estimation.

TAB. 5.1 - ESTIMATION ALGORITHMS OUTCOMES - SYNTHETIC SIGNAL

TKM		HSVD-VARPRO		ECKF		R-EMD		LPM	
$\sigma$ [s <sup>-1</sup> ]	f [Hz]								
-0.1000	0.8000	-0.1000	0.8000	-	-	-0.0764	0.8307	-0.1001	0.8181
-0.3000	0.5000	-0.3000	0.5000	-	-	-0.2196	0.4702	-0.3000	0.4946

In particular, although synthetic, the considered signal is very critical also for the ECKF and the motivations are to be found in the frequency components proximity. This estimation algorithm in fact detects the presence of two modes with similar characteristics. Being the estimations not consistent in this sense, were not reported in Tab. 5.1.

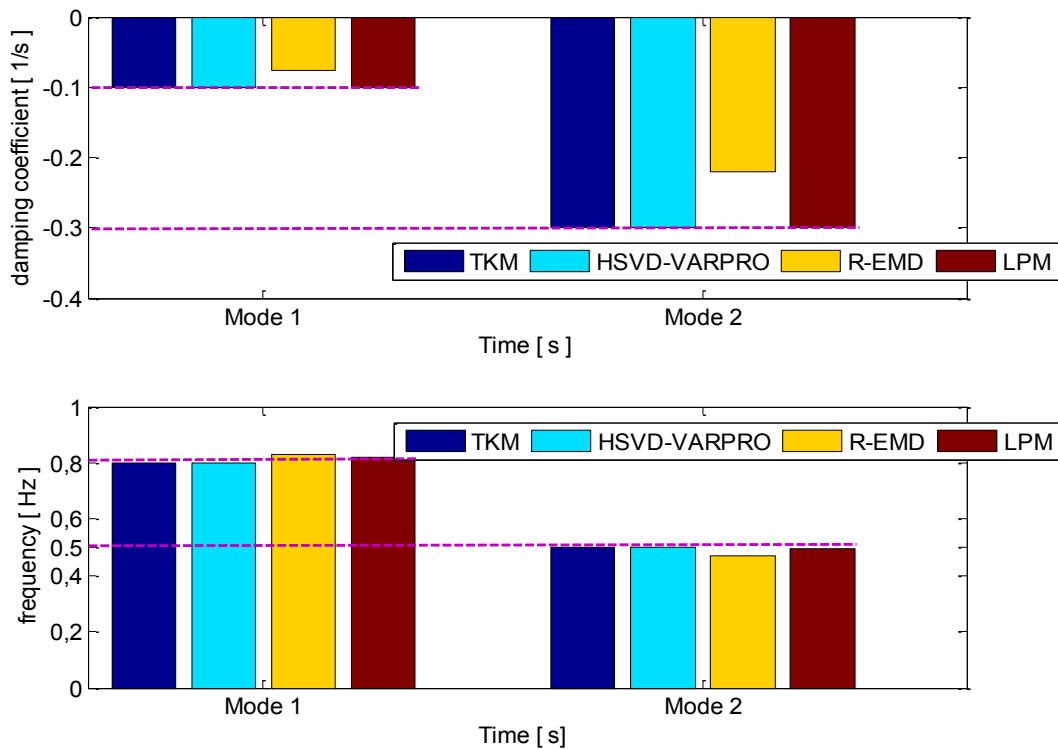


Fig. 5.6 – Estimation accuracy bar graph : synthetic signal.

March 2014

Actually, once frozen the observation window duration and changing the damping coefficients associated to the first frequency component in  $f_1 = 2.3$  Hz, the filter output is the following one:  $f_1 = 2.2850$  Hz  $\sigma_1 = -0.0956$  s<sup>-1</sup> and  $f_2 = 0.329$  Hz  $\sigma_2 = -0.2934$  s<sup>-1</sup>. Undoubtedly the fact that one components decays more quickly than the other one implies that a reduction of the observation window duration can offer better results. This is a trick that should be keep clear in mind as further drawback of the ECKF in addition to its inherent weakness in the parameters estimation of high damped electromechanical oscillations. It has been verified in conclusion that this behaviour exclusively depends on the issue outlined above and not on the damping values or on the difference in the components amplitude.

### 5.1.1 Incidence of WAMS communication network effects

WAMS communication networks, responsible for data exchange among measurement systems, control centers and controllable devices, assume a critical role in a complex system devoted to an on-line DSA. This is due to the fact that, as recognized in the accredited literature, e.g. in [89], some network effects could jeopardize the proper operating of the supervisory and control systems. A supervisory system robust design implies an appropriate taken into account of these effects in order to avoid potential misoperations that can lead the electrical power system in unsafe conditions. More specifically, the main WAMS communication network effects to pay careful attention are noise, network-induced delays, data packet dropouts and data packet disordering. It appears rather clear that the WAMS's working signals are intrinsically affected by noise due to the power system, i.e. by small load variations, and to the measurement process. Network induced delay, or as often called *latency*, is strictly related to the WAMS's structure: it can vary from tens to several hundred milliseconds, depending on routines of signal transmission, transmission protocols, communication load and communication channel [90]. In addition, the possibility that data may be lost while in transit through the transmission network should not be excluded. Apart from the uncertainties and noise in communication channels, the main causes are ascribable to transmission errors in physical links, to buffer overflows caused by congestion and so on. Latency is sometimes intimately linked to this issue. Actually, in reference [18] the authors argue that long transmission delays sometimes result in packet reordering which corresponds to a packet dropout if the receiver discards outdated arrivals. Although most network protocols are equipped with transmission-retry mechanisms, they can only retransmit after a limited time. If this time expires, the packets will be dropped. These considerations

confirm that data packet dropouts issue effectively represents a potential threat for the correct operating of the estimation algorithms. The last but not least WAMS communication network effect worthy of considering is the data packet disordering. This issue describes the actual condition in which data packets sent earlier than others may arrive at the destination later. It is caused by the redundancy of communication paths available in real context. The framework just described makes appropriate the investigations performed in the next Sections.

### 5.1.1.1 Noise incidence

High levels of noise could seriously affect the performance of some estimation algorithms. For this reason a deep analysis devoted to analyze their response with respect to different levels of signal to noise ratio must be performed. In particular the results here reported refer to an addition of white Gaussian noise to the signal in (5.1) through several SNR values expressed in dB.

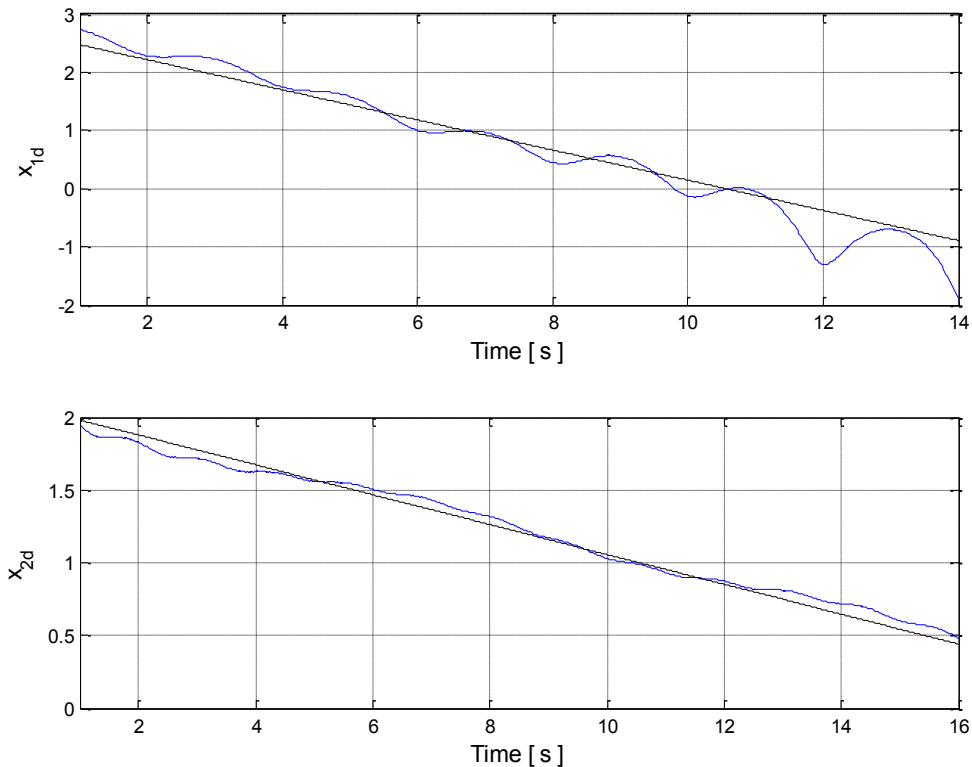
TAB. 5.2 – ESTIMATION ALGORITHMS OUTCOMES WITH RESPECT TO THE NOISE  
– SYNTHETIC SIGNAL

SNR	TKM		HSVD-VARPRO		R-EMD		LPM	
[dB]	$\sigma$ [s <sup>-1</sup> ]	f [Hz]						
120	-0.1000	0.8000	-0.1000	0.8000	-0.0782	0.8503	-0.1001	0.8181
	-0.3000	0.5000	-0.3000	0.5000	-0.1772	0.5600	-0.3000	0.4946
80	-0.1000	0.8000	-0.1000	0.8000	-0.0782	0.8503	-0.1001	0.8181
	-0.3000	0.5000	-0.3000	0.5000	-0.1772	0.5600	-0.3000	0.4946
40	-0.1001	0.8000	-0.1000	0.8000	-0.0774	0.8508	-0.1001	0.8181
	-0.3002	0.5001	-0.3001	0.5001	-0.1767	0.5601	-0.3001	0.4946

March 2014

20	-0.1042	0.8001	-0.0999	0.8001	-0.0651	0.8720	-0.1011	0.8180
	-0.3026	0.5008	-0.2999	0.5008	-0.1736	0.5613	-0.3012	0.4950
10	-0.1247	0.8051	-0.1007	0.8051	-	-	-0.1011	0.8180
	-0.3446	0.5002	-0.3033	0.5002	-0.1591	0.5591	-0.3012	0.4950

Tab. 5.2 collects the achieved algorithms outcomes for several noise levels. As can be derived from these values, HSVD-VARPRO and LPM are almost insensible to the noise levels. Hence, the least squares algorithm is able to recognize the inherent signal modal content even if strong noise is superimposed to the observed signal. As far as the LPM method, this strength arises from the joint robustness of the  $L_p$  periodogram to the noise and of the damping computation practice described in the related Section. Actually as can be appreciated in Fig. 5.7 and Fig. 5.8, the regression line of the decaying amplitude for each decomposed elemental component remains unchanged both in the case of noiseless signal and in the case of SNR = 10 dB.



ig. 5.7 – Damping computation via LPM : noiseless signal.

The influence of the TKM to the noise has been already ascertained by its developers establishing a simple concept: the SVD-based covariance methods are generally affected by noise. The perturbations introduced by the noise in the vector of the backward prediction coefficients  $B(z)$  can be only partially mitigated, hence roughly speaking the higher the noise the worse the estimate. In the Section that follows TKM behaviour will be characterized in the case of data packet dropouts.

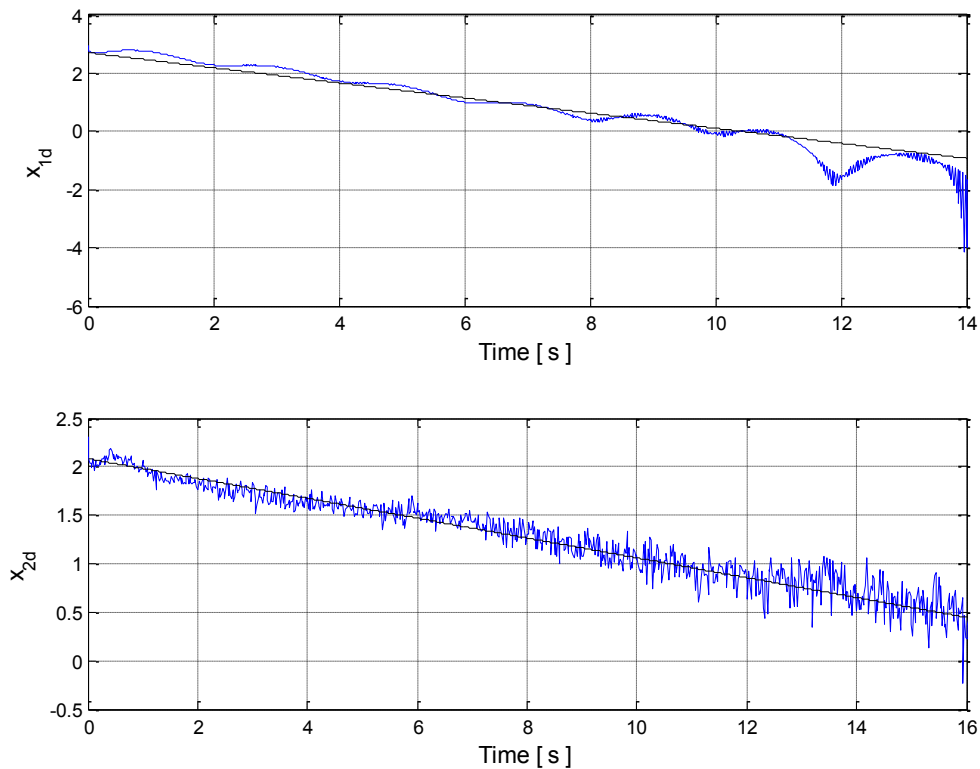


Fig. 5.8 – Damping computation via LPM: synthetic signal, SNR = 10 dB.

R-EMD seems to suffer from the presence of noise in the case of SNR = 10 dB. In this case an enlargement of the observation window is useless and however an extra-production of fictitious IMF occurs. In any case, in relation to what was found, an adequate digital filtering could be suggested before to feed the sampled signals to any adopted mode meter.

### 5.1.1.2 Data packet dropouts incidence

Due to the technological complexity of the WAMS communication network sometimes the acquired signals could not be intact but instead a loss of inherent carried information could occur. For this reason a further analysis devoted to analyze the response of the estimation algorithms with respect to different rate of data loss must be performed. Data packet dropouts modelling can be faced by adopting either stochastic or deterministic criteria. It appears clear, however, that a probabilistic phenomenon description is more appropriate than a deterministic one. Although there exists more detailed stochastic models, based for instance on finite-state Markov chains or on Poisson processes, in this thesis a Bernoulli data packet dropouts model has been adopted for characterizing such a recorded issue in WAMS communication networks.

Therefore, let us consider of having  $k$  samples to send through a communication network, one can introduce a stochastic variable  $\Theta_k$  which assumes value 1 if the sample arrives to the destination (receiver) and the value 0 otherwise [91], [92].

$$\Theta_k \in [0,1]; p = \Pr(\Theta_k = 1) \in [0,1], \forall k \in \mathbb{N} \quad 5.2$$

The values of  $\Theta_k$  are independent and identically distributed (i.i.d.) according to a Bernoulli process characterized by a probability  $p$  of having no data loss and hence  $q=1-p$  of having it. Tab. 5.3 lists the results of the estimation algorithms in the case of four different values of  $p$ . The effects of this alteration on the original signal are illustrated in Fig. 5.9 whereas to permit to appreciate them a signal scale modification has been performed.

March 2014

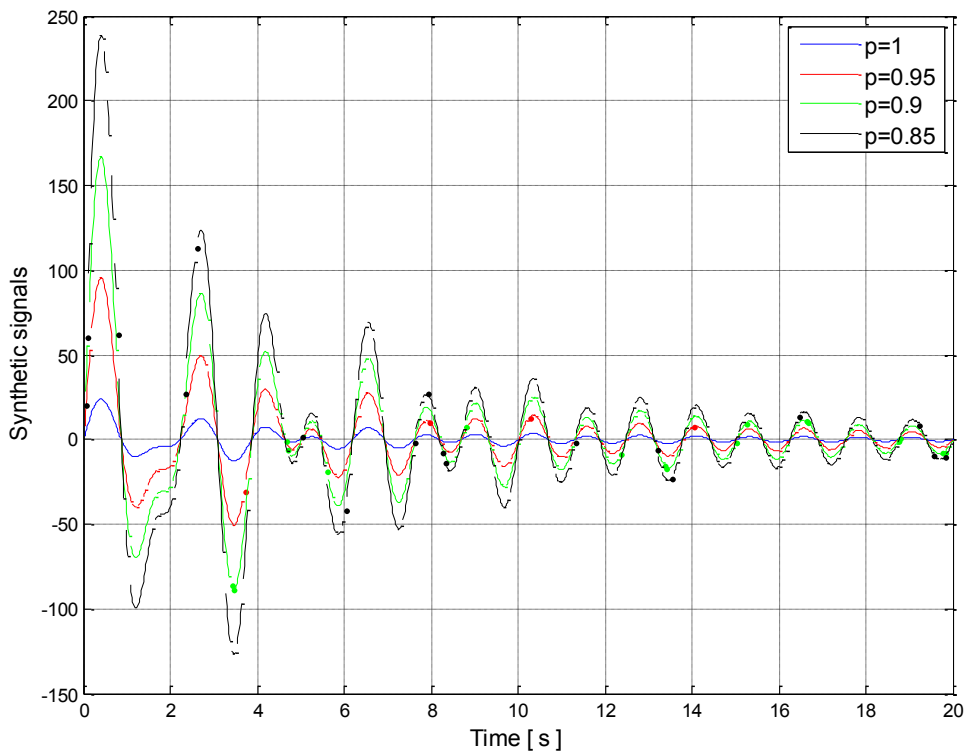


Fig. 5.9 – Change of the  $p$ -value in the Bernoulli process :effect on the synthetic signal.

TAB. 5.3 – ESTIMATION ALGORITHMS OUTCOMES WITH RESPECT TO THE DATA PACKET DROPOUTS – SYNTHETIC SIGNAL

p	TKM		HSVD-VARPRO		R-EMD		LPM	
	$\sigma$ [s <sup>-1</sup> ]	f [Hz]						
1	-0.1000	0.8000	-0.1000	0.8000	-0.0764	0.8307	-0.1001	0.8181
	-0.3000	0.5000	-0.3000	0.5000	-0.2196	0.4702	-0.3000	0.4946
0.95	-0.4790	0.8353	-0.1052	0.8350	-0.0804	0.7369	-0.1031	0.8179
	-0.6082	0.5237	-0.3054	0.5240	-0.1032	0.4450	-0.2821	0.4940
0.9	-0.7226	0.8591	-0.1051	0.8590	-0.0843	0.8162	-0.1059	0.8185
	-0.6841	0.5334	-0.3216	0.5335	-0.0957	0.4898	-0.2792	0.4940

March 2014

	- 1.0449	0.8556	- 0.1056	0.8552	- 0.0310	0.9367	- 0.1065	0.8160
0.85	- 0.8257	0.5706	- 0.2929	0.5710	- 0.0840	0.4898	- 0.2685	0.4931

As can be noted, the results of the TKM generalize the experimental evidence that the method's authors observed solely with respect to the presence of noise in the tested signals: also the packet dropouts implies a significant distortion in the signal subspace, making worse the oscillations parameters estimation. With my supervisors, in reference [93], we shows that the data packet dropouts implies a perturbation in the singular value decomposition. In particular with a reduction of the probability  $p$ , the value of the greater singular values (associated to the dominant modes in the analyzed signal) decrease while the value of the lower singular value (associated to the noise) increase. This means that the subspace of the signal and the subspace of the noise tend to overlap more and more when the number of data packets loss increases. In any case this effect influences much more the damping coefficient estimation than the frequency one. The robustness of the VARPRO is evident also with respect to this WAMS communication network effect. High data loss rates influence in a non-decisive manner the signal parameters estimation. In a certain sense HSVD-VARPRO preserves as the good of the TKM, exactly the frequency estimation accomplished with the same computing approach, improving the damping estimation via a non-linear least squares method resulted really successful. R-EMD confirms that an alteration of the signal in terms of data packet dropouts implies an overproduction of IMF with a consequent general estimation accuracy reduction. On the other hand LPM method shows a good resilience also with respect to the data packet dropouts thanks again to the joint robustness of the  $L_p$  periodogram to the data packet dropouts and of the damping computation practice via the developed regression technique. Similar graphs to the ones in Fig. 5.7 and 5.8 are obtained in this case, not reported for sake of brevity.

In conclusion, the achieved experimental findings demonstrate that with respect to the considered WAMS communication network effects LPM and HSVD are much more resilient with respect to the TKM and R-EMD. The ECKF behaviour has not be evaluated since already with an intact signal provides non-consistent estimations. The reasons which lead us to construct this sort of performance ranking are here synthesized:

March 2014

- LPM responds well to the different synthetic signals, polluted or not, provided in input thanks to the inherent robustness offered by the combination of the  $L_p$  periodogram and the tailored damping estimation procedure. Either the periodogram or the linear regression techniques is weakly affected by the noise and data packet dropouts presence in the fed signals;
- HSVD-VARPRO takes as the good characterizes the TKM in all the investigated cases, exactly the frequency estimation, employing a resilient techniques to calculate the damping coefficient which is the particular non linear least squares algorithm VARPRO. The latter is not perturbed either by high noise levels nor by substantial loss of data;
- TKM is able to face with the investigated communication network issues by increasing the Hankel matrix size. Nonetheless, while the perturbations in the backward prediction vector induced by the noise are quite limited, the ones associated to the data packets dropouts yield damping coefficient estimations sometimes really different from the actual ones. This is due to the overlap of the signal and noise subspaces which makes hard the correct estimation of the modal parameters;
- R-EMD suffers from the employment of the FFT for constructing the masking signals. When the signal is damped, the Fourier peaks can slightly differ from the actual ones e this can make the masking ineffective. Besides the noise and data packet dropouts could produce an increase of the IMF number with frequency and damping coefficient coherent with the ordinary ones so making hard their exclusion from the targeted ones.

## 5.2 Kundur's two area test system

The Kundur's two area four machine test system is the most classical IEEE test bench for investigating the electromechanical small signal stability of interconnected power systems. In spite of its small size, such a system is able to replicate in detail what actually happens in a real interconnected power system. As illustrated in Fig. 5.10 the system consists of two fully symmetrical areas linked together by two 230 kV lines of 220 km length. Each area is equipped with two almost identical synchronous machines. The load, modelled as a constant impedance, is shared by the two areas in such a way that area 1 is exporting 413 MW to the area 2. The mentioned active power transfer, is about three times the single line surge impedance loading thus confirming an operating condition somewhat stressed, even in steady-state. All the information needed for the simulation, exactly bus data, line data, machine data prime mover and exciter system data are reported in [94], [95].

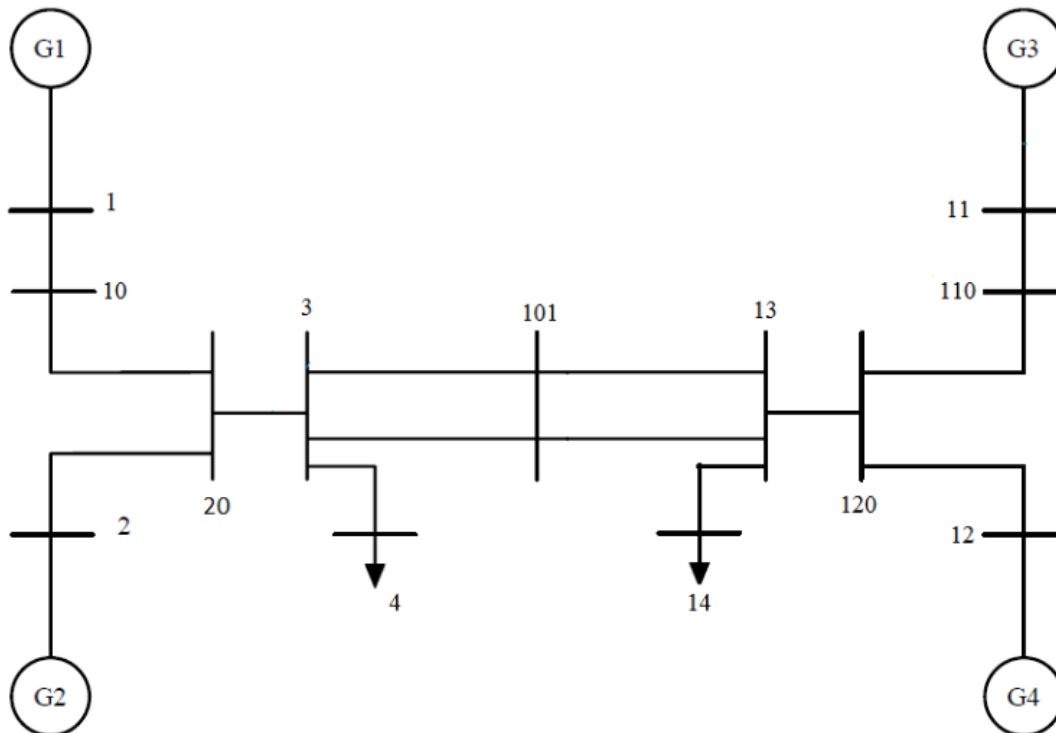


Fig. 5.10 – Kundur's two area test system

To identify the system electromechanical dynamic the modal analysis has been performed by using Power System Toolbox [96]. By computing the eigenvalues

of the state matrix **A** three chief electromechanical modes can be detected that are listed in Tab. 5.4 in terms of characteristic frequency and damping ratio  $\xi$ .

TAB. 5.4 – MODAL ANALYSIS MAIN OUTCOMES - TWO AREA TEST SYSTEM

Modes number	Eigenvalue $\lambda$	Damping Ratio $\zeta$	Frequency f [Hz]
1	0.1046 + i4.0407	- 2.59	0.6431
2	- 0.5648 + i7.0453	8.00	1.1213
3	- 0.5850 + i7.2954	7.99	1.1611

As can be noted the first electromechanical mode, Mode 1, is an unstable inter-area mode between the two area, as confirmed by the negative value of damping ratio. Mode 2 and Mode 3 respectively represent a local mode between G1 and G2 and a local mode between G3 and G4. A pictorial representation of the dynamic matrix eigenvalues in the frequency-damping ratio plane is shown in Fig. 5.11.

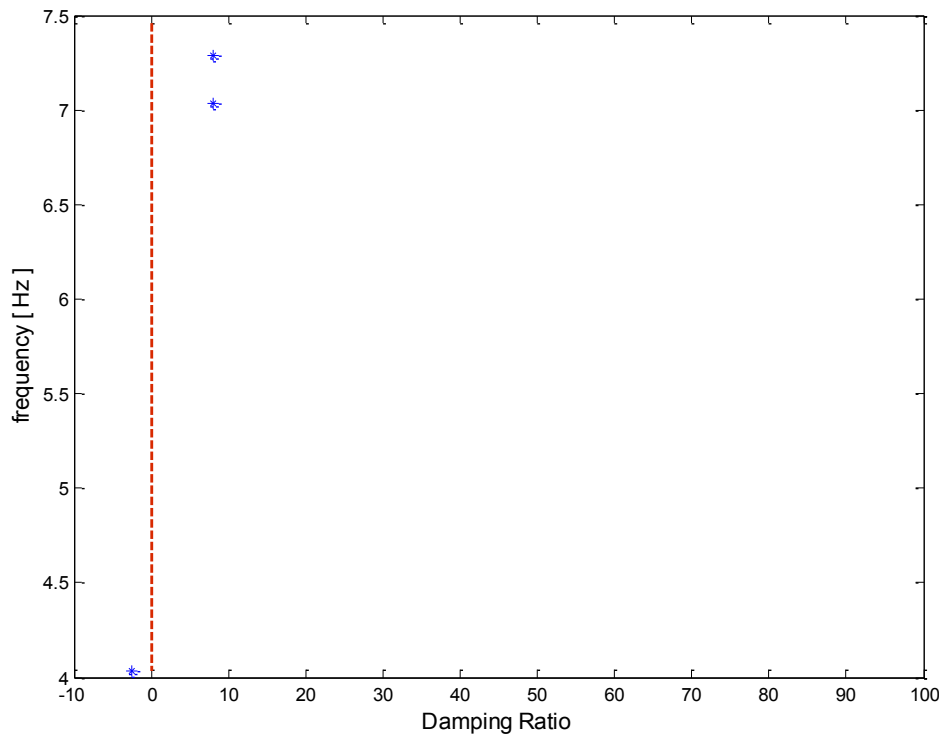


Fig. 5.11– Eigenvalues disposal: two area test system.

To test the ability of an estimation algorithm in calculating the characteristic parameters of the mentioned electromechanical oscillations there is the need to acquire signals related to the power system operating. This has been accomplished by performing a dynamic simulation of the system open-loop response (PSS action is excluded) to a 5% magnitude pulse, applied for 12 cycles at the voltage reference of M1. The instability phenomenon onset can be easily captured in all the system variables which show undamped oscillations. At this stage, for sake of brevity, we will focus only on the Mode 1 estimation which can be easily monitored by acquiring the active power transfer between the two areas. Fig. 5.12 illustrates the active power transmitted from the area 1 to the area 2 during the simulation.

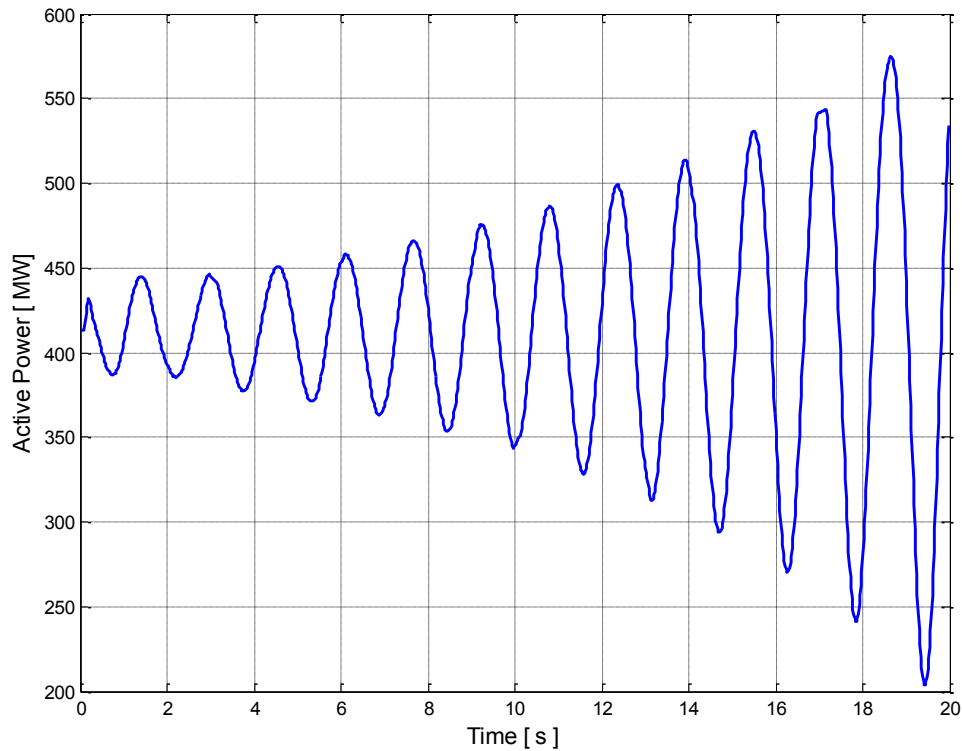


Fig. 5.12 – Active power between the areas : two area test system.

All the estimation algorithms described in the Chapter 3 and the one developed by us, LPM, are now used for basically estimating frequency and damping coefficient of the inter-area mode. Being the Mode 1 mono-component the standard Hilbert Huang Transform is employed for its tracking. The numerical outcomes are reported in the Table that follows.

TAB. 5.5 – ESTIMATION ALGORITHMS OUTCOMES - TWO AREA TEST SYSTEM

TKM		HSVD-VARPRO		ECKF		HHT		LPM	
$\sigma$ [s <sup>-1</sup> ]	f [Hz]								
0.0654	0.6426	0.1106	0.6425	0.0858	0.6563	0.1016	0.6573	0.1103	0.6398

As can be noted from the obtained numerical outcomes all the considered algorithms appear aligned both in frequency and damping estimation. ECKF and HHT seem to overestimate the inter-area oscillation frequency. In terms of damping estimation instead, the above estimation algorithms together with the LPM provide estimations closer to the actual ones. It appears clear that the presented results are related to a certain algorithms tuning.

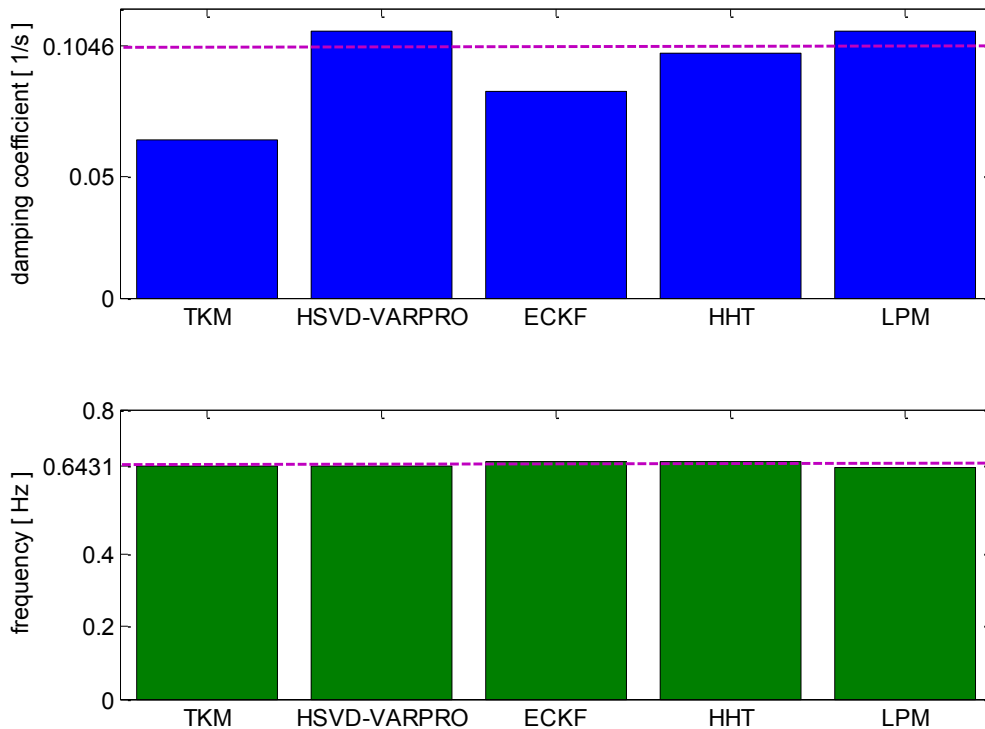


Fig. 5.13 – Estimation accuracy bar graph : two area test system.

As should be clear from the Chapter 3, all the estimation algorithms present some parameters on which one can act for adjusting the response. The experimental findings in Fig. 5.13 are hence derived with a certain tuning. Now,

in order to ensure higher accuracy in damping estimation the Hankel matrix size in TKM algorithm is iteratively increased from  $L=10$  (value assigned in the previous simulation) to  $L=55$  (value at which the estimated damping coefficient is equal to  $\sigma = 0.1046 \text{ s}^{-1}$ ). Obviously this implies an increase of the algorithm computational burden although, even in this case, the criterion for distinguishing the actual inter-area mode from the fictitious ones yielded by the Hankel matrix size increase is successful.

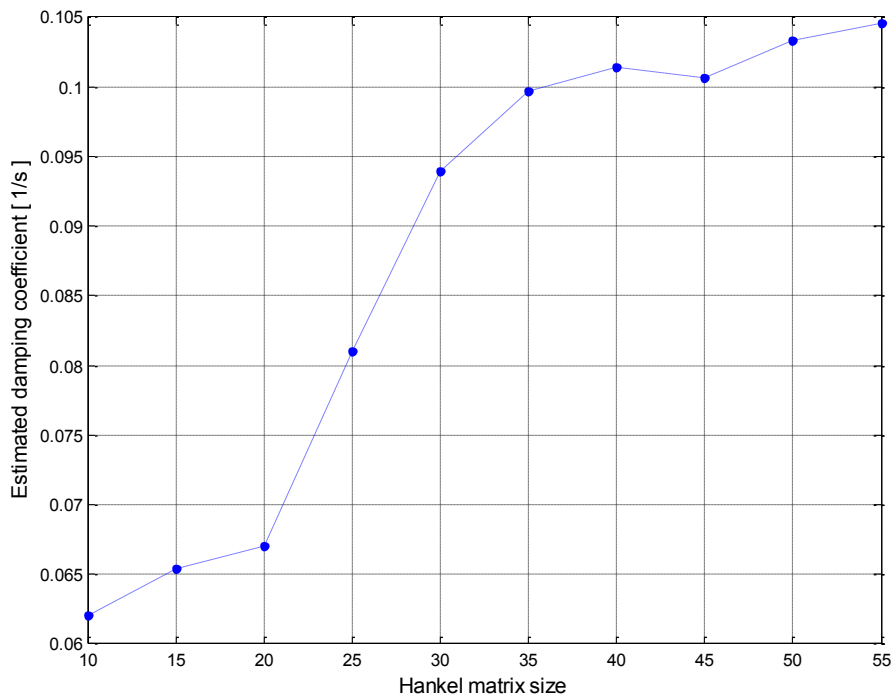


Fig. 5.14 – Estimated damping coefficient vs Hankel matrix size  $L$  : Tufts Kumaresan algorithm.

Hankel Singular Value Decomposition – VARIable PROjection method (HSVD-VARPRO) performs rather well as confirmed by the active power signal reconstruction made by successively computing inter-area oscillation amplitude  $A$  and phase  $\phi$  according to the Eqns (3.59)-(3.60). The signal reconstruction is depicted in Fig. 5.15 whereas the original signal in Fig. 5.12 has been detrended.

March 2014

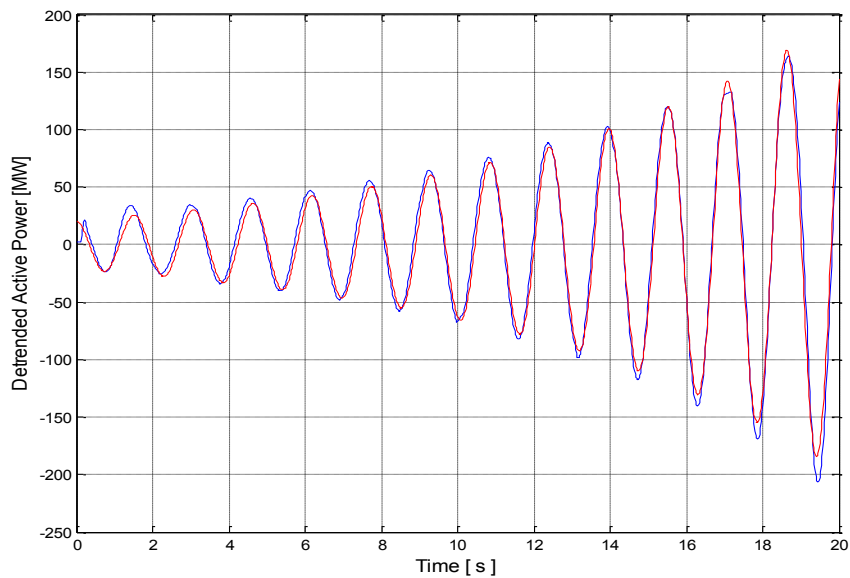


Fig. 5.15 – Signal reconstruction : Hankel Singular Value Decomposition – VARIABLE PROjection.

Conversely to the other estimation algorithms, with the exception of the HHT, ECKF estimates a time varying value for frequency and damping coefficient. This implies to average the achieved instantaneous frequency/damping values along the entire observation vector or however on an its convenient internal interval for providing an unique meaningful estimate.

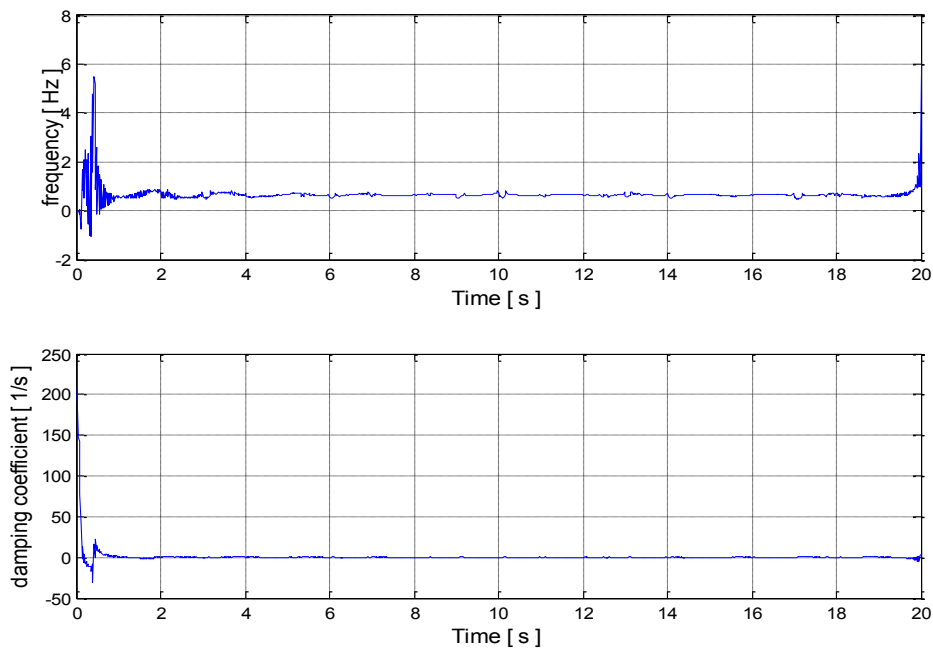


Fig. 5.16 – Time-varying frequency and damping coefficient: Extended Complex Kalman Filter.

Fig. 5.16 points out what just stated by depicting the filter output; a convenient interval on which average the parameters could be the one from 2 to 18, s so reducing the instability effects at the window's ends and hence enhancing the ECKF estimation accuracy. This operation is an expedients which can be categorized among the algorithms tuning mentioned above. As far as the HHT is concerned, the Empirical Mode Decomposition is able to extract the dominant component as first IMF. The remaining ones, jointly depicted with the latter and the residue in Fig. 5.17 are spurious component caused by the decomposition procedure to neglect realistically due to the lower characteristic energy and not meaningful values of the characteristic parameters.

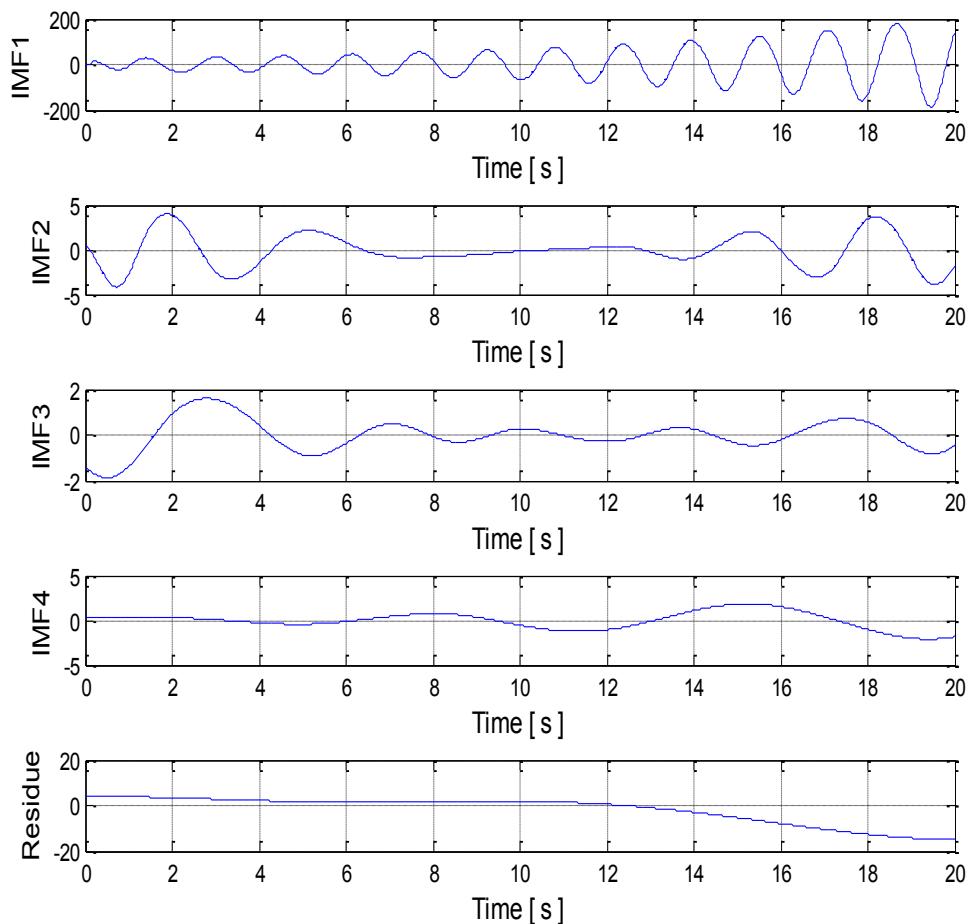


Fig. 5.17 – Empirical Mode Decomposition output: two area test system.

LPM application requires the preliminary  $L_p$  periodogram performing whose portrait for  $p = 1.5$  is shown in Figure 5.18 together with the ordinary periodogram. In this case, since there is only one component at frequency  $f_1 = 0.6423$  Hz, the unique bisecting frequency  $\omega_b$  can be computed by imaging another periodogram peak located anywhere (e.g.  $f_2 = 1$  Hz). In this manner the bisecting frequency will be  $\omega_b = \pi (f_1 + f_2)$ .

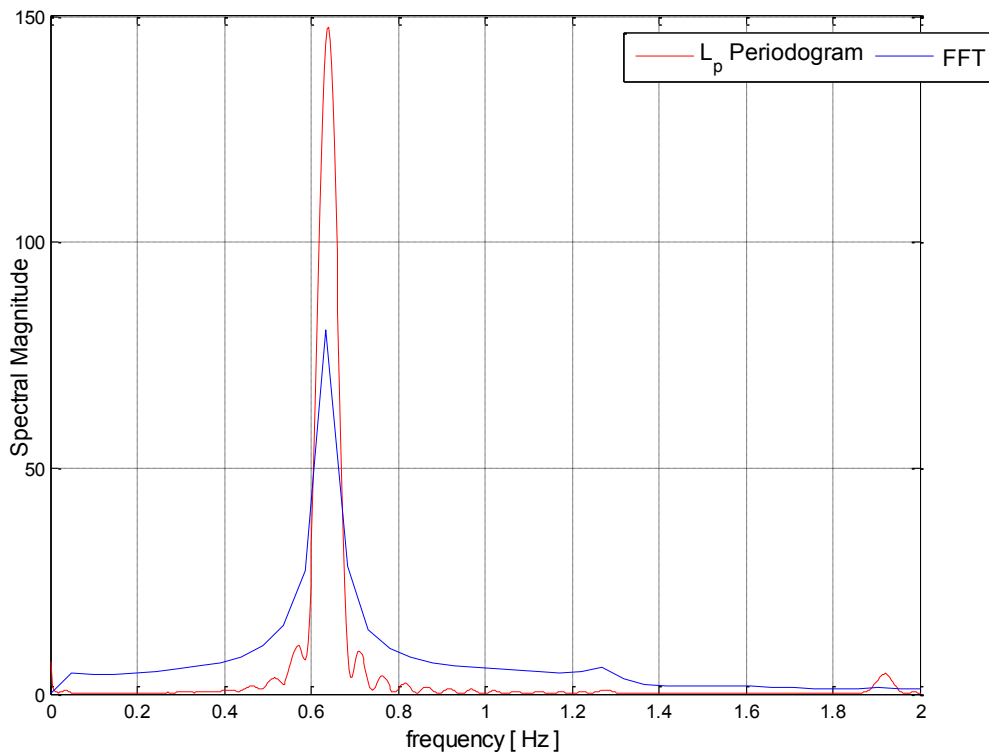


Fig. 5.18 -  $L_p$  Periodogram vs FFT : two area test system.

For sake of brevity, the time behaviour of the extracted component is now not reported since just one component is present in the observed signal. On the contrary, it is interesting to show the manner to reach damping coefficient: from the time behaviour of the component decaying amplitude (which is the logarithm of the instantaneous amplitude) versus the time a straight lines can be traced. The slope of the straight line exactly measures the average damping coefficient. One should be note that, similarly to the ECKF, an expedient is adopted for furnishing only one value of the inter-area damping coefficient. Actually, being the amplitude time-varying, instead of calculating a numerical derivative and then averaged the obtained values the numerical derivative is directly evaluated through the slope of the decaying amplitude. A pictorial

March 2014

representation of this calculation method is reported in Fig. 5.19 with reference to the Kundur's inter-area mode.

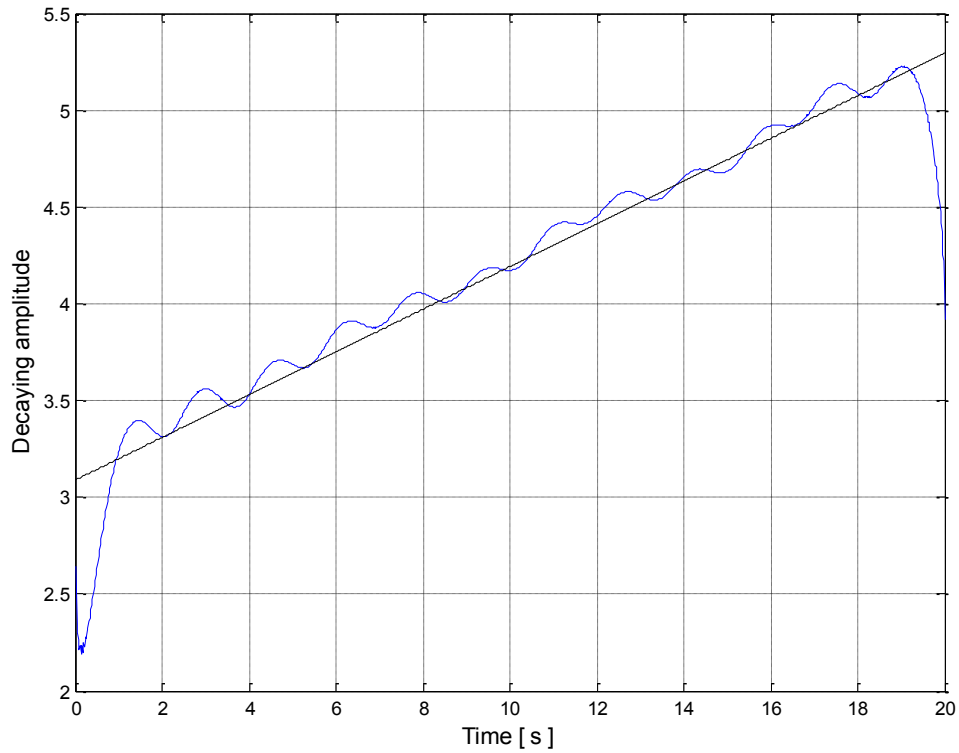


Fig. 5.19 – Damping coefficient estimation through linear regression procedure : two area test system.

### 5.3 IEEE 9 bus test system

The present case study refers to a basic version of the IEEE 9 bus-3 machines test system which represents a portion of the Western System Coordinating Council (WSCC) 3-Machines 9-Bus system.

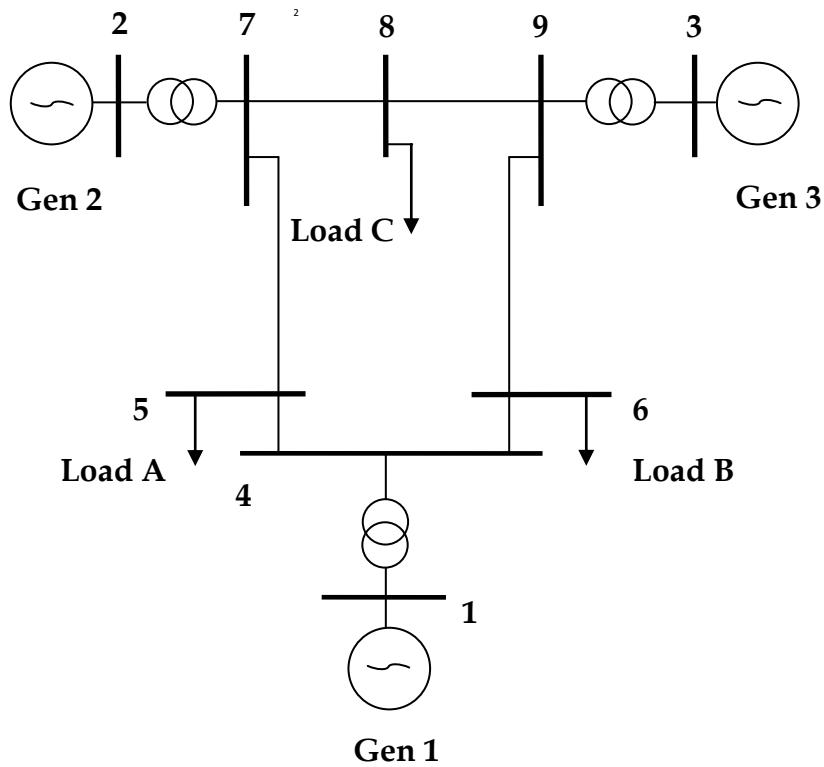


Fig. 5.20 – IEEE 9 bus test system

The test network consists out of three generators modelled by a sub-transient generator model powering three concentrated load at the buses 5, 6 and 8. More specifically, while load B and C are modelled as conventional constant impedance, load A is assumed to be a controllable one, 50/50 constant power-constant impedance. Detailed data for simulation can be found in [97]. Small signal stability analysis has been performed on the test network providing the outcomes, in terms of chief eigenvalues of the system dynamic matrix and in terms of corresponding damping coefficients and frequencies, reported in the Tab. 5.6.

TAB. 5.6 – MODAL ANALYSIS MAIN OUTCOMES – IEEE 9 BUS TEST SYSTEM

Mode number	Eigenvalue $\lambda$	Damping Ratio $\zeta$	Frequency $f$ [Hz]
1	-0.3216+i8.6088	3.7	1.3698
2	-0.9394+j13.0548	7.2	2.0777

The nature of electromechanical modes is evident if one considers the network structure: it deals with local oscillations among the machines as furthermore demonstrated by the frequency values reported in the Table above. Rigorously speaking, the nature of each mode should be evaluated by analyzing the corresponding eigenvectors. Figures 5.21a and 5.21b confirm as already said through a pictorial representation of the eigenvectors associated to the rotor angle terms. As it can be noted, Mode 1 represents a local oscillation between the machine 1 against the set of machines 2 and 3, whereas Mode 2 refers to a local oscillation of the set of machines 1 and 2 against the machine 3 (an angle of almost 180 degrees exists between the mentioned clusters for both the modes).

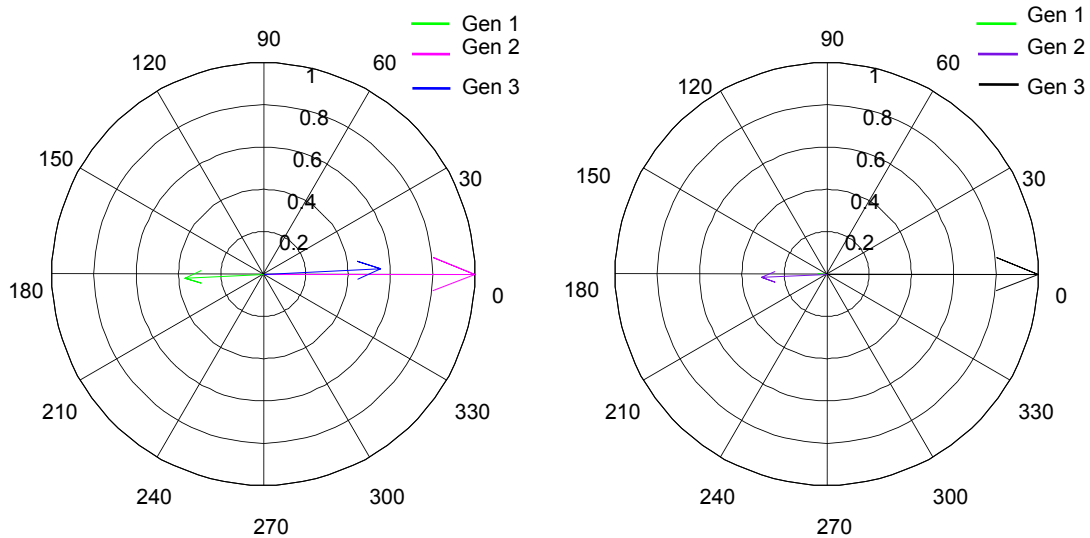


Fig. 5.21–Compass plot of the eigenvectors associated to the rotor angle terms : a) Mode #1 - b) Mode #2.

Therefore, the outcomes provided by the small signal stability analysis, constitute an unambiguous reference for sake of comparison with the results obtained by the investigated methods. In order to do this, a time domain simulation has been performed on the test network with the aim of sampling the interest signals. The simulation allowed to collect several signals candidate to be used for the modal content estimation. More specifically, at the time instant  $t=0$  a 0.01 p.u. load reduction of the controllable Load A has been applied. Fig. 5.22 depicts the time behaviour of the relative angular velocity between the generator 1 and 3 acquired during the simulation.

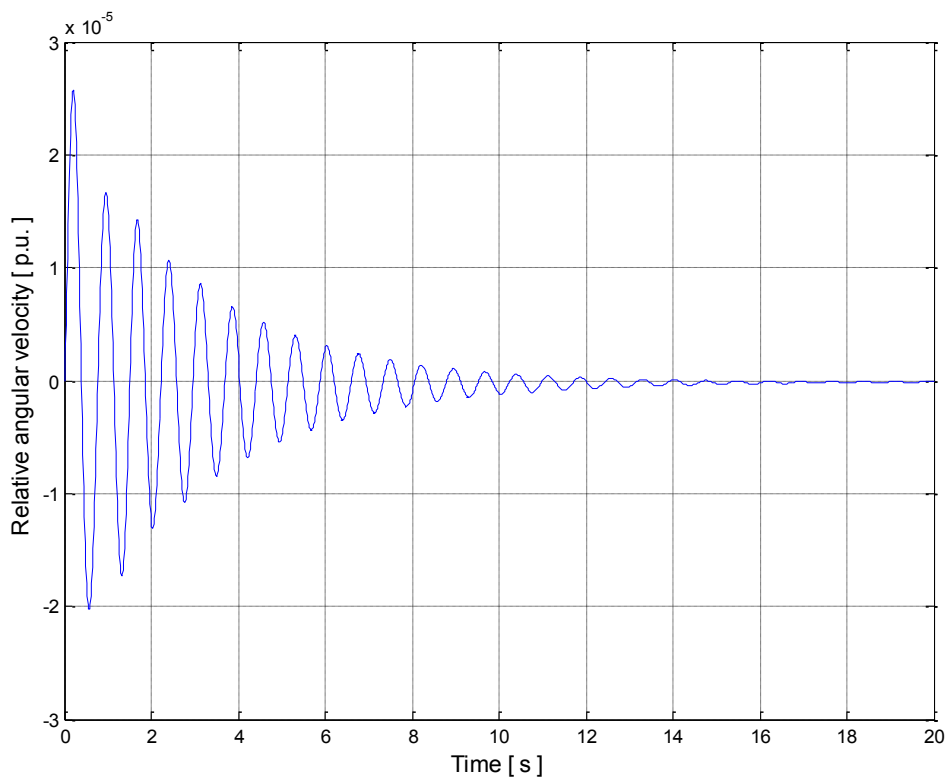


Fig. 5.22 – Relative angular speed between the generators 1 and 3 : IEEE 9 bus test system.

The estimation algorithms response are synthesized in Tab. 5.7.

TAB. 5.7 – ESTIMATION ALGORITHMS OUTCOMES – IEEE 9 BUS TEST SYSTEM

TKM		HSVD-VARPRO		ECKF		R-EMD		LPM	
$\sigma$ [s <sup>-1</sup> ]	f [Hz]								
-0.3398	1.3713	-0.3312	1.3712	-0.3038	1.3013	-0.2389	1.325	-0.3227	1.377
-1.0084	2.0991	-0.6776	1.0080	-0.9555	1.9986	-	-	-0.8929	2.072

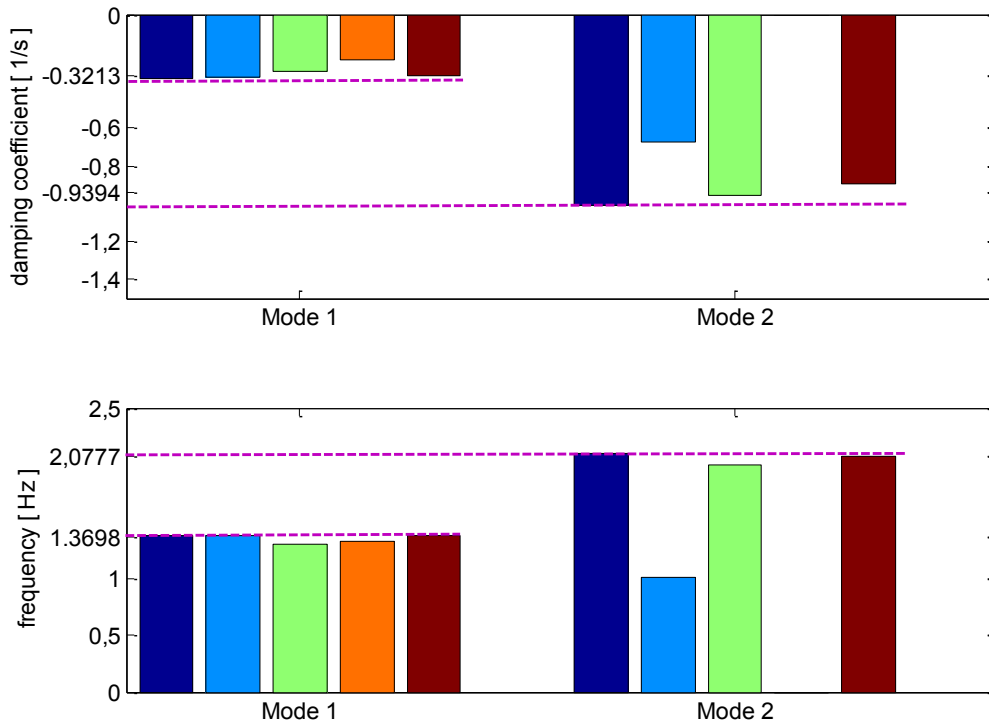


Fig. 5.23 – Estimation accuracy bar graph : IEEE 9 bus test system.

As can be argued, TKM is able to well detect both the modes by setting a Hankel matrix size  $L$  higher than the one adopted in the previous case study. Actually, the reported outcomes refer to  $L=30$ : an its reduction implies an accuracy loss. Consider that by setting  $L=10$  the Mode 2, which is characterized by lower energy, as confirmed by the Fourier spectrum in Fig. 5.24, is not identifiable. The issue just mentioned is a common problem for all the considered estimation algorithms. Actually, as can be noted by the Table 5.7 also the ECKF presents difficulties in evaluating the damping coefficient of the

Mode 2 with the initial tuning that involves a fitting with two sinusoids. By increasing the exponential damped sinusoids in the fitting function, the method estimation accuracy increases, as direct property of the Fourier transform. Essentially, the further fictitious sinusoidal components model the residue between the actual signal modal content and the fitting model. These components are hence characterized by frequency values external to the typical frequency range of the electromechanical oscillations (0.1-2 Hz) and sometimes damping levels meaningless. Fig. 5.25 illustrates the improvements in estimation accuracy with the increase of the number of damped sinusoids.

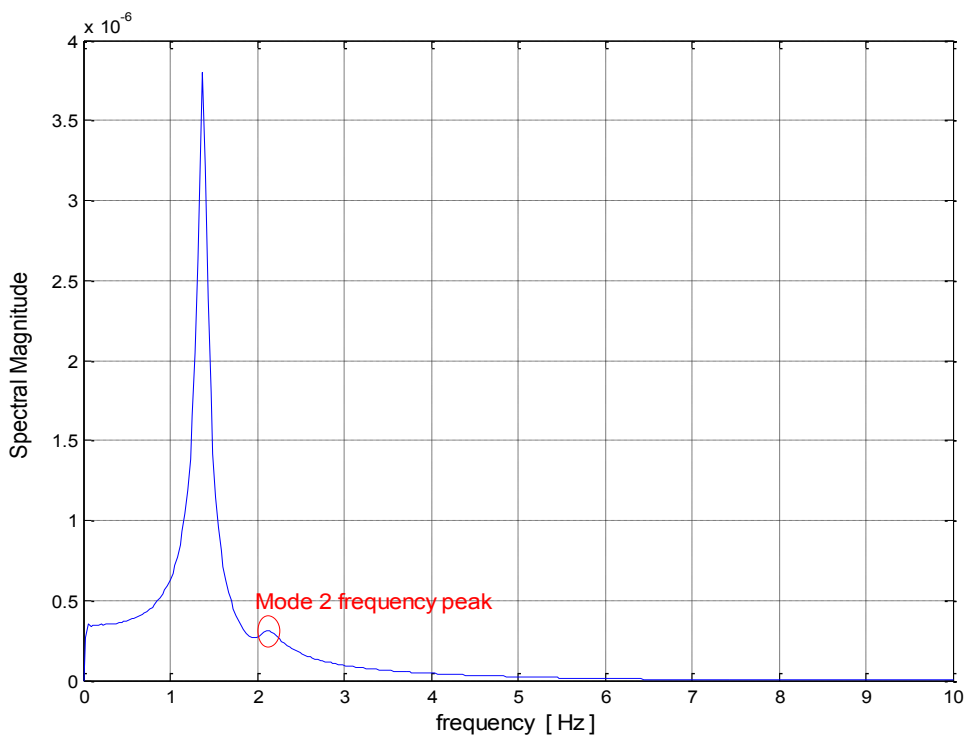


Fig. 5.24 – Fourier spectrum of the relative angular speed between the generators 1 and 3: IEEE 9 bus test system.

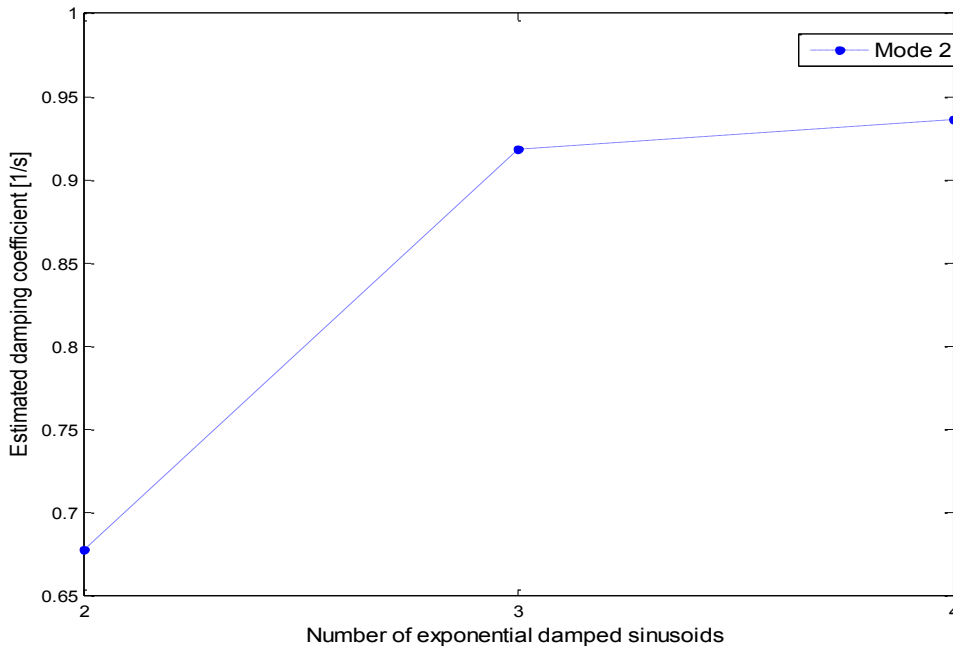


Fig. 5.25 – Estimated damping coefficient vs Exponential damped sinusoids number : Extended Complex Kalman Filter (Mode 2).

Standard HHT is not able to extract an IMF emulating the time-behaviour of the Mode 2, implying in this manner a reduction in the correct damping coefficient estimation. To overcome this issue the EMD with Fourier-Based Masking Technique, R-EMD, has been hence applied. Nonetheless, as depicted in Fig. 5.24, due to the difficulties in the peaks recognition, the revised masking procedure is altered so making ineffective the improvement. Furthermore, several difficulties were found in the proper choice of the parameter  $m$  in the masking function proposed in the EMD with Energy-Based Masking Technique, A-EMD. The LPM instead correctly identifies both the modes due to the ability of the  $L_p$  periodogram, in Fig. 5.26, to properly identify both the modes from the relative angular speed signal. Therefore the estimated frequency values are so determined. The damping coefficient, as before, are computed as linear regression line slope of the decaying amplitude of the Mode 1 and Mode 2 over a convenient interval. This is shown in Fig. 5.27 for both the modes.

March 2014

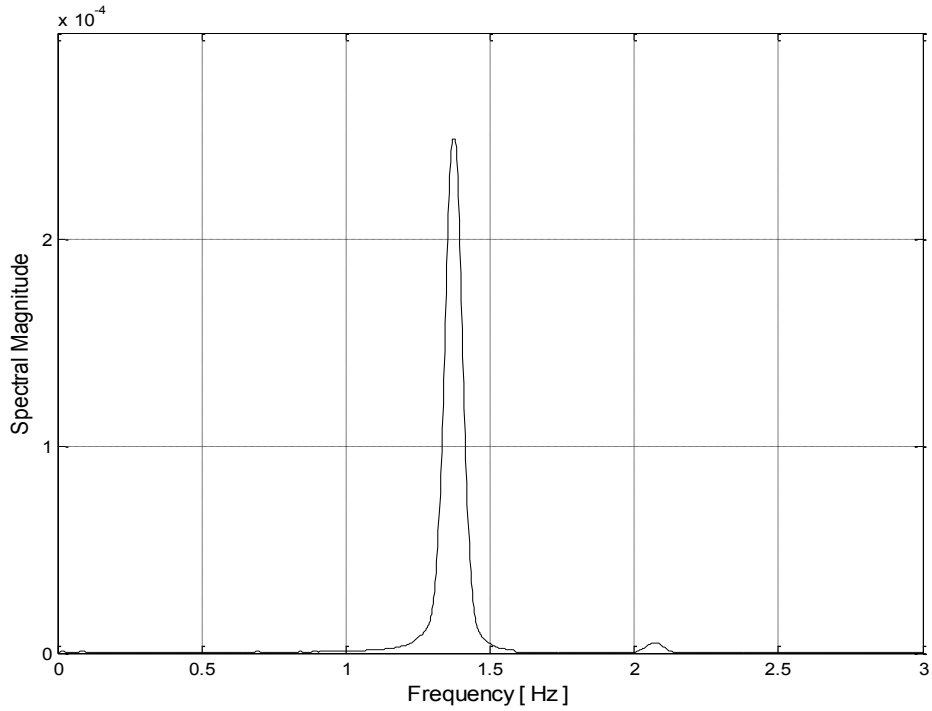


Fig. 5.26 –  $L_p$  periodogram of the relative angular speed between the generators 3 and 1: IEEE 9 bus test system.

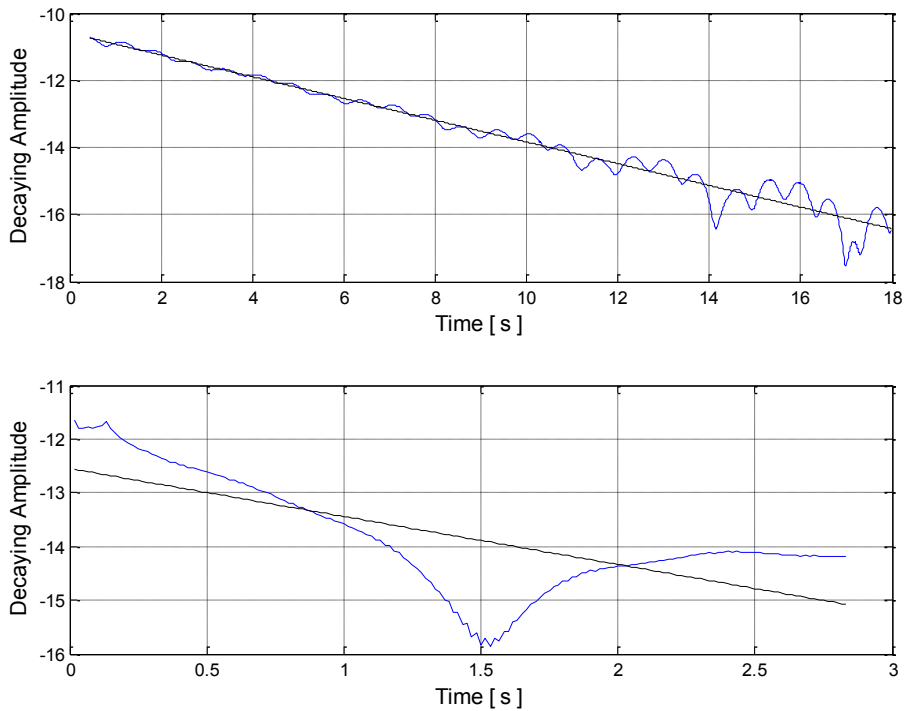


Fig. 5.27– Damping coefficient estimation through linear regression procedure : IEEE 9 bus test system.

## 5.4 IEEE 68 bus test system

To further investigate the effectiveness of the considered estimation techniques, a more complex and realistic power system, the 16-machine 68-bus test system, is here considered. This benchmark represents a reduced order model of the New England and New York interconnected system. All the information about the electrical system such as network data, generators modelling and their equipments typology (excitation systems, speed governors, power system stabilisers etc.), load modelling can be found in [98], [12].

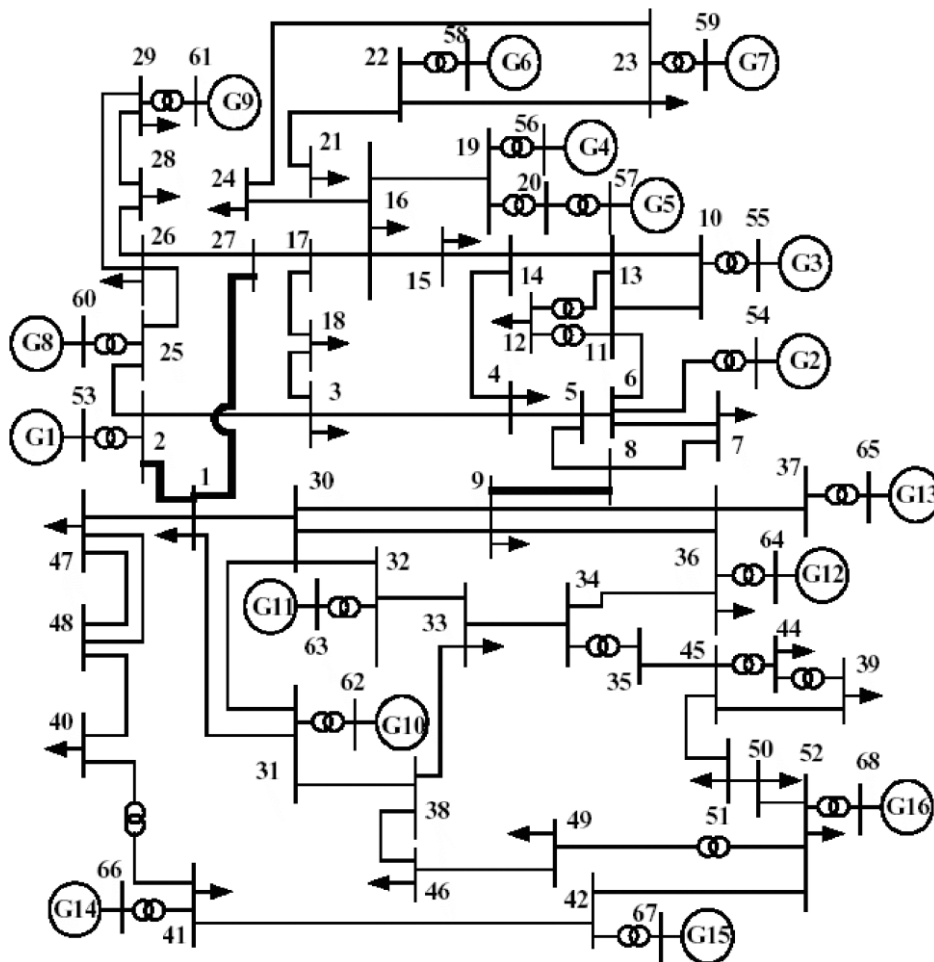


Fig. 5.28 –IEEE 68 bus test system

Modal analysis performed on the test network shows the presence of four inter-area mode whose fundamental characteristics are listed in the Table 5.8.

TAB. 5.8 – MODAL ANALYSIS MAIN OUTCOMES – IEEE 68 BUS TEST SYSTEM

Modes number	Eigenvalue $\lambda$	Damping Ratio $\zeta$	Frequency $f$ [Hz]
1	-0.3310+2.3494j	13.95	0.3739
2	-0.2926+j3.2786	8.89	0.5218
3	-0.5402+j4.1037	13.05	0.6531
4	-0.4303+j4.9864	8.60	0.7936

To excite the inherent inter-area oscillations network a three-phase fault has been applied on the tie line connecting the buses 46-49 at time instant  $t=0.1$  s which is subsequently cleared by the line protections in accordance with the ordinary fault clearing and reclosing times. The electrical service is hence restored. Different wide-area signal candidates for tracking the four inter-area modes have been selected and tested. Fig. 5.29 reports the time behaviour of the relative angular velocity between the generator 7 and 13 acquired over the dynamic simulation.

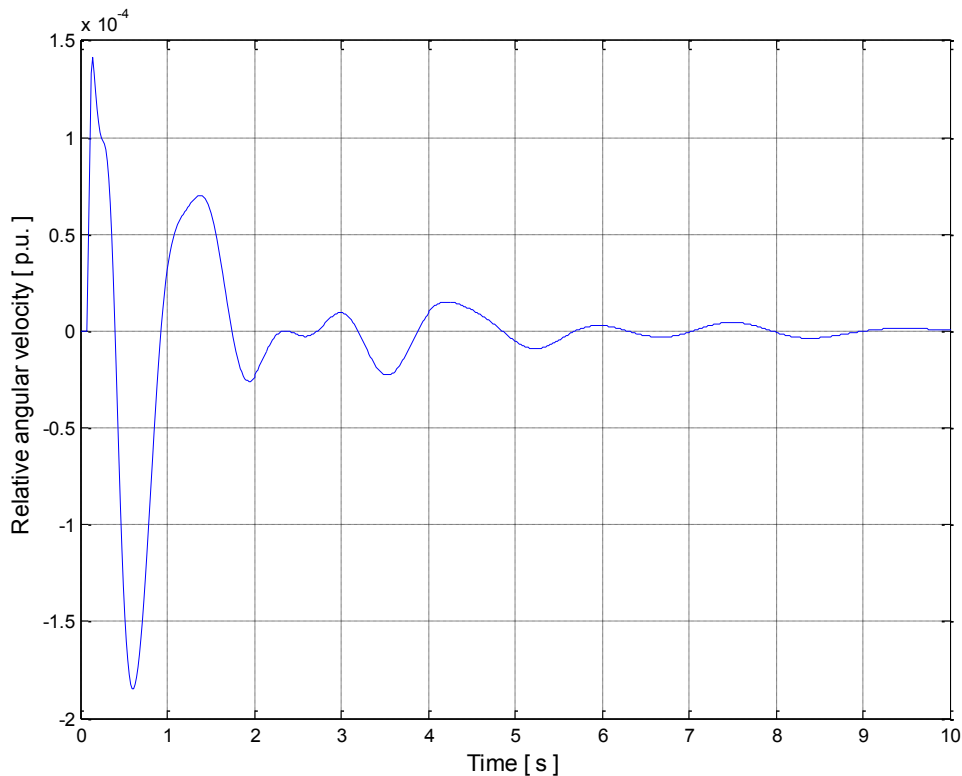


Fig. 5.29 – Relative angular speed between the generators 7 and 13: IEEE 68 bus test system.

March 2014

The numerical outcomes yielded by the investigated estimation algorithms are listed in Tab. 5.9. A proper digital filtering of the signal is needed in this case with respect to the previous ones analyzed in order to focus on the frequency interval of interest, which is very tight. By looking at the bar graph in Fig. 5.30 TKM is able to track all the inherent oscillatory modes estimating with sufficient accuracy both the frequencies and the damping coefficients. The Mode 4 damping coefficient estimation deviates from the actual one in a more sensible manner with respect to the others due to the filtering action. This value tends to increase towards the real one by shifting the high pass frequency of the band-pass filter. Unfortunately this operation implies an accuracy loss on the estimation of the other modes.

*TAB. 5.9 – ESTIMATION ALGORITHMS OUTCOMES – IEEE 68 BUS TEST SYSTEM*

TK		HSVD-VARPRO		ECKF		R-EMD		LPM	
$\sigma$ [s <sup>-1</sup> ]	f [Hz]								
-0.3443	0.3510	-0.4025	0.3510	-0.3460	0.3516	-0.1830	0.3375	-0.3423	0.3820
-0.3986	0.5760	-0.3880	0.5755	-0.4157	0.5698	-	-	-0.2830	0.5173
-0.4453	0.6785	-0.5083	0.6788	-0.5514	0.6507	-0.2717	0.6484	-0.5498	0.6552
-0.1735	0.7959	-0.2989	0.7960	-0.4565	0.7885	-0.1959	0.8128	-0.3423	0.7825

The performance of the HSVD-VARPRO and of the ECKF are essentially ensured by the proper tuning of the HSVD which has been able to provide in both the cases a good starting point for the iterative procedures. Without this tuning operation the effectiveness of the mentioned estimation algorithms could be threatened. Due to the presence of four frequency components in about the same octave the HHT was replaced with the R-EMD like in the previous case study. The Fourier spectrum of the observed processed signal is depicted in Fig. 5.31.

March 2014

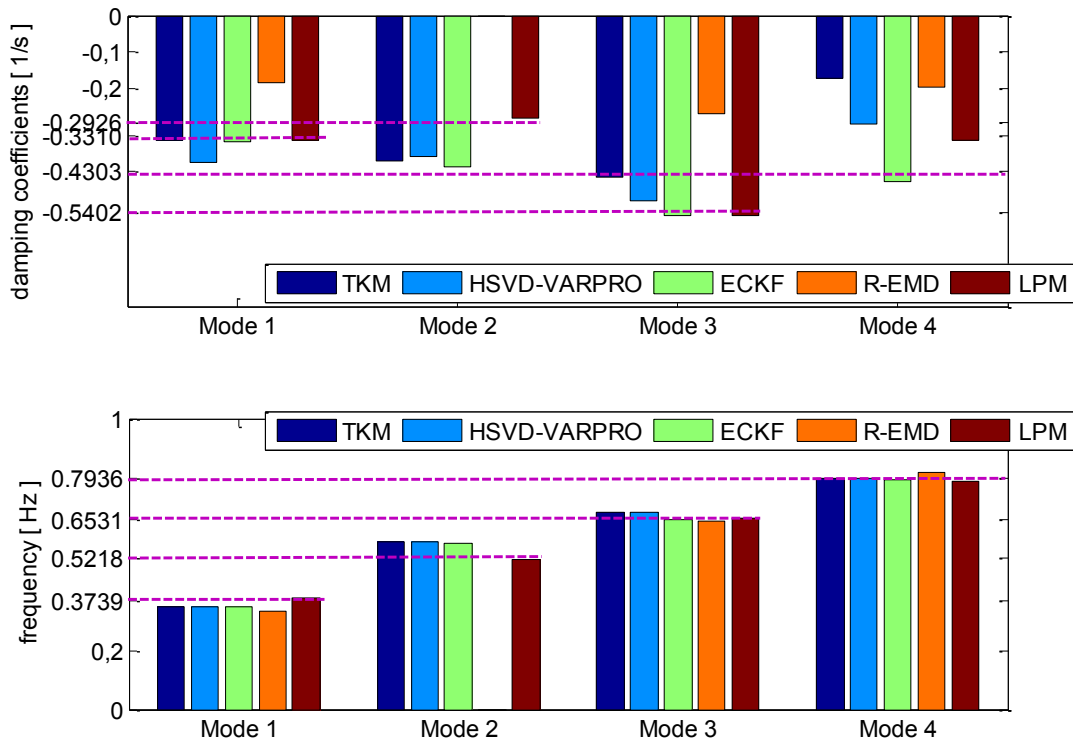


Fig. 5.30 – Estimation accuracy bar graph : IEEE 68 bus test system.

As can be noted the peak associated to the Mode 3 is not clearly identifiable so affecting, as in the previous case study, the effectiveness of the revised masking signal procedure. The singular fact that happens is that, thanks to the revised masking signal procedure, this mode is tracked losing detailing information about the dynamic evolution of the Mode 2. The frequencies estimation is satisfactory while the one of the damping coefficients suffers from the outlined issue. Conversely, the  $L_p$  periodogram is able to recognize all the frequency components making hence effective the decomposition according to the procedure HT-based. The frequency obtained by the  $L_p$  periodogram and the damping coefficient, computed from the regression line procedure applied to each elemental component decaying amplitude, are the closer to the one provided by the modal analysis.

March 2014

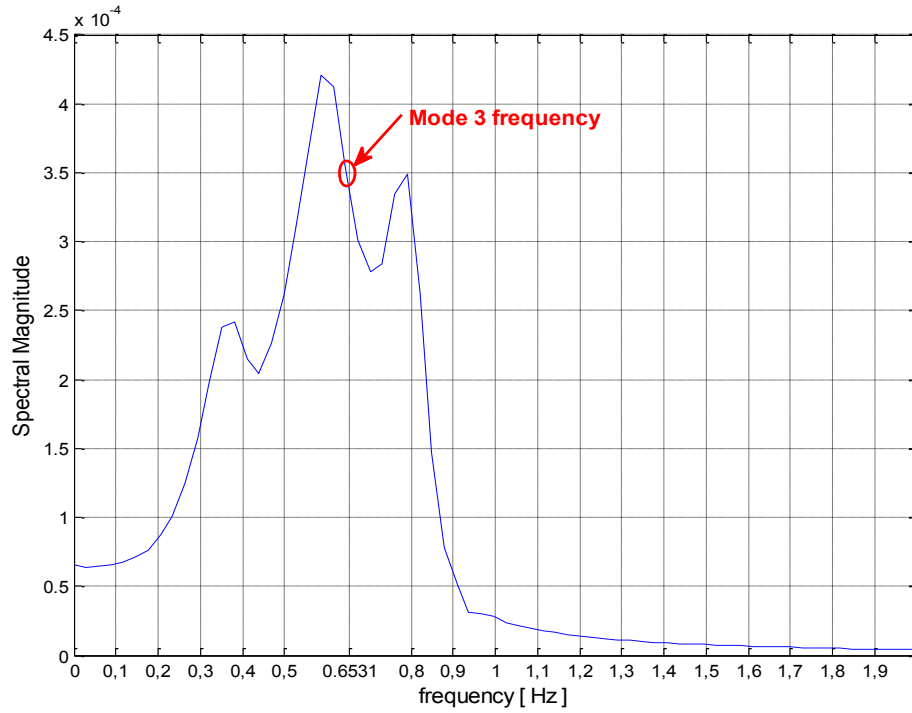


Fig. 5.31 – FFT of the relative angular speed between the generators 7 and 13: : IEEE 68 bus test system.

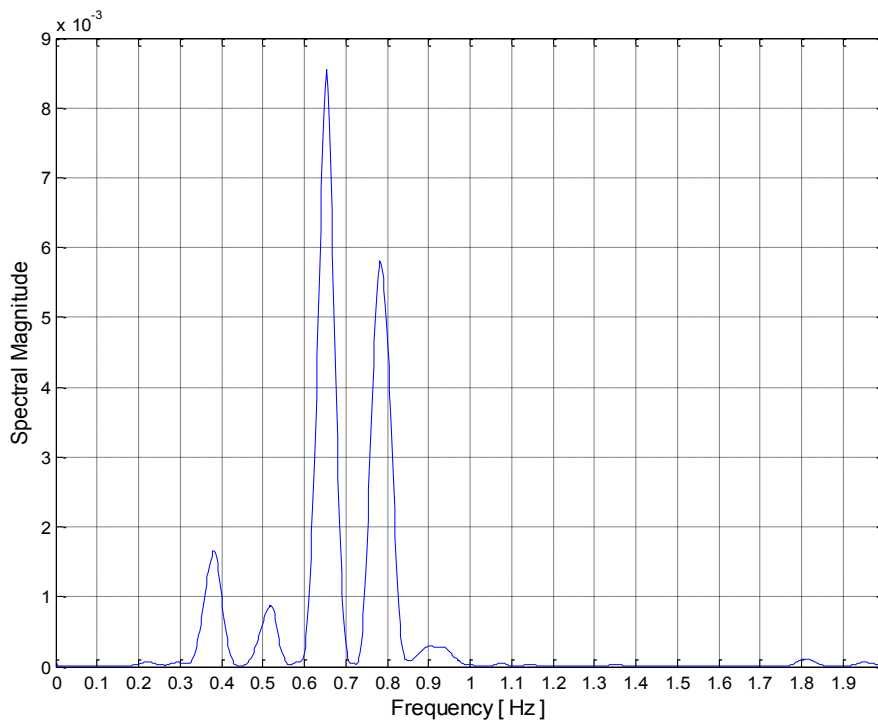


Fig. 5.32 –  $L_p$  periodogram of the relative angular speed between the generators 7 and 13 : IEEE 68 bus test system.

## 5.5 Real electromechanical oscillations in ENTSO-e interconnected network system grid

ENTSO-e Continental European Synchronous Area is a large interconnected electrical system which spans from Portugal to the West, Denmark to the North, Italy in the South and Greece in the East. The inherent oscillatory modes are both local and inter-area. With the Turkish power grid connection to the ENTSO-e CESA system, from September 2010, three major inter-area modes can be identified [99]:

- The **East-West mode** appeared following the Turkey connection, characterized under normal conditions by the major energy. It involves coherent movement of generators in Portugal and Spain against those in Turkey. This mode exhibits a typical frequency of 0.13-0.15 Hz and a time-domain damping  $\xi_{td}$ , calculated as the ratio of two successive peaks in a recorded oscillation, in the interval 45-70%.
- The **Former East-West mode** engages coherent movement of generators in Portugal and Spain against those in Greece. The typical frequency falls in the interval 0.17-0.2 Hz while the time-domain damping  $\xi_{td}$  around 40-50%. Such a mode is clearly observable through frequency measurements from Greece and Portugal.
- The **North-South mode** involves coherent movement of generators located in the south of Italy against the ones installed in the north of Germany and Denmark. The typical frequency falls in the interval 0.23-0.27 Hz whereas the recorded time-domain damping  $\xi_{td}$  is around 30% on average. Good measurement signals to track this mode are frequency and voltage angle measurements from southern Italy or Denmark, or active power flow measurements on the cross-border lines between Italy and Switzerland.

Therefore the analytical studies of engineers and researchers about the dynamic behaviour of this massive electrical power system are supported by several distributed measurement resources located in the whole ENTSO-e CESA.

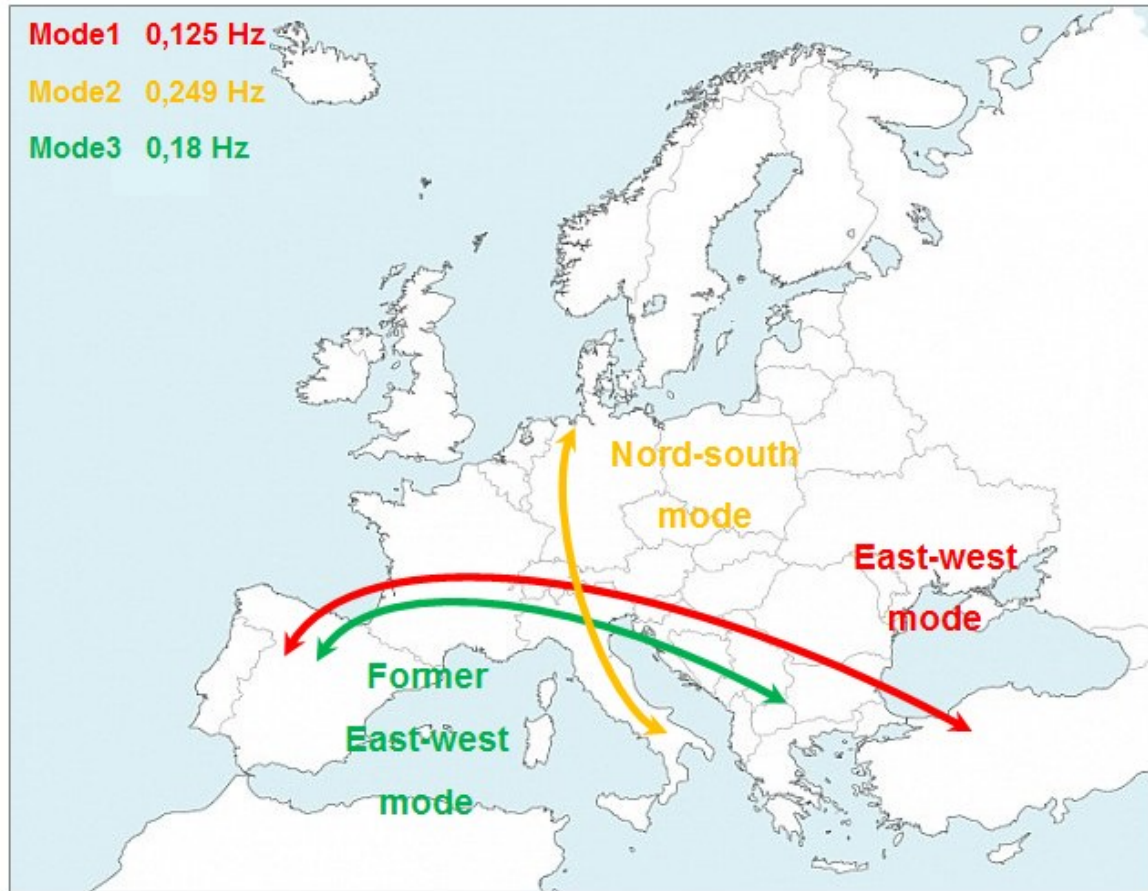


Fig. 5.33 – ENTSO-e CESA inter-area modes

### 5.5.1 A sudden inter-area oscillation recorded in the Continental Europe on 19<sup>th</sup> February 2011

On February 19<sup>th</sup> 2011 (a Saturday) at the 08:00:00 UTC (Coordinated Universal Time) inter-area oscillations within the Continental Europe power system occurred. The highest impact of these 0.25 Hz oscillations was observed in the middle-south part of the system with amplitudes of +/- 100 mHz in southern Italy and related power oscillations on several north-south corridor lines of up to +/- 150 MW and with resulting voltage oscillation on the 400 kV system of +/- 5 kV respectively. Fig. 5.34 depicts the frequency oscillations recorded at Brindisi along a time window of about five minutes. Indeed the total duration of the oscillations was around 15 minutes: the complete time-behaviour is illustrated together with the frequency oscillations recorded at Mettlen in Switzerland and at Kassoe in Denmark in [100]. Therefore, along the North-

South axis the highest amplitude was recorded in the southern Italy, almost no oscillation was observed near the “nodal line” in Switzerland and at last much lower amplitude opposite oscillation was seen in Denmark.

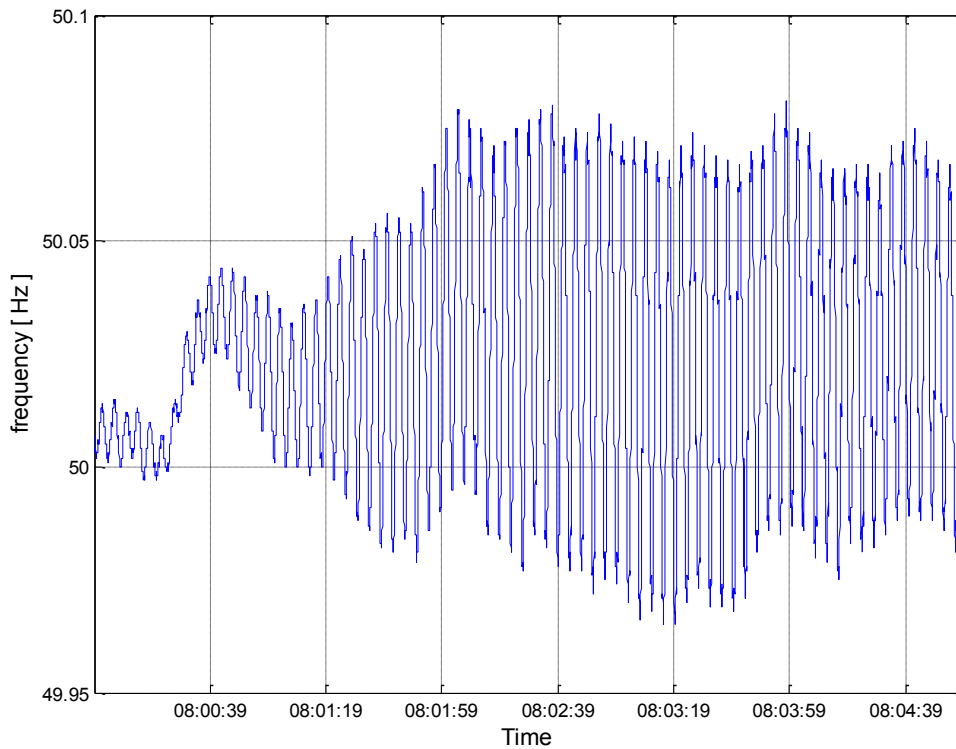


Fig. 5.34 – Frequency recorded at Brindisi (Italy) on February 19<sup>th</sup> 2011

All the estimation algorithms considered in this thesis detect the presence of one oscillatory mode which is exactly the ENTSO-e CESA North-South mode. The range in which frequency and damping coefficient fall has been reported in Section 5.5: for sake of uniformity with the previous case studies the time domain damping was converted in term of damping ratio getting a value of about  $\xi \sim 5-6\%$ . We prefer to continue the performance comparison by using the latter index instead than the damping coefficient as previously done. Actually a further conversion would furnish an approximated value due to the truncations and however one considers that  $\xi_{td}$  is an average value hence does not make sense to search for an advanced precision. The experimental findings provided by the algorithms on fifteen windows of 20 s are listed in Table 5.10.

Hence, some practical considerations about the behaviour of the considered algorithms with respect to an actual electromechanical oscillation can be

March 2014

extracted. Firstly, all the algorithms are able to properly identify a mode frequency falling within the mentioned range in almost all the analyzed observation windows related to the ringdown portion of the signal (after 08:00:30 UTC). As far as the ambient portion of the signal instead (before 08:00:30 UTC), HHT and TKM seem to do not correctly hang up the frequency value before the onset of the sudden frequency amplitude variation. It is conceivable that this is due to the transition from an operating regime to another and hence to a data typology (ambient type) to another one (ringdown). By looking at the damping ratio estimate one can note that ECKF output in the first time windows deviates from those ones of the other algorithms. Such a response is not due to a transient behaviour of the algorithm but instead to the fact that the portion of the data analyzed in the observation windows is ambient: ECKF, as already said, is specifically developed for light damped ringdown oscillations. On the basis of how just said we can state that this response was predictable. The next case study will further confirm that this kind of algorithm response implies a high variability in the filter state variables and hence in the provided estimations. All the remaining algorithms provide a damping ratio estimate consistent with each other from the fourth window onwards. Apart from the ECKF, the onset of the instability phenomenon is promptly well detected by all the considered estimation algorithms. This means that in this case almost all the studied algorithms would have been able to early detect the instability phenomenon and subsequently to permit to adopt all the necessary countermeasures.

Summarizing, the frequency oscillations recorded on February 19<sup>th</sup> 2011 pointed out that the Turkey connection has changed the mode displacement in ENTSO-e CESA. According to Terna investigations in fact in some measurement places there was a superposition of the East-West mode and North-South mode. Characteristic frequency and damping varied from a minimum low value to a maximum high value due to different composition of oscillations. Dispersed Generation (DG) such as wind or solar plants didn't play a negative role but however subtracted "stabilized inertia" from conventional groups equipped with PSS. The Italian power system currently plays the role covered in the past by other border areas like Spain, Portugal or exactly Turkey after the synchronization in the Central-East Europe: this means that it is more sensitive to the new oscillatory modes. For this reason, immediately after the event described, Terna has reinforced the PSS in Italy recommending to its ENTSO-e partners similar analysis in the rest of Continental Europe power system.

Real Time tracking of electromechanical oscillations in ENTSO-e Continental European Synchronous Area

March 2014

TAB. 5.10 – ESTIMATION ALGORITHMS OUTCOMES – ENTSO-e CESA NORTH SOUTH MODE a)

TKM		HSVD-VARPRO		ECKF		HHT		LPM	
$\xi$	f [Hz]	$\xi$	f [Hz]	$\xi$	f [Hz]	$\xi$	f [Hz]	$\xi$	f [Hz]
9.9075	0.4606	4.7454	0.4610	80.2002	0.1528	0.5352	0.3812	0.1734	0.2542
2.3844	0.2142	-11.9469	0.2140	41.1812	0.1506	-8.0654	0.2405	-10.4320	0.2446
4.7409	0.2339	0.4091	0.2340	10.4845	0.2351	1.4100	0.2434	-0.1745	0.2498
-0.9577	0.2456	-3.2189	0.2456	-1.3812	0.2385	-2.9873	0.2499	-3.0667	0.2530
-1.5565	0.2455	-2.0009	0.2455	-2.5632	0.2466	-2.5592	0.2495	-1.5745	0.2495
-1.0406	0.2414	-1.3620	0.2410	-3.6521	0.2432	-1.4242	0.2470	-1.1624	0.2538
-1.1735	0.2452	-1.3516	0.2455	-1.8934	0.2457	-1.3147	0.2481	-1.4354	0.2534
-0.3964	0.2459	-0.6552	0.2459	-1.7999	0.2457	-0.4552	0.2488	-0.9787	0.2533
-0.2839	0.2466	-0.3124	0.2461	0.2549	0.2464	-0.2309	0.2494	-0.0765	0.2538
-0.1779	0.2465	-0.1052	0.2464	0.4682	0.2465	-0.1407	0.2484	-0.2344	0.2546
-0.0899	0.2469	-0.1370	0.2468	-0.1296	0.2482	-0.2457	0.2480	-0.0109	0.2542
0.0029	0.2482	0.1169	0.2483	0.6678	0.2478	0.0826	0.2483	-0.1912	0.2541
0.2398	0.2476	0.1744	0.2477	0.2276	0.2478	0.1777	0.2481	-0.1411	0.2550
0.3907	0.2488	0.2322	0.2489	0.4495	0.2494	0.4211	0.2490	-0.1012	0.2545
0.1768	0.2475	0.2563	0.2475	0.9954	0.2474	0.4526	0.2483	-0.1015	0.2546

## 5.5.2 North-South inter-area mode excited by a fault occurrence in Italy

The current case study takes in consideration actual voltage magnitude measurements recorded at a primary substation placed in the South of Italy, in Palermo, and stored in the Italian WAMS database. A grid disturbance on the 400 kV system on January 18<sup>th</sup> 2008 at the 17:05:20 UTC resulted in the voltage magnitude variation illustrated in Fig. 5.35. The physical location of the measurement point makes again observable the same North-South inter-area mode, now excited by a local fault occurrence.

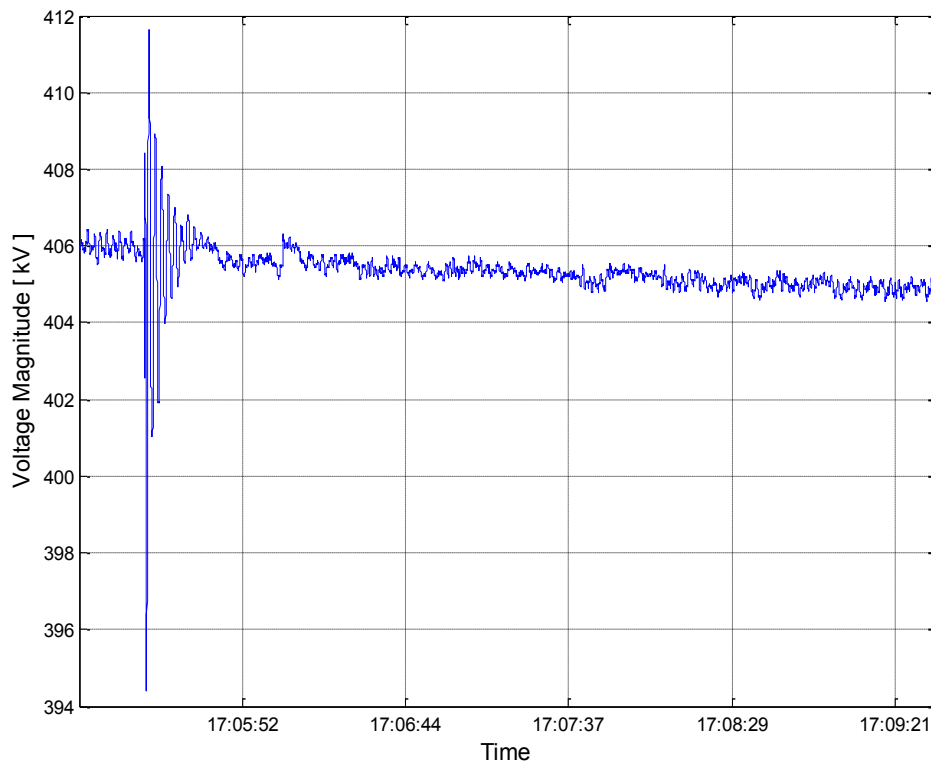


Fig. 5.35 –Voltage magnitude recorded at Palermo (Italy) on January 18<sup>th</sup> 2008

Since a substantial part of the signal is of ambient type this permits to complete the previous performance analysis with respect to the same inter-area oscillation.

Real Time tracking of electromechanical oscillations in ENTSO-e Continental European Synchronous Area

March 2014

TAB. 5.11 – ESTIMATION ALGORITHMS OUTCOMES – ENTSO-e CESA NORTH SOUTH MODE b)

TKM		HSVD-VARPRO		ECKF		HHT		LPM	
$\xi$	f [Hz]	$\xi$	f [Hz]	$\xi$	f [Hz]	$\xi$	f [Hz]	$\xi$	f [Hz]
-5.9122	0.2480	-6.0501	0.2480	-4.5545	0.1450	-8.1340	0.2501	-5.3310	0.2495
-4.3491	0.2510	-4.5119	0.2510	-7.8605	0.1384	-4.9698	0.2580	-4.1587	0.2540
1.3888	0.2516	0.6838	0.2516	2.0562	0.2353	0.8136	0.2509	0.8990	0.2490
2.8193	0.2506	2.8734	0.2506	6.7984	0.2385	3.7743	0.2477	2.8523	0.2492
3.1057	0.2494	3.0249	0.2494	5.7984	0.2466	3.3447	0.2473	2.8745	0.2501
3.0841	0.2502	3.1556	0.2502	7.6796	0.2432	4.5467	0.2471	3.1312	0.2490
-0.1032	0.2534	-0.6808	0.2534	-3.5871	0.2457	-0.7764	0.2534	-0.3166	0.2398
1.8238	0.2488	2.0895	0.2488	6.3703	0.2457	2.4031	0.2483	2.1973	0.2480
0.1685	0.2478	-0.2117	0.2478	-1.5478	0.2464	0.1637	0.2485	-0.1590	0.2504
4.7487	0.2542	10.4660	0.2542	24.2812	0.2465	3.9270	0.2777	7.7202	0.2589
-2.8609	0.2532	-3.6330	0.2532	-10.4350	0.2482	-4.4979	0.2563	-3.9453	0.2488
1.0190	0.2471	1.1820	0.2471	3.8086	0.2478	1.1331	0.2488	1.6255	0.2488
-0.9936	0.2464	-1.0841	0.2464	-2.2789	0.2478	-1.2624	0.2490	-0.6798	0.2474
0.5877	0.2513	0.8824	0.2513	2.4411	0.2494	1.1566	0.2499	1.1744	0.2495
2.7330	0.2441	3.4900	0.2441	8.7544	0.2474	5.7590	0.2476	4.6673	0.2399

Similarly to the previous case study, the mode frequency estimation is not a particular concern for all the employed algorithms as it can be argued by the Table 5.11 As far as the damping ratio estimation is concerned, the ECKF behaviour slightly deviates from the response of the other algorithms along all

March 2014

the observation windows. Besides, due to the same reasons exposed in the previous Section the algorithm output in terms of frequency is outside the ordinary frequency interval of the North-South mode. On the contrary the remaining algorithms outcomes follow the same trend along the entire signal duration resulting very close to each other, in some particular observation windows even almost coincidental. Since when the voltage magnitude oscillation vanishes, negative damping ratio estimates are provided by all the algorithms, in order to implement possible automatic countermeasures avoiding false alarms, such as generators' re-dispatching, tie line flows adjustments, load reductions, network topology changes etc, proper triggering criteria has to be defined. One proposal could be so conceptualized: (i) set a damping ratio threshold alarm value  $\xi_{th}$  and a maximum violation time  $t_{max}$ , (ii) if the damping ratio estimated by one or more algorithms falls below this value,  $\xi < \xi_{th}$ , put the system in alarm condition initiate a time counter  $t_c$ , (iii) restrict properly the observation window and repeat the estimation process with the current signal portion, (iv) if the current estimated damping ratio is over the threshold value,  $\xi > \xi_{th}$ , remove the system by the alarm condition else repeat iteratively the estimation process until  $t_c = t_{max}$  then implement the most adequate countermeasures. Roughly speaking, such a philosophy is to perform a network action if the damping ratio estimates persistently violate the condition  $\xi < \xi_{th}$  for a certain time  $t_{max}$ .

### 5.5.3 Sardinia local oscillations

The last case study is particularly interesting since concerns a non-linear and non-stationary multi components waveforms recorded on August, 13<sup>th</sup> 2007 (01:40:00 UTC) at Cagliari and Fiumesanto in Sardinia island (Italy). Four chief local electromechanical oscillations among the generators installed on the island network can be identified from the measurements in Fig. 5.37. Till now, the characteristic mode frequencies are well known,  $f_1=0.12$  Hz,  $f_2=0.64$  Hz,  $f_3=1.33$  Hz,  $f_4=1,40$  Hz, as for it lacks an adequate characterization of the characteristic damping levels.

March 2014

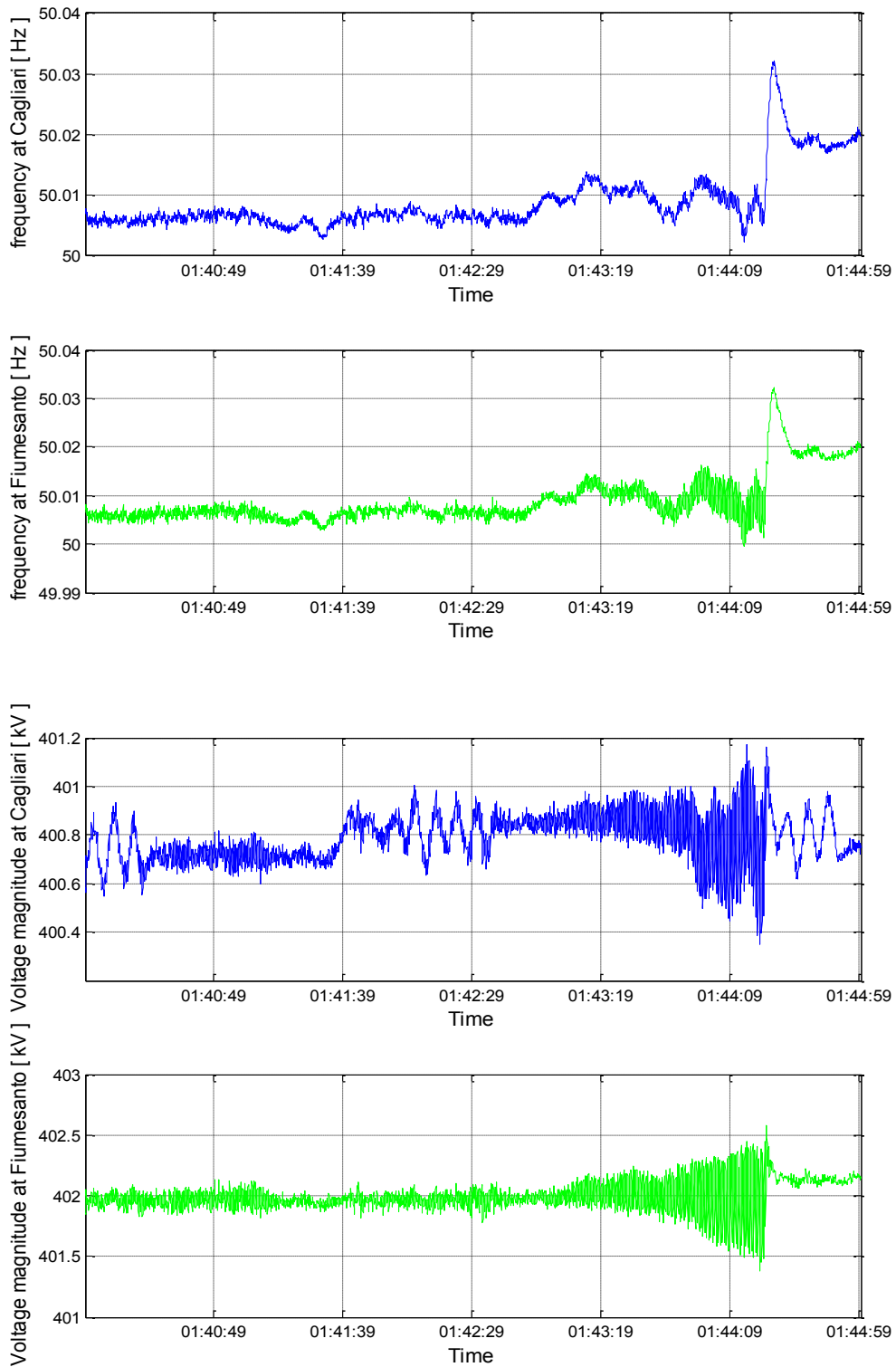


Fig. 5.36 – Waveforms recorded at Cagliari and Fiumesanto (Italy) on August 13<sup>th</sup> 2007

The signal Fourier spectrum in Fig. 5.37, estimating the stationary equivalents of the four time-varying frequency components allows to make two basic statements: 1) frequency component  $f_2$  is not well identifiable due to the low inherent mode energy 2) the two highest frequency components  $f_3$  and  $f_4$  falls within the same octave. The second aforementioned point is a particular concern for the EMD in HHT that fails in extracting mono-component IMF. To solve the mode mixing issue in the decomposition procedure, HHT algorithm has been replaced with the R-EMD that seems to overcome the EMD inability to guarantee the mono-component trait of each IMF. R-EMD decomposing capability has been compared with the one of the signal decomposition theorem HT based in LPM.

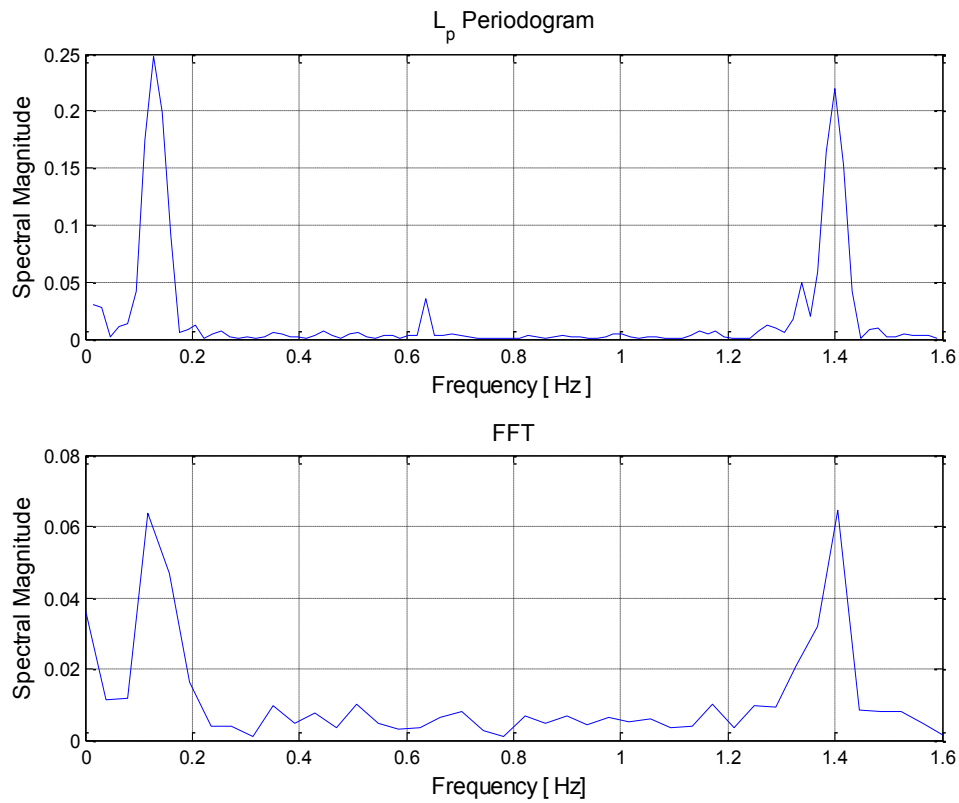


Fig. 5.37 – FFT vs  $L_p$  Periodogram on a 20 s time-window: voltage magnitude at Cagliari.

Table 5.12 collects the numerical outcomes obtained in this case study. The most important result achieved by the numerical simulations is the fact that the R-EMD fails in properly separating the local modes. Actually, as can be noted it seems to identify two IMF having similar frequency which try to emulate the modes at frequency  $f_3$  and  $f_4$ . This is essentially due to the FFT inability to

March 2014

correctly identify in each observation window all the inherent power system modes as shown in Fig. 5.38 for instance in one of the considered time window.

The two highest peaks of frequencies are superimposed making ineffective the R-EMD improvements in this specific case. Besides the heuristic parameters proposed by the developers are specifically derived for inter-area oscillation, this suggest the need for a revision in the case of local oscillations. In any case, no particular improvements were found by considering the alternative refinement, A-EMD. Conversely, the  $L_p$  periodogram (e.g.  $p = 1.5$ ) in LPM is able to well-capture all the inherent Sardinia island local modes separating quite sharply the modal content from the noise, especially in the middle part of the Fig. 5.37, as can be appreciated. Even more important is its ability to distinguish the two peaks at higher frequency falling in the same octave. These properties are preserved along the entire signal duration. Moreover the signal decomposition theorem based on HT of the LPM allows the waveform decomposition in elemental components whose frequencies match satisfactorily the ones provided by the  $L_p$  periodogram. In terms of frequency estimation, ECKF furnishes nearby outcomes to the ones of LPM. Unfortunately, apart the damping ratio estimates of the first mode the others provided by the FKE are realistically implausible; this is due to the highly variability in the filter state variables and hence in the damping calculation with respect to this particular test signal. To estimate the actual electromechanical modes damping ratio is not an easy task, and however it is not possible to provide a general measure at this stage. In any case, as can be noted, three algorithms on five furnish damping ratio estimates in a narrow band close to the zero value for all the modes, two of them are the R-EMD and the LPM. Therefore, one can reasonably imagine that the actual value of damping ratio falls within this tight band.

Real Time tracking of electromechanical oscillations in ENTSO-e Continental European Synchronous Area

March 2014

TAB. 5.12 – ESTIMATION ALGORITHMS OUTCOMES – SARDINIA LOCAL OSCILLATIONS, MODE 1

TKM		HSVD-VARPRO		ECKF		R-EMD		LPM	
$\xi$	f [Hz]	$\xi$	f [Hz]	$\xi$	f [Hz]	$\xi$	f [Hz]	$\xi$	f [Hz]
-0.2215	1.4111	0.4601	1.4010	0.6799	1.3987	-1.0605	1.1922	-0.5363	1.4105
5.2044	1.4645	23.9500	1.4304	-0.7363	1.4007	0.0889	1.2021	-0.4152	1.3997
5.0632	1.5658	24.1719	1.5421	-1.3812	1.4004	-0.6778	1.2005	-0.2499	1.4002
10.48	1.5131	20.3712	1.5022	0.4774	1.4010	0.9756	1.1995	0.7675	1.4008
0.8711	1.4706	23.9211	1.4780	2.1803	1.4003	0.0832	1.1784	0.3283	1.4001
2.5965	1.4631	5.2785	1.4594	0.1832	1.3995	-0.4679	1.1952	-0.1169	1.4010
1.6207	1.4635	-1.8099	1.4688	-0.4091	1.4007	-0.1027	1.2133	0.0991	1.4008
3.4273	1.4538	0.2094	1.4532	2.0555	1.3899	-1.0243	1.1995	-0.3565	1.4006
4.3522	1.5353	18.8005	1.5633	0.3692	1.4012	-0.2172	1.1396	-0.3543	1.4005
1.7949	0.2815	22.3143	0.8574	-1.9343	1.4015	-0.3705	1.2128	-0.5975	1.4007
11.4716	1.5661	23.9243	1.5493	4.5977	1.3685	-0.1965	1.2009	-0.2190	1.4004
7.5055	1.4657	-13.8628	1.4576	4.6156	1.3996	-0.3555	1.2063	0.1688	1.4083
10.3221	1.5449	24.7265	1.5693	1.7244	1.2990	-0.0336	1.1705	0.2384	1.4012
4.1112	1.4421	5.4735	1.4567	35.1005	1.3556	3.9205	1.1178	1.7005	1.3899
0.5662	1.4502	9.4603	1.45	23.6011	1.3245	-0.8455	0.70	-0.41	1.3998

Real Time tracking of electromechanical oscillations in ENTSO-e Continental European Synchronous Area

March 2014

TAB. 5.13 – ESTIMATION ALGORITHMS OUTCOMES – SARDINIA LOCAL OSCILLATIONS, MODE 2

TKM		HSVD-VARPRO		ECKF		R-EMD		LPM	
$\xi$	f [Hz]	$\xi$	f [Hz]	$\xi$	f [Hz]	$\xi$	f [Hz]	$\xi$	f [Hz]
4.0911	1.1404	32.3101	1.1032	7.8045	1.3227	0.0552	1.1223	0.4712	1.3402
0.6876	1.3893	32.5705	1.3776	16.3031	1.2883	0.1462	1.1858	0.1883	1.3021
-0.2445	1.3945	2.5677	1.4001	8.5955	1.3301	-0.5643	1.1453	-0.0395	1.3302
0.6872	1.4090	7.5638	1.4001	12.9073	1.2993	1.1722	0.9723	0.0174	1.3305
0.5598	1.3455	3.0554	1.3425	10.9032	1.3705	0.4873	1.1747	-0.4259	1.3502
0.5567	1.3751	6.6828	1.3723	26.8018	1.2386	-0.4236	1.1822	0.2115	1.3111
-0.1987	1.3760	-5.2952	1.3832	19.4041	1.3005	-3.1642	0.9241	-2.4051	1.3220
0.4040	1.3654	8.2354	1.3765	35.2088	1.3013	-0.4218	1.1411	-0.8143	1.3102
21.4703	0.2679	3.4785	0.8555	12.8047	1.2084	-1.8992	1.1263	3.0023	1.3066
-3.5064	1.4709	5.4777	1.4702	14.4012	1.2944	-0.3065	1.1653	-0.2142	1.3094
-0.0998	1.3985	12.108	1.3923	-2.4862	1.3903	-0.6122	1.1652	0.9512	1.3403
-0.2440	1.3643	1.8937	1.3834	-2.5263	1.3702	-0.6295	1.1843	-0.5312	1.3411
45.9411	0.2410	2.7444	0.7684	-1.7554	1.3273	-0.3423	1.1532	-1.0023	1.3110
20.5006	1.0258	2.5232	1.0500	18.8011	1.3255	5.7722	1.2488	2.0036	1.3404
4.8969	1.0110	4.6263	1.005	25.3001	1.2532	2.6206	1.2994	-0.0523	1.3303

March 2014

TAB. 5.14 – ESTIMATION ALGORITHMS OUTCOMES – SARDINIA LOCAL OSCILLATIONS, MODE 3

TKM		HSVD-VARPRO		ECKF		R-EMD		LPM	
$\xi$	f [Hz]	$\xi$	f [Hz]	$\xi$	f [Hz]	$\xi$	f [Hz]	$\xi$	f [Hz]
24.2374	0.2998	49.2822	0.3367	20.4012	0.6128	-5.2422	0.4388	0.4712	0.7002
6.0363	0.8403	6.2315	0.8224	30.8523	0.5755	0.9351	0.4286	0.1812	0.6166
38.9834	0.5788	6.1253	0.5066	18.7044	0.6352	2.3121	0.7103	-0.0321	0.6502
12.1343	0.8804	5.5053	0.9081	36.5221	0.6024	0.5662	0.4195	0.0124	0.6404
8.1927	0.7732	2.1978	0.80	25.9044	0.6135	0.6033	0.5758	-0.4282	0.6111
5.9656	0.7423	0.0783	0.7027	34.6121	0.5762	-0.5261	0.5657	0.2113	0.6503
5.3523	0.8084	-2.7446	0.8052	29.0042	0.6228	-1.9873	0.5569	-2.4012	0.6800
6.9772	0.8543	1.6625	0.8541	32.7241	0.5687	0.7614	0.5495	-0.8141	0.6801
0.8953	0.8402	0.8973	0.8043	33.5041	0.6544	2.2333	0.4888	3.0011	0.6600
-1.9534	0.8763	2.2573	0.8567	29.2394	0.6223	-0.2014	0.5168	-0.2123	0.5994
46.7638	0.8464	0.8968	0.8288	38.0034	0.6586	2.0714	0.4859	0.9551	0.6167
12.2561	0.7554	-1.4385	0.7642	33.8021	0.5917	-1.3456	0.5075	-0.5312	0.6402
-0.2964	0.7222	-0.1834	0.7464	32.8464	0.6455	-4.8625	0.5058	-1.0024	0.7001
1.6741	0.7232	1.9278	0.7444	42.4323	0.4923	6.7172	0.5488	2.0142	0.6099
24.4403	0.6826	4.8966	0.7025	37.8170	0.4934	2.6852	0.5489	-0.0521	0.6217

Real Time tracking of electromechanical oscillations in ENTSO-e Continental European Synchronous Area

March 2014

TAB. 5.15 – ESTIMATION ALGORITHMS OUTCOMES – SARDINIA LOCAL OSCILLATIONS, MODE 4

TKM		HSVD-VARPRO		ECKF		R-EMD		LPM	
$\xi$	f [Hz]	$\xi$	f [Hz]	$\xi$	f [Hz]	$\xi$	f [Hz]	$\xi$	f [Hz]
5.0013	0.0503	-0.4202	0.0899	-3.4503	0.1287	27.6701	0.0695	-1.3241	0.1401
33.6901	0.1704	-0.3603	0.1723	43.5082	0.0963	11.4203	0.1802	4.4702	0.0899
7.2523	0.5123	-0.2722	0.4822	46.3002	0.1145	-0.3389	0.4423	1.0703	0.0992
20.9501	0.2432	1.3903	0.2661	48.5032	0.1294	-1.5521	0.1749	0.0889	0.1089
32.8020	0.2321	0.7583	0.2314	31.9015	0.0959	0.7824	0.3244	-2.8904	0.0997
16.1702	0.2212	-0.3232	0.2224	28.9064	0.1394	1.9463	0.2924	10.0842	0.1211
11.9900	0.1443	-0.0331	0.2442	4.9335	0.1235	-8.1484	0.1099	-4.5803	0.1210
13.7503	0.1543	-0.6462	0.1827	-1.5125	0.1364	0.9953	0.1522	1.7242	0.1431
3.4801	0.2541	-0.3323	0.2657	46.1067	0.1274	-1.9553	0.2203	-1.8112	0.0996
9.3325	0.3456	-0.7964	0.3048	46.5031	0.0993	0.0992	0.2230	-1.9911	0.0899
11.3053	0.3634	-0.2632	0.3286	41.8046	0.1295	3.6142	0.1932	-0.0992	0.0897
27.2934	0.2304	0.0625	0.2554	40.9036	0.0994	-4.2512	0.1831	-8.2510	0.1088
3.1184	0.2645	1.2353	0.2834	41.9074	0.1047	-3.9142	0.2401	-5.6803	0.1203
9.7801	0.2855	1.2322	0.2646	18.0023	0.1364	1.1624	0.0509	4.6901	0.1306
0.0084	0.0853	1.3439	0.1069	23.6011	0.1284	2.7645	0.0909	13.0234	0.1241

## Chapter 6

### ***Concluding remarks and future works***

The present thesis addressed the issue of estimating in real time electromechanical oscillations in power systems through the use of enabling technologies such as WAMS and advanced estimation methodologies. The onset of electromechanical oscillations in modern power systems is quite common, especially at European level, because of the reasons well-described in the prolegomeni. Hence, by following the UCTE recommendations, the performed work try to furnish a valid help to the TSO in improving the measure of proximity to critical conditions, enhancing at the same time the possibility of very fast reactions. This support consisted in the definition of one estimation algorithm demonstrated to be *(i)* high accurate to augment the TSO's situational awareness against critical and not critical electromechanical oscillations phenomena, *(ii)* characterized by reduced computational burden and flexible enough to be implemented in TSO's simulation platforms WAMS interfaced, *(iii)* high robust against all the potential situations encountered in the ordinary operation. Such an algorithm, whose name coined in this thesis takes the last name of its developers, briefly LPM, is the product of an in-depth literature analysis and field tests. More specifically, in the early stages of the research activities we focused on the most popular algorithms employed in the accredited scientific literature by coding and implementing them in the Italian TSO environment simulation WAMS interfaced. The field response allowed to identify the strengths to preserve and drawbacks to overcome. In this sense to capture the non-linearity and non-stationarity trait of the electromechanical oscillations and for exploiting some remarkable properties not satisfied from other mathematical operators our attention is moved towards Hilbert transform based methodologies. The first improvement to the most recent Hilbert Huang refinements was to replace the EMD, characterized by several heuristic assumptions, with an analytical signal decomposition theorem based upon the Bedrosian identity. Each provided elemental component has the important

March 2014

feature to be mono-frequency so solving the mode mixing issue in the EMD and hence avoiding wrongful understanding of the power systems dynamic evolution. The second one is to adopt a preliminary non-linear spectral analyzer, the  $L_p$  periodogram, instead than the standard FFT in order to identify the mode frequency values. As confirmed from the experimental findings, the  $L_p$  periodogram, is found to be very resilient against noise, data packet dropouts and to the proximity of the frequency components. FFT instead, estimating the stationary equivalents of potential non-stationary frequency components could lose details about the lower energy components, making ineffective the improvements proposed by Laila et al. with the R-EMD. Furthermore all the algorithms considered in this work were tested against some critical wide area communication network effects, exactly noise and data packet dropouts. The response of the developed algorithm, thanks to the characteristics of the  $L_p$  periodogram and to the damping calculation method proposed, is also successful in these situations. Thanks to the Terna support the application domain for the analyzed estimation methodologies was the ENTSO-e CESA: some recent actual inter-area and local oscillations recorded in this large interconnected system have undergone to evaluation. A general triggering criterion was also defined in order to implement potential automatic system actions avoiding false alarms such as generators' re-dispatch, tie line flows adjustment, load reduction, network topology change.

The encouraging experimental results achieved led the Italian TSO to investigate a properly integration of this algorithm with an automatic closed-loop control in the next future.

Furthermore, since some of the considered algorithms provide often outcomes consistent with the ones of the LPM our idea is to equip the EMS with the more accurate and robust algorithms (e.g. TKM) defining smart criteria for merging the obtained information. A promising paradigm selected in this sense is the *multi mode data fusion* which is a process of combining or amalgamating information from multiple data sources and mathematical models. Real time tracking of electromechanical oscillations may benefit from the ability of the data fusion paradigm to combine information derived from multiple estimation algorithms implemented in the EMS.

At last, an interesting further research line will be directed towards the investigation about the effect of the pervasive introduction of DG (especially wind and solar plants) in the ENTSO-e CESA on the frequency and damping ratio of its inter-area modes. The reasons of potential changes are essentially due to the fact that such a type of generators do not contribute (except in very few cases of over-frequency transient) to the frequency regulation having however a reductive action on the ENTSO-e CESA global inertia which is directly linked to the parameters to estimate (exactly frequency and damping ratio).

## APPENDIX A – BEDROSIAN THEOREM PROOF

E. Bedrosian was the first to take care the validity of the following relationship under the Hilbert Transform:

$$H[f(x)g(x)] = f(x)H[g(x)] \quad A.1$$

where  $f(x)$  and  $g(x)$  are generally complex-valued functions of the variable  $x$  in  $L^2$ , and  $H[\cdot]$  the Hilbert Transform operator of the function in the square brackets defined as:

$$H[g(x)] = \frac{1}{\pi} \text{P.V.} \int_{\mathbb{R}} \frac{g(y)}{x-y} dy \quad A.2$$

with P.V. the Cauchy principal value of the integral.

Although there exist several manners to proof the theorem, the authors prefer to retrace the rationale made by its developer to get it. Let us initiate with writing Fourier transform of the product  $f(x)g(x)$  as follows:

$$H[f(x)g(x)] = \frac{1}{(2\pi)^2} \int_{-\infty}^{+\infty} ds \int_{-\infty}^{+\infty} F(s)G(t)e^{i(s+t)x} dt \quad A.3$$

Eq. (A.3) can be rewritten by using the basic result that  $H[e^{ikx}] = i \text{sgn}(k)e^{ikx}$  :

$$H[f(x)g(x)] = \frac{1}{(2\pi)^2} \int_{-\infty}^{+\infty} ds \int_{-\infty}^{+\infty} F(s)G(t)i \text{sgn}(s+t)e^{i(s+t)x} dt \quad A.4$$

Now, since globally  $\text{sgn}(s+t)$  is equal to the  $\text{sgn}(t)$  over the integration regions where the integrand  $F(s)G(t)$  is non-vanishing the previous Eq. becomes:

March 2014

$$H[f(x)g(x)] = \frac{1}{(2\pi)^2} \int_{-\infty}^{+\infty} ds \int_{-\infty}^{+\infty} F(s)G(t) i \operatorname{sgn}(s+t) e^{i(s+t)x} dt = f(x) \frac{1}{2\pi} \int_{-\infty}^{+\infty} G(t) i \operatorname{sgn}(t) e^{itx} dt \quad A.5$$

As can be noted the term which multiplies  $f(x)$  in the Eq. A.5 is exactly the Hilbert Transform of the  $g(x)$  function:

$$H[g(x)] = \frac{1}{2\pi} \int_{-\infty}^{+\infty} G(t) H[e^{itx}] dt = \frac{1}{2\pi} \int_{-\infty}^{+\infty} G(t) i \operatorname{sgn}(t) e^{itx} dt \quad A.6$$

Hence QED:

$$H[f(x)g(x)] = f(x)H[g(x)]$$

That is the Hilbert transform of the product of a low-pass signal  $f(x)$  and a high-pass signal  $g(x)$  with non-overlapping spectra is given by the product of the low-pass signal and the Hilbert transform of the high-pass signal.

## APPENDIX B – THEOREM PROOF ON CAUCHY PRINCIPAL VALUE INTEGRAL OF OSCILLATORY FUNCTIONS

### Statement

If  $f$  is an analytic function in the half-strip of the complex plane,  $t_a \leq \Re(z) \leq t_b$  and  $\Im(z) \geq 0$  and if there exist two constants  $M$  and  $\omega_0$  such that for  $0 \leq \omega \leq \omega_0$

$$\int_{t_a}^{t_b} f(x + i\eta) dx \leq M\eta e^{\omega_0 \eta} \quad \text{B.1}$$

The following relationship holds true:

$$I_\omega(f; t) = \text{P.V.} \int_{t_a}^{t_b} e^{i\omega\tau} \frac{e^{\sigma\tau}}{t - \tau} d\tau = -ie^{i\omega t} \pi e^{\sigma t} - \frac{ie^{-i\omega t_a}}{\omega} \int_0^{+\infty} e^{-x} \frac{e^{\sigma\left(t_a + \frac{ix}{\omega}\right)}}{t_a - t + \frac{ix}{\omega}} dx + \frac{ie^{-i\omega t_b}}{\omega} \int_0^{+\infty} e^{-x} \frac{e^{\sigma\left(t_b + \frac{ix}{\omega}\right)}}{t_b - t + \frac{ix}{\omega}} dx \quad \text{B.2}$$

### Proof

According to the Cauchy Residue Theorem, being the integrand function of the complex variable  $z$ ,  $e^{i\omega z} \frac{f(z)}{t - z}$  analytic in the region  $\Omega$  except  $\Omega'$ , by taking all the contours in counterclockwise direction as showed in Fig. B.1, one has:

$$I_\omega(f; t) = \int_{\Gamma_1 + \Gamma_2 + \Gamma_3 + \Gamma_4 + \Gamma_5 + \Gamma_6} e^{i\omega z} \frac{f(z)}{t - z} dz = 0 \quad \text{B.3}$$

Let us evaluate the first integral in a specific way:

$$\int_{\Gamma_1} e^{i\omega z} \frac{f(z)}{t-z} dz = \frac{ie^{i\omega t_b}}{\omega} \int_0^{\omega\eta} e^{-x} \frac{e^{\sigma\left(t_b + \frac{ix}{\omega}\right)}}{t - t_b + \frac{ix}{\omega}} dx \quad \text{B.4}$$

and similarly

$$\int_{\Gamma_3} e^{i\omega z} \frac{f(z)}{t-z} dz = -\frac{ie^{i\omega t_a}}{\omega} \int_0^{\omega\eta} e^{-x} \frac{e^{\sigma\left(t_a + \frac{ix}{\omega}\right)}}{t - t_a + \frac{ix}{\omega}} dx \quad \text{B.5}$$

By keeping in mind that:

$$\int_{t_a}^{t_b} e^{\sigma(x+i\eta)} dx \leq M \quad \text{with} \quad M = \frac{1}{|\sigma|} \max\{e^{\sigma t_b}, e^{\sigma t_a}\} \quad \text{B.6}$$

on  $\Gamma_2$  we have:

$$\begin{aligned} \left| \int_{\Gamma_2} e^{i\omega z} \frac{f(z)}{t-z} dz \right| &= \left| - \int_{t_a}^{t_b} e^{i\omega(x+i\eta)} \frac{e^{\sigma(x+i\eta)}}{t-x-i\eta} dx \right| \\ &\leq \int_{t_a}^{t_b} e^{-\omega\eta} \left| \frac{e^{\sigma(x+i\eta)}}{t-x-i\eta} \right| dx \\ &\leq \frac{e^{-\omega\eta}}{\eta} \int_{t_a}^{t_b} e^{\sigma x} dx \\ &\leq \frac{e^{-\omega\eta}}{\eta} M \rightarrow 0, \quad \eta \rightarrow \infty. \end{aligned} \quad \text{B.7}$$

In correspondence of the half circle contour  $\Gamma_5$ , containing the singularity  $z=t$ , one can make the position  $z-t = re^{i\theta}$ , with  $0 \leq \theta \leq \pi$ , so that:

$$\int_{\Gamma_5} e^{i\omega z} \frac{f(z)}{t-z} dz = -\int_0^\pi e^{i\omega(t+re^{i\theta})} \frac{e^{\sigma(t+re^{i\theta})}}{re^{i\theta}} re^{i\theta} i d\theta = -ie^{i\omega t} \int_0^\pi e^{ire^{i\theta}} e^{\sigma(t+re^{i\theta})} d\theta \rightarrow -i\pi e^{i\omega t} e^{\sigma t} \Big|_{r \rightarrow 0} \quad \text{B.8}$$

At this point, by recalling the C.P.V. integral definition and exploiting the Eq. B.3, it is immediate to derive relationship B.2.

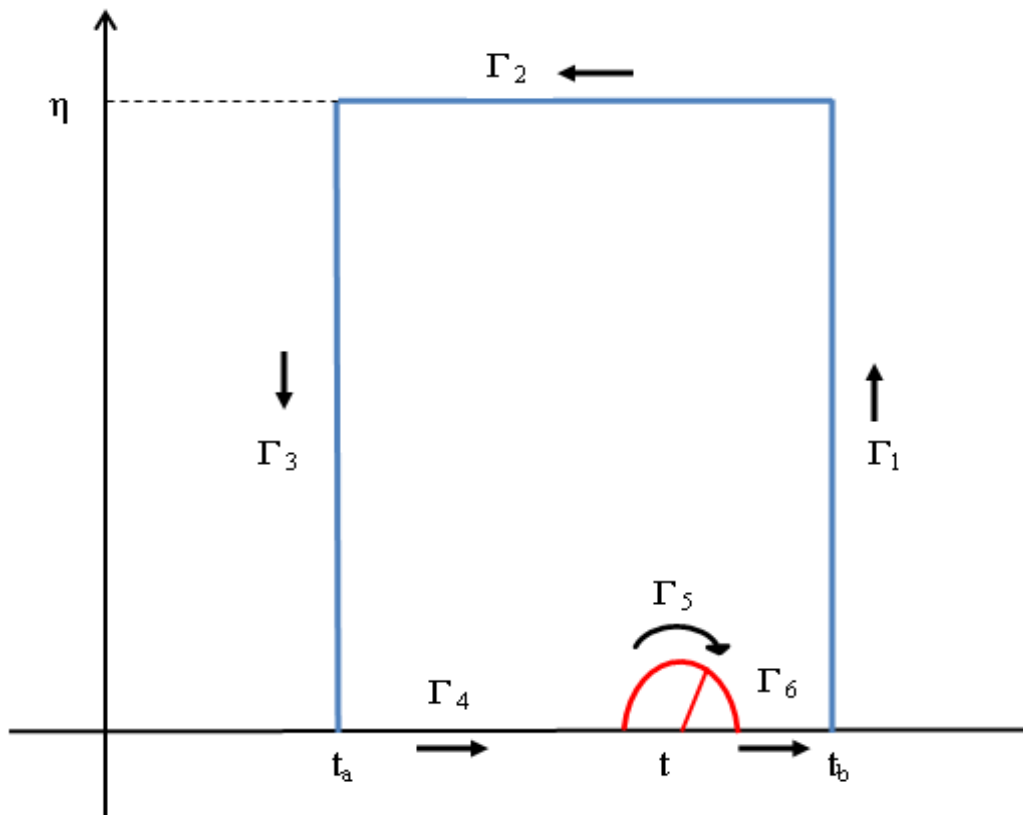


Fig. B.1 – Path of integration for  $I_\omega(f;t)$

## References

- [1] G. Phadke, J. S. Thorp, and M. G. Adamiak, "New Measurement Techniques for Tracking Voltage Phasors, Local System Frequency, and Rate of Change of Frequency," *IEEE Transactions on Power Apparatus and Systems*, vol. 102, no. 5, pp. 1025-1038, May 1983.
- [2] D. Cirio, A. Danelli, M. Pozzi, S. Cecere, et al., "Wide Area Monitoring and Control System: the Italian research and development," *CIGRE Session*, C2-208, Paris, 2006.
- [3] Candia, D. Cirio, G. Giannuzzi, M. Pozzi, et al., "PMU location and parameter identification techniques for the Italian Wide-Area Measurement System," *International World Energy System Conference (WESC)*, 10th-12nd July, Turin, Italy, 2006.
- [4] E. Ciapessoni, D. Cirio, G. Giannuzzi, C. Sabelli, "Wide area monitoring in the Italian system and advanced perspectives for PMU synchronisation," *Monitoring of Power System Dynamics Performance Conference*, 28-30 April, Saint Petersburg, Russia, 2008.
- [5] G. Giannuzzi, C. Sabelli, R. Salvati, et al., "Voltage and angle stability monitoring: possible approaches in the framework of a Wide Area Measurement System (WAMS)," *CIGRE Session*, C2-114, Paris, 2008.
- [6] Cirio, D. Lucarella, S. Massucco, "On-line Dynamic Security Assessment to mitigate the risk of blackout in the Italian power system," *European Transactions on Electrical Power*, vol. 18, no. 8, pp.784-801, Nov 2008.
- [7] Bruno, C. Candia, L. Franchi, et al., "Possibility of enhancing classical weighted least squares state estimation with linear PMU measurements," *IEEE Power Tech Conference*, June 28th - 2nd July, Bucharest, Romania, 2009, pp. 1-6.
- [8] B. Mohammadi-Ivatloo, M. Shiroei, M. Parniani, "Online small signal stability analysis of multi-machine systems based on synchronized phasor measurements," *Elsevier Electric Power Systems Research*, vol. 81, no. 10, pp. 1887-1896, Oct. 2011.
- [9] L.P. Di Noia, D. Lauria, C. Pisani, D. Villacci, "A novel procedure for real-time detection of inter-area oscillations", *IEEE Energycon Conference*, September 9th-12nd, Florence, Italy, 2012, pp. 433-438.
- [10] S.M. Kay, *Fundamentals of Statistical Signal Processing: Estimation Theory*, vol.1, Prentice Hall PTR, New Jersey, 1993.

March 2014

- [11] U. S. Department of Energy, "Algorithm Summary and Evaluation: Automatic Implementation of Ring-down Analysis for Electromechanical Mode Identification from Phasor Measurements", 2010.
- [12] B. Pal, B. Chaudhuri, *Robust Control in Power Systems*, Springer, New York, 2005.
- [13] Lauria, C. Pisani, D. Villacci, "Probabilistic transient stability margins assessment based upon quadratic stability region approximation," *IEEE Energycon Conference*, September 9th-12nd, Florence, Italy, 2012, pp. 439-444.
- [14] Chiodo, D. Lauria, C. Pisani and D. Villacci, "Transient Stability Margins Evaluation Based Upon Probabilistic Approach," *International Review of Electrical Engineering*, vol. 8, no.2, pp. 752-761, Dec. 2013.
- [15] D. Lauria, C. Pisani, "Transient Stability Assessment Based Upon Differential Transform Method," *International Review of Electrical Engineering*, vol. 7, no. 1, pp. 4925-4935, August 2012.
- [16] ENTSO-e Interim Report of the Investigation Committee on the 28 September 2003 Blackout in Italy, <https://www.entsoe.eu/news-events/former-associations/ucte/other-reports>.
- [17] ENTSO-e Interim Report - System Disturbance on 4 November 2006, <https://www.entsoe.eu/news-events/former-associations/ucte/other-reports/>
- [18] J.P. Hespanha, P. Naghshtabrizi, Xu Yonggang, "A Survey of Recent Results in Networked Control Systems," *Proceedings of the IEEE*, vol. 95, pp. 1, Jan 2007.
- [19] M. M. Begovic, D. Novosel, D. Karlsson, C. F. Henville et al., "Wide area protection and emergency control," *IEEE Transaction on Power Delivery*, vol. 93, no. 5, pp. 876-891. May 2005.
- [20] D. Cay, *Wide Area Monitoring, Protection and Control in the future of the Great Britain power system*, PhD Disseration, 2012.
- [21] C.W. Taylor, "Wide Area Measurement, Monitoring and Control in Power Systems," *Workshop on Wide Area Measurement, Monitoring and Control in Power Systems*, Imperial College, London, Mar. 16-17, 2006.
- [22] D. Yan, *Wide-area Protection and Control System with WAMS Based*, *International Conference on Power System Technology (PowerCon2006)*, China, Oct. 22nd-26th, Chongqing, China, 2006, pp. 1-5.
- [23] M.S. Thomas, D. Nanda and I. Ali, *Development of a Data Warehouse for Nonoperational Data in Power Utilities*, *Proceeding Power India Conference*, New Dehli, India, 2006.
- [24] G.D. Jelatis, *Information Security Primer*, Electric Power Research Institute Report, 2001.
- [25] Clarke and D. Reynders, *Practical Modern SCADA Protocols: DNP3, 60870.5 and Related Systems*. Elsevier, Oxford, England, 2004.

March 2014

- [26] Trends in SCADA for Automated Water Systems, *Synchrony*, 2001.
- [27] A.G. Phadke and J.S. Thorp, Synchronized Phasor Measurements and Their Applications, *Springer*, 2008.
- [28] M. Kezunovic, Integration of Substation IED Information into EMS Functionality, Final Project Report, Power Systems Engineering Research Center (PSERC), 2008.
- [29] Considerations for use of disturbance recorders, A report to the System Protection Subcommittee of the Power System Relaying Committee of the IEEE Power Engineering Society, IEEE Inc., 2006.
- [30] M. Shahraeini et al. , A New Approach for Classification of Data Transmission Media in Power Systems, *International Conference on Power System Technology*, October 24-28, Hangzhou, China, 2010, pp. 1-7.
- [31] N. Zhou, Z. Huang, F. Tuffner, S. Jin et al, Algorithm Summary and Evaluation: Automatic Implementation of Ringdown Analysis for Electromechanical Mode Identification from Phasor Measurements, Pacific National Northwest Laboratory (PNNL) Report, 2010.
- [32] J. Pierre, D.J. Trudnowski, and M.K. Donnelly, "Initial results in electromechanical mode identification from ambient data," *IEEE Transactions on Power Systems*, vol. 12, no. 3, pp. 1245-1251, Aug. 1997.
- [33] J.F. Hauer, C. J. Demeure, and L.L. Scharf, "Initial Results in Prony Analysis of Power System Response Signals," *IEEE Transactions on Power Systems*, vol. 5, no. 1, pp. 80-89, Feb. 1990.
- [34] N. Zhou, J. Pierre, and J. Hauer, "Initial Results in Power System Identification from Injected Probing Signals Using a Subspace Method," *IEEE Transaction on Power Systems*, vol. 21, no. 3, pp. 1296-1302, Aug 2006.
- [35] L. Vanfretti, S. Bengtsoon, J.O Gjerde, "Preprocessing synchronized phasor measurement data for spectral analysis of electromechanical oscillations in the Nordic Grid," *International Transactions on Electrical Energy Systems*, early view at <http://onlinelibrary.wiley.com/doi/10.1002/etep.1847/abstract>.
- [36] D. Trudnowski, J. Pierre, N. Zhou, J. Hauer, et al. "Performance of three mode-meter block-processing algorithms for automated dynamic stability assessment," *IEEE Transactions on Power Systems*, vol. 23, no. 2, pp. 680-690, May 2008.
- [37] L. Ljung, System Identification Theory for the User, Prentice Hall, Upper Saddle River, New Jersey, 1999.
- [38] N. Zhou, J.W. Pierre, D. Trudnowski, R. Guttromson, "Robust RLS Methods for On-line Estimation of Power System Electromechanical Modes," *IEEE Transactions on Power Systems*; vol. 22, no. 3, pp. 1240-1249, May 2007.
- [39] P. Van Overschee, B. De Moor, Subspace Identification for Linear Systems: Theory-Implementation-Applications, Kluwer Academic Publishers, London, 1996.

March 2014

- [40] B. Kovacevic, M. Milosavljevic, M. Veinovic, "Robust Recursive AR Speech Analysis," *Signal Processing*, vol. 44, no. 2, pp. 125-138, June 1995.
- [41] P.W. Sauer, M.A. Pai, *Power system dynamics and stability*, Prentice Hall, Upper Saddle River, New Jersey, 1988.
- [42] M.A. Pai, *Energy Function Analysis for Power System Stability*, Kluwer Academic Publishers, Boston, 1989.
- [43] P. Kundur, *Power system stability and control*, McGraw-Hill Education, California, 1994.
- [44] L. Grigsby, *Power system stability and control*, CRC Press, New York, 2012.
- [45] Rogers, *Power system oscillations*, Kluwer Academic Publishers, Boston, 2000.
- [46] G.H. Hardy, G. Rogosinsky, *Fourier Series*, Dover Publications, New York, 1956.
- [47] T.J. Browne, V. Vittal, G.T. Heydt, and A. R. Messina, "Practical Application of Hilbert Transform Techniques in Identifying Inter-area Oscillations," in *Inter-area oscillations in Power Systems: A Nonlinear and Nonstationary Perspective.*, Springer, New York, 2009.
- [48] K. Duda, L. B. Magalas, M. Majewski, T. P. Zielinski, "DFT-based Estimation of Damped Oscillation Parameters in Low-Frequency Mechanical Spectroscopy," *IEEE Transaction Instrumentation and Measurement*, vol. 60, no. 11, pp. 3608-3618, Nov. 2011.
- [49] P. O'Shea, "The use of sliding spectral windows for parameters estimation in power system disturbance monitoring," *IEEE Transaction on Power Systems*, vol. 15, no. 4, pp. 1261-1267, Nov. 2000.
- [50] K. P. Poon, K. C. Lee, "Analysis of transient stability swings in large interconnected power systems by Fourier transformation," *IEEE Transaction on Power Systems*, vol. 3, no. 4, pp. 1573-1581, Nov. 2007.
- [51] G. Ledwich, E. Palmer and A. Gosh, "Detection and Estimation of Nonstationary Power Transients," in *Inter-area oscillations in Power Systems: A Nonlinear and Nonstationary Perspective.*, Springer, New York, 2009.
- [52] L. Scharf, *Statistical Signal Processing: Detection, Estimation, and Time Series Analysis*, Addison Wesley Publishing Company, Inc., 1991.
- [53] J. Xiao, X. Xie, Y. Han and J. Wu, "Dynamic tracking of low-frequency oscillations with improved Prony method in wide-area measurement system", *Conference Publications of IEEE Power Engineering Society General Meeting*, 10th June, vol. 1, 2004, pp. 1104 - 1109.
- [54] X. Xie, Y. Xin, J. Xiao, J. Wu, et al, "WAMS applications in Chinese power system," *IEEE Power and Energy Magazine*, vol. 4, no. 1, pp.54-63, Jan-Feb 2006.

March 2014

- [55] D.W. Tufts, R. Kumaresan, "Estimation of Frequencies of Multiple Sinusoids: Making Linear Prediction Perform Like Maximum Likelihood," *Proceedings of the IEEE*, vol. 70, no.97, Sept 1982.
- [56] R. Kumaresan, D.W. Tufts, "Estimating the Parameters of Exponentially Damped Sinusoids and Pole-Zero Modeling in Noise", *IEEE Transactions on Acoustics, Speech, and Signal Processing*, vol. ASSP-30, no.6, Dec 1982.
- [57] R. Kumaresan, "On the zeros of the linear prediction error filter for deterministic signals", *IEEE Transactions Acoustics, Speech, and Signal Processing*, vol. ASSP-31, no.1, Feb 1983.
- [58] J. Zhang, A.K. Swain and S.K. Nguang, "Parameter Estimation of Exponentially Damped Sinusoids using HSVD based Extended Complex Kalman Filter," *IEEE TENCON Region 10 Conference*, Nov 19-21, Hyderabad, India, 2008.
- [59] S.Y. Kung, K.S. Arun and D.V. Bhaskar Rao, "State-space and singular-value decomposition-based approximation methods for the harmonic retrieval problem," *Journal of the Optical Society of America*, vol. 73, no.12, pp. 1799-1811, Dec 1983.
- [60] B.W. Rust, "Fitting nature's basic functions. Part IV: The variable projection algorithm," *IEEE Journal Computing in Science and Engineering*," vol. 5, no. 2 ,pp. 74-79, Mar./Apr. 2003.
- [61] J.C.H. Peng and N.K.C. Nair, "Enhancing Kalman Filter for Tracking Ringdown Electromechanical Oscillations," vol. 27, no. 2, pp. 1042-1050, May 2002.
- [62] S. Haykin, *Adaptive Filter Theory*, Prentice-Hall, Englewood Cliffs, New Jersey, 2002.
- [63] J.C.H. Peng et al., "Detection of lightly damped inter-area power oscillations using extended complex Kalman filter," in *Proceedings IEEE Region 10 Conference*, 23th-26th Jan, Singapore, pp. 1-5, 2009.
- [64] S. Shukla, S. Mishra, B. Singh, "Empirical-Mode Decomposition With Hilbert Transform for Power-Quality Assessment," *IEEE Transactions on Power Delivery*, vol. 24, no. 4, pp. 2159-2165, Sept 2009.
- [65] L. Zhenghua, "Hilbert-Huang Transform Based Application in Power System Fault Detection," *Proc. International Workshop on Intelligent Systems and Applications*, Wuhan, China, May 2009, pp. 1-4,
- [66] N. Senroy, "Enhancements to the Hilbert-Huang Transform for Application to Power System Oscillations," in *Inter-area oscillations in Power Systems: A Nonlinear and Nonstationary Perspective.*, Springer, New York, 2009.
- [67] N.E. Huang, Z. Shen, S. R. Long, M. C. Wu et al., "The empirical mode decomposition and Hilbert Spectrum for nonlinear and non-stationary time series analysis", *Proceedings of the Royal Society of London*, vol. 454 A, no. 1971, pp. 903-995, March 1998.

March 2014

- [68] M. Feldman, "Theoretical analysis and comparison of the Hilbert transform decomposition methods," *Mechanical System and Signal Processing*, vol. 22, no. 3, pp. 509-519, April 2008.
- [69] R.T. Rato, M.D. Ortigueira, A.C. Batista, "On the HHT, its problems and some solutions," *Mechanical Systems and Signal Processing*, vol. 22, no. 6, pp. 1374-1394, Aug 2008.
- [70] D. Vakman, "On the Analytic Signal, the Teager-Kaiser Energy Algorithm, and Other Methods for Defining Amplitude and Frequency," *IEEE Transactions on Signal processing*, vol. 44, no. 4, pp. 791 - 797, April 1996.
- [71] H. Li, L. Li, T. Qian, "Discrete-time analytic signals and Bedrosian product theorems," *Digital Signal Processing*, vol. 20, no. 4, pp. 982-990, July 2010.
- [72] G. D. Cain, "Hilbert transform relations for products," *Proceedings of IEEE*, pp. 673-674, May 1973.
- [73] F.K. Wing, *Hilbert Transforms*, Cambridge University Press, Cambridge (UK), May 2010.
- [74] R. Deering, J.F. Kaiser, "The use of masking signal to improve empirical mode decomposition," *Proceedings of IEEE Int. Conf. Acoustics, Speech Signal Processing (ICASSP)*, Philadelphia, USA, March 2005, pp. 485-488.
- [75] O.E. DeLange, "Optical heterodyne detection," *IEEE Spectrum*, vol. 5, no. 2, pp. 77-85, Oct 1968.
- [76] D.S. Laila, A.R. Messina, B.C. Pal, "A refined Hilbert-Huang transform with applications to interarea oscillations monitoring," *IEEE Transactions on Power Systems*, vol. 24, no. 2, pp. 610-620, May 2009.
- [77] A. Prince, N. Senroy, R Balasubramanian, "Targeted approach to apply masking signal-based empirical mode decomposition for mode identification from dynamic power system wide area measurement signal data," *IET Generation Transmission and Distribution*, vol. 5, no. 10, pp. 1025-1032, Oct 2011.
- [78] D. Lauria, C. Pisani, "On Hilbert transform methods for low frequency oscillations detection," accepted for publication on *IET Generation Transmission and Distribution*, doi: 10.1049/iet-gtd.2013.0545.
- [79] G. Chen, Z. Wang, "A signal decomposition theorem with Hilbert transform and its application to narrowband time series with closely spaced frequency components," *Mechanical Systems and Signal Processing*, vol. 28, no. 1, pp. 258-279, April 2012.
- [80] T.H. Li, "A nonlinear method for robust spectral analysis," *IEEE Transaction on Signal Processing*, vol. 58, no. 5, pp. 2466-2474, May 2010.
- [81] J.N. Yang, Y. Lei, S. Pan, N. Huang, "System identification of linear structures based on Hilbert-Huang spectral analysis, Part I: normal modes," *Earthquake Engineering and Structural Dynamics*, vol. 32, no. 1, pp. 1443-1467, July 2003.

March 2014

- [82] L. Cohen, *Time-Frequency Analysis*, Prentice-Hall, Englewood Cliffs, New Jersey, 1995.
- [83] A.J. Jerri, "The Shannon sampling theorem – Its various extensions and applications: A tutorial review," *Proceedings of the IEEE*, vol. 65, no. 11, pp. 1565-1596, Nov 1977.
- [84] H. Boche, M. Protzmann, "A new algorithm for the reconstruction of bandlimited functions and their Hilbert transform," *IEEE Transactions on Instrumentation and Measurement*, vol. 46, no. 2, pp. 442-444, 1997.
- [85] Maly, W.P. Ziemer, *Fine Regularity of Solutions of Elliptic Partial Differential Equations*, American Mathematical Society, New York, 1997.
- [86] H. Wang, and S. Xiang, "On the evaluation of Cauchy principal value integrals of oscillatory functions," *Journal of Computational and Applied Mathematics*, vol. 234, no.1, pp.95-100, May 2010.
- [87] G.H. Golub, J.H. Welsch, "Calculation of Gauss quadrature rules," *Mathematics of Computation*, vol. 23, pp. 221-230, 1969.
- [88] D. Lauria, C. Pisani, "An improved non linear least squares method for estimating the damping levels of electromechanical oscillations," submitted to *IET Generation Transmission and Distribution*.
- [89] S. Wang, W. Gao, J. Wang, J.Lin, "Synchronized Sampling Technology-Based Compensation for Network Effects in WAMS Communication," *IEEE Transactions on Smart Grid*, vol. 3, no. 2, June 2012.
- [90] B. Naduvathuparambil, M.C. Valenti, A. Feliachi, "Communication delays in wide area measurement systems," *Proceedings of the Thirty-Fourth South-eastern Symposium on System Theory*, pp. 118-122, Mar. 2002.
- [91] A. Paopulis, S. Unnikrishna Pillai, *Probability, Random Variables and Stochastic Processes*, 4th edition, McGraw-Hill, New York, 2002.
- [92] E. Chiodo, *Lecture notes of Reliability and Diagnostics of electrical Power Systems*, 2014.
- [93] L.P. Di Noia, D. Lauria, C. Pisani, "Incidence of Some WAMS Communication Network Effects on Real-Time Tracking of Low Frequency Oscillations," *International Journal on Engineering Applications*, vol. 1, no.1, pp. 27-37, Jan 2013.
- [94] M. Klein, G.J. Rogers, and P. Kundur, "A Fundamental Study of Inter-Area Oscillations," *IEEE Transaction on Power Systems*, vol. 6, no.3, pp. 914-921, August 1991.
- [95] [http://www.mathworks.it/products/simpower/modelexamples.html?file=/products/demos/shipping/powersys/power\\_PSS.html](http://www.mathworks.it/products/simpower/modelexamples.html?file=/products/demos/shipping/powersys/power_PSS.html)
- [96] J.H. Chow, K.W. Cheung, "A toolbox for power system dynamics and control engineering education and research," *IEEE Transactions on Power Systems*, vol. 7, no. 4, pp. 1559–1564, Nov 1992.
- [97] P.M. Anderson, A.A. Fouad, *Power System Control and Stability*, IEEE Press Power Engineering Series, 2005.

March 2014

- [98] General Electric final report: 'Singular Perturbation, Coherency and Aggregation of Dynamic Systems', 1981.
- [99] M. Larsson, P. Korba, W. Sattinger, P. Owen, "Monitoring and Control of Power System Oscillations using FACTS/HVDC and Wide-area Phasor Measurements," Proceedings of CIGRE Conf.- SC B5 PS1, Paris, France, August 2012.
- [100] ENTSO-e Interim Report of the Investigation Committee on Analysis of CE inter-area oscillations of 19 and 24 February 2011, <https://www.entsoe.eu/publications/system-operations-reports/continental-europe/>.